Title

Development of acoustic radiation force optical coherence elastography system for in vivo mapping of biological tissues

Author

Qu, Yueqiao

Publication Date

2018

UNIVERSITY OF CALIFORNIA,
IRVINE

Development of acoustic radiation force optical coherence elastography system for in vivo mapping of biological tissues

DISSERTATION

submitted in partial satisfaction of the requirements
for the degree of

DOCTOR OF PHILOSOPHY

in Biomedical Engineering

by

Yueqiao Qu

Dissertation Committee:
Professor Zhongping Chen, Chair
Professor William Tang
Associate Professor Gultekin Gulsen

2018

DEDICATION

To

My loving grandmother,

Until we meet again.

TABLE OF CONTENTS

LIST OF FIGURES

Page

LIST OF TABLES

Page

TABLE OF ABBREVIATIONS

OCT	Optical coherence tomography
OCE	Optical coherence elastography
US	Ultrasound
TCFA	Thin cap fibroatheroma
AMD	Age-related macular degeneration
CT	Computed tomography
MRI	Magnetic resonance imaging
IVUS	Intravascular ultrasound
TDOCT	Time domain optical coherence tomography
FDOCT	Fourier domain optical coherence tomography
SSOCT	Swept source optical coherence tomography
SDOCT	Spectrometer based optical coherence tomography
FFT	Fast Fourier Transform
2-D	Two-dimensional
3-D	Three-dimensional
GRIN	Gradient refractive index
FWHM	Full width at half maximum
SNR	Signal to noise ratio
fps	frames per second
RPE	Retinal pigment epithelium
ARF	Acoustic radiation force
SLD	Superluminescent diode

CMOS	Complementary metal-oxide-semiconductor
CCD	Charge-coupled device
GM	Galvanometer mirrors
PSF	Point spread function
PPLK	Progressive post-LASIK keratectasia
RFA	Radiofrequency amplifier
FG	Function generator
ORA	Ocular response analyzer
LASIK	Laser-assisted in situ keratomileusis
MPE	Maximum permissible exposure
PBS	Phosphate-buffered saline
H&E	Hematoxylin and eosin
FAF	Fundus autofluorescence
LED	Light-emitting diode
MI	Mechanical index
UV	Ultraviolet

ACKNOWLEDGMENTS

I would like to express my most sincere appreciation to my mentor, Professor Zhongping Chen, for his endless support and nurture throughout my graduate career. He has tirelessly taught me everything I know about research and paved my path to pursue an academic career. Not only was he an integral part of my studies, he was also a life coach. With great patience and compassion, he often shared valuable life experiences and offered warmhearted advice. I am forever grateful.

I would like to thank my committee members, Professor Gultekin Gulsen and Professor William Tang, for continued support and devotion to this dissertation. I very much appreciate Dr. Gulsen's encouragement and guidance that began even before my admission to UCI, through all the lunch meetings, until now and beyond.

In addition, I want to specially thank our collaborators from UCI, USC, and Columbia University: Professor Qifa Zhou, Professor Mark Humayun, Professor Ron Silverman, and Professor Pranav Patel. This project would not have been possible without their expertise and dedication. Dr. Zhou has been a constant source of inspiration and a role model in ophthalmic research.

I am grateful for all my colleagues and have truly enjoyed working with everyone. I thank the life-long friends I have made in the FOCT lab. Dr. Joe Jing, Danny Chou, and Dr. Jiawen Li, thank you for teaching me the way around the lab. I would like to thank Dr. Jiang Zhu and Dr. Teng Ma for the productive collaborations. I am grateful to Dr. Cuixia Dai for her dedicated teaching of optical systems. I also want to thank Yan Li, Emon Heidari, Yusi Miao, and Jason Chen, my wonderful friends and labmates for their companionship in the lab and the endless gossip sessions.

I would like to thank Tanya, Sari, David, and Professor Brenner's entire lab, for their endless help during animal experiments, and for the fresh tissue samples. I want to thank Leacky Liaw for her patient lessons on histology and tissue analysis.

I would like to offer my deepest gratitude to my parents for their unconditional support and selflessly providing me with the opportunities to pursue my dreams. My father has always been my role model and has given me valuable wisdom and advice in my Ph.D. journey. My mother is my pillar of support, always encouraging me with a smile and comforting me during hard times. I also want to thank my sister, Rochelle, for her undying cheerfulness and good spirits, which always fuels me with energy to continue my studies.

Finally, I would like to thank my labmate and my best friend, who also happens to be my amazing husband, Youmin. I cannot thank you enough for everything you've done for me, from writing all of the coding for this dissertation project to your loving reassurances when times were tough. Through this dissertation project, we fell in love, got married, and had our incredible daughter, Kimi. Thank you to Kimi for sleeping while I wrote and for the many encouraging smiles. I am deeply thankful for all the blessings.

CURRICULUM VITAE

Yueqiao Qu

2011	B.S. in Biomedical Engineering, Johns Hopkins University
2016	M.S. in Biomedical Engineering, University of California, Irvine
2018	Ph.D. in Biomedical Engineering, University of California, Irvine

FIELD OF STUDY

Biophotonics and Biomedical Imaging

PUBLICATIONS

1) **Yueqiao Qu,** Youmin He, Yi Zhang, Teng Ma, Jiang Zhu, Yusi Miao, Cuixia Dai, Qifa Zhou, Mark Humayun, Qifa Zhou, Zhongping Chen. "Quantified elasticity mapping of retinal layers using acoustic radiation force optical coherence elastography." *Biomedical optics express* (Under review).

2) **Yueqiao Qu,** Youmin He, Arya Saidi, Yihang Xin, Yongxiao Zhou, Jiang Zhu, Teng Ma, Ronald H. Silverman, Donald S. Minckler, Qifa Zhou, Zhongping Chen. "In-vivo elasticity mapping of posterior ocular layers using acoustic radiation force optical coherence elastography." *Investigative ophthalmology & visual science* 59, 455-461 (2018).

3) Jiang Zhu, Junxiao Yu, **Yueqiao Qu**, Youmin He, Yan Li, Qiang Yang, Tiancheng Huo, Xingdao He, and Zhongping Chen. "Coaxial excitation longitudinal shear wave measurement for quantitative elasticity assessment using phase-resolved optical coherence elastography." *Optics Letters* 43, 2388-2391 (2018).

4) Sucbei Moon, **Yueqiao Qu**, Zhongping Chen. "Characterization of spectral-domain OCT with autocorrelation interference response for axial resolution performance." *Optics Express* 26, 7253-69 (2018).

5) **Yueqiao Qu**, Teng Ma, Youmin He, Mingyue Yu, Cuixia Dai, Jiang Zhu, K. Kirk Shung, Qifa Zhou, Zhongping Chen. "Miniature probe for mechanical properties of vascular lesions using acoustic radiation force optical coherence elastography." *Scientific Reports,* 7, 4731 (2017).

6) Yan Li, Joseph Jing, **Yueqiao Qu**, Yusi Miao, Buyun Zhang, Teng Ma, Mingyue Yu, Qifa Zhou, Zhongping Chen. “Fully integrated optical coherence tomography, ultrasound, and indocyanine green-based fluorescence tri-modality system for intravascular imaging.” *Biomedical Optics Express,* 8, 1036-44 (2017).

7) Wesley J. Moy, Erica Su, Jason J. Chen, Connie Oh, Joe C. Jing, **Yueqiao Qu**, Youmin He, Zhongping Chen, Brian JF Wong. "Association of Electrochemical Therapy With Optical, Mechanical, and Acoustic Impedance Properties of Porcine Skin." *JAMA facial plastic surgery* 19, 502-509 (2017).

8) Yan Li, Joseph Jing, Emon Heidari, Jiang Zhu, **Yueqiao Qu**, and Zhongping Chen. "Intravascular Optical Coherence Tomography for Characterization of Atherosclerosis with a 1.7 Micron Swept-Source Laser." *Scientific Reports* 7, 14525 (2017).

9) Jiang Zhu, Yusi Miao, Li Qi, **Yueqiao Qu**, Youmin He, Qiang Yang, and Zhongping Chen. “Longitudinal shear wave imaging for elasticity mapping using optical coherence elastography.” *Applied Physics Letters* 110, 201101 (2017).

10) **Yueqiao Qu**, Teng Ma, Youmin He, Jiang Zhu, Cuixia Dai, Mingyue Yu, Shenghai Huang, Fan Lu, K. Kirk Shung, Qifa Zhou, and Zhongping Chen. "Acoustic Radiation Force Optical Coherence Elastography of Corneal Tissue." *Selected Topics in Quantum Electronics, IEEE Journal of* 22, 1-7 (2016).

11) Jiang Zhu, Li Qi, Yusi Miao, Teng Ma, Cuixia Dai, **Yueqiao Qu**, Youmin He, Yiwei Gao, Qifa Zhou, and Zhongping Chen. “3D mapping of elastic modulus using shear wave optical micro-elastography.” *Scientific Reports* 6, (2016).

12) Jiang Zhu, **Yueqiao Qu**, Teng Ma, Rui Li, Yongzhao Du, Shenghai Huang, K. Kirk Shung, Qifa Zhou, and Zhongping Chen. "Imaging and characterizing shear wave and shear modulus under orthogonal acoustic radiation force excitation using OCT Doppler variance method." *Optics letters* 40, 2099-2102 (2015).

13) Jie Hui, Qianhuan Yu, Teng Ma, Pu Wang, Yingchun Cao, Rebecca S. Bruning, **Yueqiao Qu**, Zhongping Chen, Qifa Zhou, Michael Sturek, Ji-Xin Cheng, and Weibiao Chen. “High-speed intravascular photoacoustic imaging at 1.7 μm with a KTP-based OPO.” *Biomedical optics express* 6, 4557-4566 (2015).

14) Giriraj K. Sharma, Gurpreet S. Ahuja, Maximilian Wiedmann, Kathryn E. Osann, Erica Su, Andrew E. Heidari, Joseph C. Jing, **Yueqiao Qu**, Frances Lazarow, Alex Wang, Lidek Chou, Cherry C. Uy, Vijay Dhar, John P. Cleary, Nguyen Pham, Kevin Huoh, Zhongping Chen, and Brian J-F Wong. “Long-range optical coherence tomography of the neonatal upper airway for early diagnosis of intubation-related subglottic injury.” *American journal of respiratory and critical care medicine* 192, 1504-1513 (2015).

15) Verinika Volgger, Giriraj K. Sharma, Joseph C. Jing, Ya-Sin A. Peaks, Anthony Chin Loy, Frances Lazarow, Alex Wang, **Yueqiao Qu**, Erica Su, Zhongping Chen, Gurpreet S. Ahuja, Brian J-F Wong. “Long-range Fourier domain optical coherence tomography of the pediatric subglottis.” *International journal of pediatric otorhinolaryngology* 79, 119-126, (2015).

ABSTRACT OF THE DISSERTATION

Development of acoustic radiation force optical coherence elastography system for in vivo mapping of biological tissues

By

Yueqiao Qu

Doctor of Philosophy in Biomedical Engineering

University of California, Irvine, 2018

Professor Zhongping Chen, Chair

Mechanical elasticity often serves as a major indicator for pathological changes in ocular as well as intravascular diseases. For example, age-related macular degeneration is an ocular disease that occurs in the posterior eye, where central vision gets damaged due to drusen formation and neovascularization. The mechanical elasticity of the tissue is often altered during the onset of disease before structural changes are detectable with existing technologies. It is necessary to detect these changes early and provide timely treatment due to either the irreversible nature of the disease progression or the fatal consequences associated with late diagnosis. This thesis focuses on the development of an acoustic radiation force optical coherence elastography (ARF-OCE) system to map the mechanical elasticity of tissues, and the translation of this laboratory technology to in vivo animal studies. This technique uses ultrasonic excitation to apply a force onto the tissue and optical coherence elastography to detect the spatial and frequency responses of the tissue, which combines to quantify the elasticity and provide an elasticity map. The resonance frequency method is validated and used to measure the bulk modulus of the tissue while a Voigt spring model calculates the individual layer elasticity. We first test the feasibility of the system using tissue-mimicking phantoms. Then we perform tissue imaging on the ex vivo anterior and posterior eye, where we are able to provide quantified elasticity maps of the rabbit cornea and porcine retina The system is then translated to in vivo imaging, for which quantified elasticity mapping of the rabbit retinal layers can be obtained. In addition, we have also fabricated an ARF-OCE catheter with a diameter of 3.5 mm, which was validated using phantom studies, and intravascular imaging was performed on a human cadaver artery. This study is a major stepping stone to the translation of the ARF-OCE technology in measuring the mechanical properties of tissues in clinical settings. Future studies using this technology include monitoring the retinal elasticity during and after electrode stimulation treatment and also intravascular elasticity imaging to diagnose atherosclerosis.

CHAPTER 1

Introduction

1.1 Retinal diseases

Mechanical properties, such as the elasticity and viscosity, are often major indicators of diseases. The stiffness of tissue changes in unison with the onset of pathology in the cases of cardiovascular diseases, ocular diseases, and tumor formations. The cellular composition of the tissues is altered over time, in tune with disease progression. However, the reported stiffness of a specific type of cell or tissue differs greatly depending on the type of imaging modality used and the experimental conditions. In order to accurately distinguish the diseased tissues from healthy ones, it is necessary to validate the results through both theoretical and experimental methods.

Age-related macular degeneration (AMD) is one of the leading causes of blindness in the North American and European population over the age of 60 years (1, 2). Approximately 1.7 million Americans over 65 years of age have visual impairment due to AMD, according to the statistics provided by the NIH National Eye Institute. Since vision directly impacts the quality of life in the aging population, it is essential that this condition is diagnosed and treated in its early stages.

The retina is a light sensitive layer at the posterior section of the eye that is responsible for converting and sending visual signals to the brain. Although the layer is only approximately 200 - 300 um thick, it has many sublayers that contribute to its function as shown in Figure 1.1 (3). AMD is a retinal disease that is classified in stages. Early stage AMD occurs when changes in the macular pigmentation occur and drusen, which is a yellow-colored focal deposition of acellular polymorphous debris, forms in the retina, and contribute to blindness. These deposits, which can grow to over 125 um in size, are most often located between the basal lamina of the retinal pigment epithelium (RPE) and the Bruch's membrane as depicted in Figure 1.1 (4). In the late stage progression of AMD, neovascularization and atrophy of the retina occur, as well as overt loss of central vision (5). The early stages of AMD are often known as "dry" macular degeneration, referring to the drusen, while the latter stages are "wet" due to the vascularization.

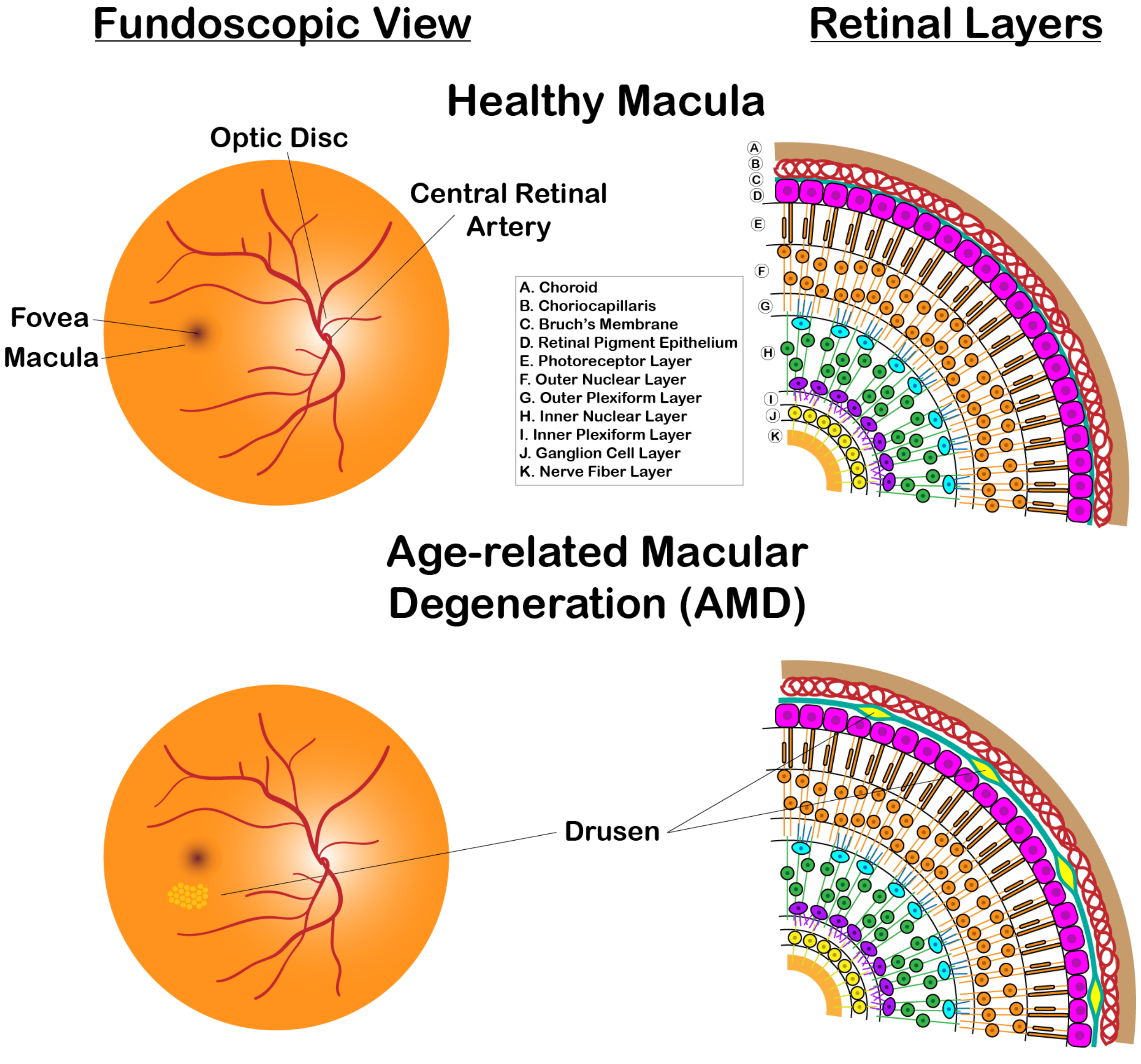

Figure 1.1 Dry-form AMD.

In order to diagnose AMD, fundus imaging, angiography and optical coherence tomography (OCT) techniques have been used (6, 7). The *en face* surface anatomical information along with the blood vessel formations, and the blood flow dynamics, can be obtained with fundus imaging and angiography, respectively. OCT is a relatively newer imaging modality that can visualize the entire depth of the retina, especially subsurface structures associated with the retina and even the choroid (8). With these modalities, the anatomical structures of the retina have been studied extensively. However, in many cases, it is still challenging to diagnose the early stages of AMD during the beginning of drusen formation when there is a stiffening of tissue, but tissue morphology change is not visible by conventional imaging techniques.

The elasticity of the ocular tissue will change during the onset of AMD, possibly as a precursor to neovascularization (9). Elasticity changes in the retina and choroid can occur when the microvasculature changes or when drusen forms. In order to study the mechanical structure of the retina, several studies attempt to provide elastic properties by performing mechanical strain testing *in vitro* (10, 11). However, testing is not currently available for tissues *in vivo.* In addition, the entire retina is extracted as a single unit, which means that information for the individual layers cannot be obtained. Other studies turn to mathematical modeling of the retina to determine the Young’s modulus, which is the standard measurement of stiffness (12).

1.2 Cardiovascular diseases

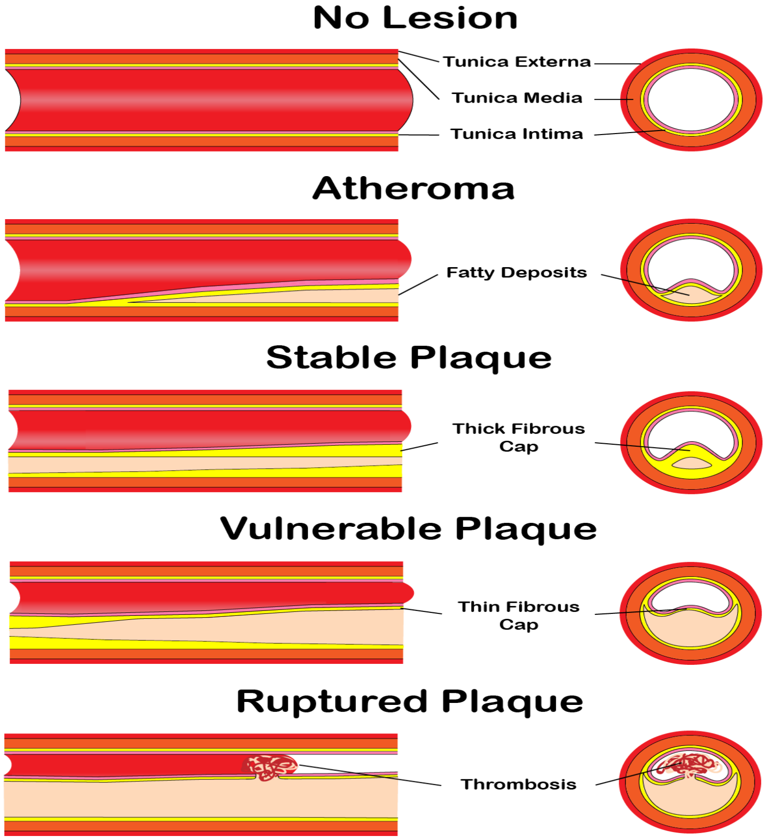

Figure 1.2 Atherosclerosis in arteries.

Cardiovascular diseases have the highest rate of fatalities and account for 30.8 % of all deaths in the United States (13, 14). Atherosclerosis, accounting for 41 deaths per day, is a cardiovascular condition that is associated with changes in the composition of the blood vessel walls. A healthy blood vessel consists of 3 layers in the vessel wall, including the tunica intima, tunica media, and tunica externa as shown in Figure 1.2. During the early onset of disease or atheroma, the walls of the artery thicken due to fatty deposits, inflammation, cells, and scar tissue build up (15, 16). Eventually, the lesions that form, often known as plaques, are composed of distinctive necrotic cores and a fibrous cap. If the plaque is stable with a relatively thick cap and small lipid core, there may be varying degrees of obstruction to blood flow. However, in the case of a vulnerable plaque, the cap, containing collagen and smooth muscle cells, becomes less than 65 um, and can rupture easily. When there is a plaque rupture as shown in Figure 1.2, the inflammatory elements of the necrotic core bursts into the artery, and can cause blocked arterial flow, angina, or even myocardial infarction (17, 18).

Early detection of vulnerable plaques is essential to the health and safety of cardiovascular patients. The structure and composition of the plaque is largely used currently to determine its vulnerability. Current clinical imaging techniques include angiography, angioscopy, ultrasound, and magnetic resonance imaging (MRI) (19, 20). Angiography allows the physician to visualize the region of blockage, by inserting a dye into the bloodstream and observing the mechanism of flow (21). Angioscopy helps to examine the surface of the interior blood vessel to identify areas of damage and abnormality (22, 23). Ultrasound and MRI allow for the visualization through the depth of the blood vessel walls, at the expense of resolution and cost, respectively (24). Due to limitations of the current imaging modalities, they cannot effectively identify vulnerable plaques with high sensitivity and specificity (19, 20). Since the change in the composition of the blood vessel wall is indicative of the early onset of atherosclerosis, it is possible to classify vulnerability according to the composition. Plaques can be differentiated into 3 different types: lipid, fibrous, and calcified. The mechanical stiffness of these three components differs by nearly one order of magnitude (25-27). Therefore, if the stiffness of the tissue can be measured, the composition can be determined, and vulnerable plaques can be isolated.

Mechanical testing methods have been used to observe the differences in the stiffness of lipid, fibrous, and calcified plaque components (28-30). However, these tests require the extraction and manipulation of the tissue, which is not possible for *in vivo* imaging. It is necessary to understand the change in tissue elasticity *in-vivo* during the early onset and formation of plaques in order to accurately assess the mechanical properties under the influence of natural environmental factors (23, 25, 26, 31). The feasibility of such measurements is limited by the resolution and accuracy of the measurement devices, size of the device, and the accessibility of the plaque in question.

1.3 Elasticity imaging

Tissue elastography is a method that has been developed to map out the mechanical properties of tissues (32, 33). There are typically three steps involved as depicted in Table 1.1: excitation, detection, and parameter estimation (34-36). The tissue is first excited using an internal or external mechanism, where the tissue itself or an outside force causes deformation (36). The force can be either static or dynamic in nature, depending on the variable to be measured. For example, a few external methods include piezoelectric elements, air puff devices, and acoustic radiation force (ARF) using ultrasound transducers. All of these devices can operate by giving static, continuing force to analyze a stable deformation state, or by providing a single or modulated dynamic signal of pulses to analyze the change in deformation over time. Once the tissue is deformed, a technique is used to visualize and measure the amount of deformation. Traditionally, mechanical testing using pressure sensors were used to obtain data in *ex vivo* samples. Magnetic resonance and ultrasound methods have also been used to detect tissue deformation at the expense of high cost and low resolution, respectively. In recent years, optical imaging methods, such as optical coherence elastography, have been developed to detect tissue response (37-45). In particular, Doppler OCT has been widely used for detection, with its main advantages being its high resolution and the high phase sensitivity.

Excitation		Detection	Parameter Estimation
Internal	External	Mechanical Test Magnetic Resonance Ultrasound Optical	Quantitative Qualitative
Static	Dynamic		

Table 1.1 Elastography in three steps.

Most parameter estimation methods target the extraction of elasticity by the means of elastograms or elasticity maps (37-45). Research has also been done to observe other mechanical properties, such as the viscosity (46-48). The parameter estimation can be either quantitative or qualitative. Qualitative methods allow users to obtain relative values for mechanical properties and can be beneficial for the comparison between healthy and diseased tissues. However, there are often problems with the calibration accuracy of the system, and environmental and systematic changes between measurements, that limit the functions of qualitative data. Due to these factors, quantitative measurements with strong theoretical evidence are always preferred. A few examples of quantification include shear wave velocity calculations, strain imaging, and tissue frequency response (49-53). Select methods will be discussed in detail in the next section.

In order to perform *in-vivo* real time imaging with information of different retinal layers, while accounting for perfusion and intraocular pressure, a fast functional imaging system is necessary. Ocular optical elastography is a relatively new method of providing elasticity mapping with high resolution and sensitivity (37). Several applications have been studied using this technique, including the cornea (54-56). However, the mechanical properties of the retina are still not well defined since the retina is inaccessible to many elastography methods. Therefore, a technology using acoustic excitation and optical detection can possibly help scientists and physicians better understand the mechanisms of AMD *in-vivo*, specifically the changes in tissue elasticity, in order to more accurately diagnose and track the progression of the disease in its natural setting.

Intravascular elastography using ultrasound has been widely studied in the past 20 years (23, 57-59). In general, a pressure is applied to the artery, and ultrasound is used for detection of tissue displacement, which is then converted to strain measurements and an elastogram can be generated. Examples of ultrasound elastography techniques include compression strain imaging and phase-sensitive speckle tracking methods based on cross-correlation analyses (58). *In vivo* intravascular ultrasound elastography studies have also taken place in the past years, along with modeling methods such as finite element analysis (60-62). However, these methods are often limited by the low ultrasound resolution of typically 150-300 um, which allow for the detection of homogenous plaque types, but restrict the observation of heterogeneity within small regions, which is the case for most human plaques (63). In addition, most vulnerable plaques are characterized by thin fibrous caps, as little as 65 um in thickness, which cannot be accurately measured using ultrasound (17). Using optical methods, with micron-level resolution, it is possible to detect minute changes in tissue elasticity within a small region. Finally, due to the nanometer sensitivity of phase resolved methods, only small forces are necessary to induce vibrations, which is critical in *in-vivo* clinical applications.

OCE is a technology that uses the principles of OCT to detect the tissue response to excitation. OCT is based on the interference of the back-scattered light signals of the sample and a reference mirror (8, 64). In regards to OCE, an excitation force, most often external, is applied to the tissue, while the optical interference information is extracted (34, 40-45, 65-67). The information provided can be used to measure the tissue response by using parameters such as phase resolved method and Doppler variance methods, depending on the type of parameter estimation.

There are primarily 2 types of tissue responses, which rely on elastic wave properties, studied using OCE: the p-wave and the s-wave (68). When a force is exerted on a sample, the first response consists of the p-wave, also known as the compressional wave, traveling across the sample parallel to the direction of the force. The p-wave travels at a high speed and essentially compresses the sample as it passes, providing the relative Young's modulus of the penetration region. The s-wave, also referred to as the secondary or shear wave, travels perpendicularly to the direction of the initial force and is approximately 3 orders of magnitude slower than the p-wave (69). The s-wave is directly related to the shear modulus. There are primarily two different methods of parameter estimations, including Doppler OCE using the p-wave measurements to obtain the elastic modulus and velocity extraction using s-waves to obtain the shear modulus.

1.4 Summary of chapters

In this dissertation, acoustic radiation force optical coherence elastography (ARF-OCE) is developed for ocular and cardiovascular applications and has been translated from benchtop testing to in vivo animal studies. The system measures the mechanical elasticity of tissues by applying a compressional wave or force on the sample and measuring the frequency and amplitude of the tissue vibrations. The technique provides synchronized excitation and detection, real-time image acquisition, and quantified spatial mapping of tissues. This technology addresses a current unmet need in medicine and overcomes the limitations on existing technologies. Brief summaries of the chapters are given below.

Chapter 2 introduces OCE in detail. First, the principles of time-domain and Fourier-domain OCT are discussed, and then focuses on the alignment and calibration of SD-OCT. The principles of ARF are described, and the technologies are combined to introduce the ARF-OCE system.

Chapter 3 presents the corneal imaging project using a basic ARF-OCE system, proving the feasibility for ocular elasticity mapping. Phantom studies as well as ex vivo tissue studies are performed and the results of healthy versus cross-linked tissue are analyzed.

Chapter 4 discusses the resonance frequency approach to imaging and quantifying ocular tissue, stepping away from the relative elasticity measurements presented in the previous chapter. Phantom calibration is done and the results are validated with mechanical testing. Ex vivo porcine and rabbit ocular samples are studied, and the elasticity of tissue is measured with varying intraocular pressure.

Chapter 5 focuses on retinal layered elasticity mapping, with the addition of a synchronized, quantified approach. First system synchronization is achieved by timing the excitation and detection simultaneously. Then ex vivo retinal images are acquired using a porcine model. Quantification and data analysis are performed by segmenting the ocular layers and applying a spring model to isolate individual layers.

Chapter 6 presents the first in vivo ARF-OCE imaging of retinal layers and the mechanical quantification of each layer, showing the feasibility of translating the technology for in vivo imaging. The healthy rabbit eye is imaged in vivo at different locations on the central retina and statistical analysis is performed. A diseased retinal degeneration model is also established and the change in mechanical elasticity is tracked. Limitations of the in vivo system for clinical translation are also discussed.

Chapter 7 introduces the first intravascular ARF-OCE system, including the front-facing probe design and fabrication. Phantom validations were performed and ultimately, a cadaver human carotid artery segment was imaged, where an elasticity map was obtained and different plaque components were identified.

Chapter 8 summarizes the work that is presented in this dissertation from basic imaging to in vivo, real-time, quantified elasticity mapping. Finally, future research directions including retinal stimulation OCE and in vivo intravascular OCE are presented with preliminary results.

CHAPTER 2

Optical Coherence Elastography

In this chapter, we introduce the basic concepts of the optical coherence elastography imaging system. First section 2.1 covers the principles of optical coherence tomography, including the transition from time-domain to frequency-domain systems. Section 2.2 explores the spectrometer based OCT in more depth, specifically the hardware alignment and software calibration. Next, the principles of ARF based on ultrasound are discussed in section 2.3. In section 2.4, the excitation and detection of the system is combined to introduce the phase-resolved ARF-OCE technology. The elasticity quantification method is discussed in section 2.5, and the chapter ends with a summary in section 2.6.

2.1 Principles of optical coherence tomography

OCT is an emerging technology in ophthalmology and cardiology, achieving a non-invasive, non-ionizing method of micron resolution imaging. OCT uses a coherent source to measure the optical backscattering from tissue and other samples (8, 64). OCT is able to provide cross-sectional views of tissues and 3 dimensional volumetric imaging. Just as ultrasound uses the propagation of sound and its interaction with tissue, OCT relies on the transmission of near-infrared light. With a resolution of ~2-15 um and an imaging penetration of 1-2 mm in tissue, OCT has been widely studied for in vivo and clinical applications (8, 64, 70, 71).

OCT was first introduced to ophthalmic imaging in 1986 and has since gained popularity in the area of retinal imaging. The technique is based on the Michelson interferometer shown in Figure 2.1a (8, 72). A coherent light source emits light that is split by a beam splitter. A portion of the light is reflected on to the first mirror and the rest is transmitted toward the second mirror. The light from both mirror is directly reflected back over the same path toward the beam splitter. The light paths combine and the interference signal is picked up by the detector. The imaging axial location of the tissue depends on the path length difference between the 2 mirrors. The first OCT system was based on the time-domain (TD) design as shown in figure 2.1b. The second mirror is replaced by a tissue sample in the sample arm and since depth information is required, a moving mirror reference arm is introduced, most often via mechanical scanning methods. The mirror oscillates from the beam splitter and changes the path length between the sample and reference arms depending on the axial location of interest.

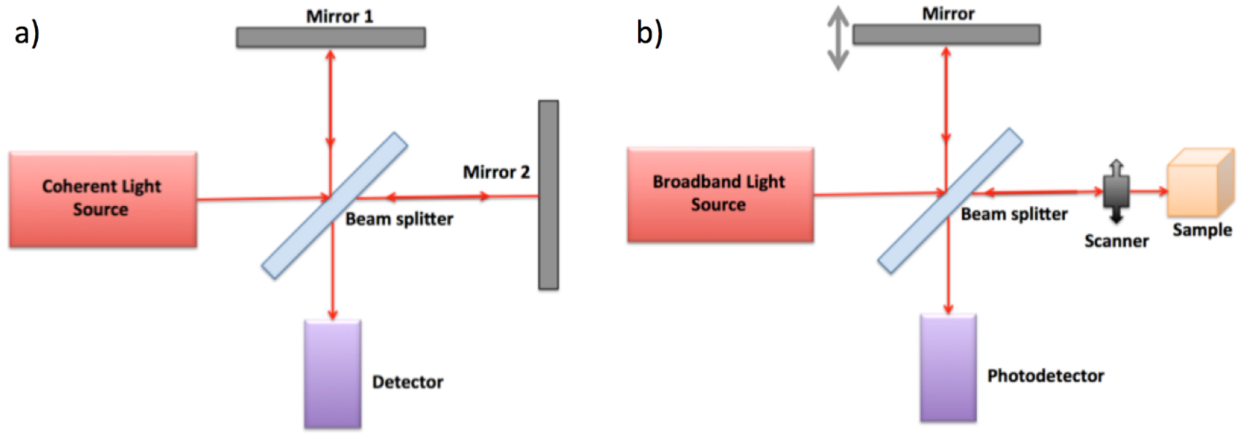

Figure 2.1 a) Michelson interferometer, b) Time-domain OCT.

To illustrate the theory of OCT, the electric field of back scattered light from the reference mirror and sample arm reflectors 1 to N are described below as E_r and E_s respectively.

$$E_r(k,w) = cS(k,w)r_r e^{j(2kz_r - wt)} \qquad \text{(Eq. 2.1)}$$

$$E_s(k,w) = (1-c)S(k,w)\sum_{n=1}^{N} r_s(z_n)e^{j(2kz_n - wt)} \qquad \text{(Eq. 2.2)}$$

Where S denotes the power of the laser source, and c denotes the ratio at which the light is split from the laser to the reference arm. z and z_r are optical path length determined by the position of sample arm reflectors and reference mirror. Function r_s represents sample reflectivity along axial direction, while r_s denotes the reflectivity of reference mirror. The angular frequency of the light is denoted by w. Accordingly, the power of interference between reference and sample light can be given by equation 2.3.

$$S_i(k) = cS(k)r_r + (1-c)S(k)\sum_{n=1}^{N} r_s(z_n) \tag{a}$$

$$+\sqrt{c(1-c)}S(k)\sum_{n=1}^{N}\sqrt{r_s(z_n)r_r}\, cos\, 2k(z_n - z_r) \tag{b}$$

$$+(1-c)S(k)\sum_{m\neq n=1}^{N}\sqrt{r_s(z_n)r_s(z_m)}\, cos\, 2k(z_n - z_m) \tag{c}$$

(Eq. 2.3)

Where three components, include DC term, cross-correlation (CC) term and auto-correlation (AC) term, can be identified in Eq. 3a, 3b and 3c respectively. To be specific, DC term is the summation of light power from both arm, AC term represents the self-interference signal from sample arm, and CC term denotes the interference between sample and reference arm. The angular frequency term is eliminated from the phase of the light because its frequency usually exceeds the cut off frequency of the photodetector. In the case of OCT imaging, the depth resolved information is achieved by canceling AC and DC term first, and then de-correlating the cross-correlation component to retrieve the axial profile of sample reflectivity.

$$I(z) = \frac{\rho}{4}\left[S_0\left(cr_r + (1-c)\sum_{n=1}^{N} r_s(z_n)\right)\right] \tag{a}$$

$$+\frac{\rho}{2}\left[S_0\sqrt{c(1-c)}\sum_{n=1}^{N}\sqrt{r_s(z_n)r_r}\, e^{-(z_n-z_r)^2\Delta k^2} cos\, 2k_0(z_n - z_r)\right] \tag{b}$$

(Eq. 2.4)

For time domain OCT, the output detector current can be obtained by integrating the signal over k and the signal for each individual depth can be obtained as shown by equation 2.4, where $S_0(z) = \int S(k)dk$, ρ is the responsivity of the detector, Δk is the range of wavenumber, and k_0 is the central wavenumber. For TD-OCT, an A-line can be obtained based on the interference amplitude at each z location by moving the mirror. For 3D scanning and rendering, it is necessary to add a scanner on the sample arm to navigate the light beam across the volumetric space. A-lines are taken at every point and pieced together to create a B-scan, which is then combined to render a 3D image.

The primary limitation of TD-OCT is the scanning speed of the reference mirror. With mechanical methods, it is difficult for imaging to exceed 10 frames per second, which is below the scanning speed required for most in vivo applications. For example, breathing movements and reflex motions make it difficult to image for long periods of time. Therefore, Fourier domain (FD) OCT was discovered and has become a necessary commodity in ophthalmology (8, 64).

FD-OCT is split into 2 designs: swept-source (SS) OCT and spectral-domain (SD) OCT. FD-OCT uses a stationary reference mirror and analyzes the interference pattern with respect to the wavenumber in k-space. Fourier transform is performed to convert the frequency information in k-space to depth information for a single A-line. In order to use a range of wavelengths corresponding to the wavenumbers, SS-OCT replaces the light source with a swept-source laser, which sweeps over a broad spectrum of light to calculate the interference. SD-OCT uses a similar principle but instead of a swept laser, it uses a broadband laser while the wavelengths are separated using a diffraction grating in the detector portion. FD-OCT offers faster imaging and higher SNR than its TD-OCT counterpart. SD-OCT is chosen for this study due to its high phase stability associated with having no moving parts.

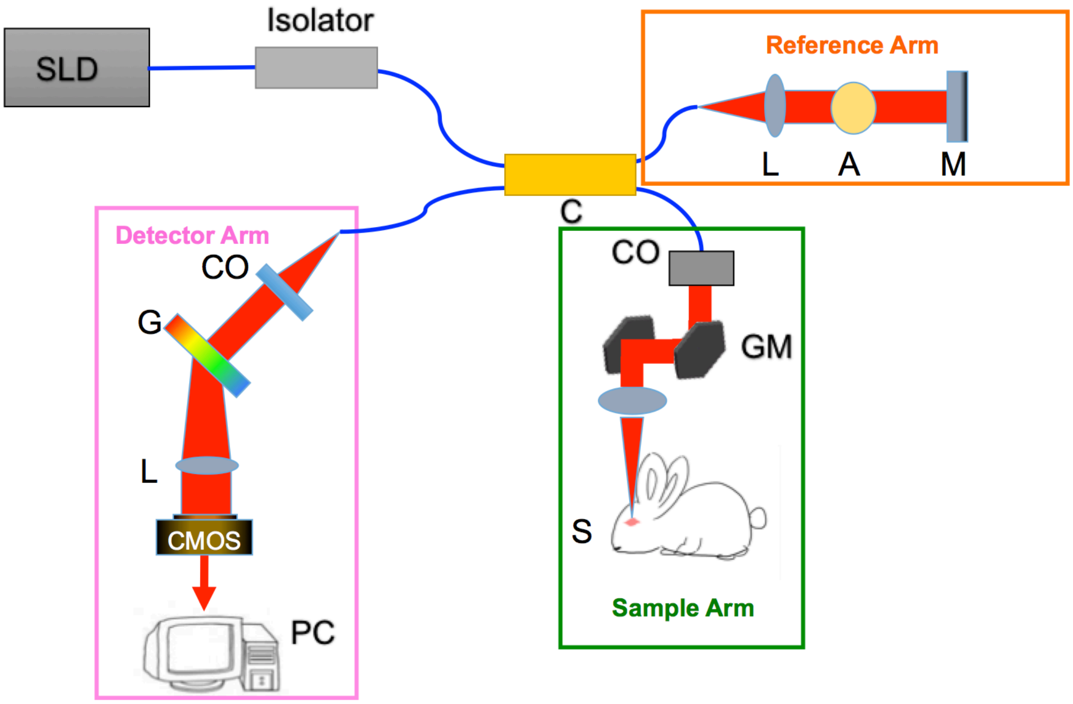

Figure 2.2 Schematic of SD-OCT system.

The basic schematic diagram of a SD-OCT system is shown in Figure 2.2. A broadband SLD source emits near-infrared light and an isolator guides the light in a forward direction to avoid laser damage associated with strong back reflections. A 2x2 coupler is used to couple the low coherence light from the SLD laser into a fiber-based Michelson interferometer. The light is split into the sample and reference arms. In the reference arm, the light is collimated, attenuated, and reflected directly back with a mirror through the same path. The light in the sample arm is collimated, focused onto the sample, and the backscattered signal is collected. A galvanometer is often used for fast and accurate 2D scanning. The back-reflected light from the sample arm and reference arm is collimated and dispersed by a diffraction grating. Finally it is focused onto a line scan CMOS or CCD camera by an achromatic lens. When the path lengths of the sample and reference arms are matched, the light will interfere and the camera will collect and digitized the interference spectrum as described by Eq. 2.3.

To obtain cross-correlation component, DC term is first extracted and removed by averaging the interference fringes across consequent A-Scans, while AC term is simply ignored because it is usually too weak to be detected. Fourier transform will then be performed to de-correlate the cross-correlation signal as shown in Eq. 4 below. The wave number and the depth resolved signal are a Fourier transform pair. This transforms the interference spectrum from k-space, which is based on the intensity at different wave numbers, to an A-line with depth information. The Fourier transformed signal is separated into two separate signals for two symmetrical images.

$$I(z) = \mathcal{F}^{-1}(\sqrt{c(1-c)}S(k)\sum_{n=1}^{N}\sqrt{r_s(z_n)r_r}\,cos\,2k(z_n - z_r))$$

$$= \sqrt{c(1-c)}S(z)\otimes \textstyle\sum_{n=1}^{N}\sqrt{r_s(z_n)r_r}\left(\delta(\mathrm{z} + 2z_n - 2z_r) + \delta(\mathrm{z} - 2z_n + 2z_r)\right) \qquad \text{(Eq. 2.5)}$$

Equation 2.6 rewrites the interference intensity expression in terms of its magnitude and phase information, where $\phi(z)$ refers to the phase at depth z.

$$I(z) = |I(z)|e^{j\phi(z)} \qquad \text{(Eq. 2.6)}$$

The magnitude of the interference signal determines the intensity of the A-line at depth z and is used to construct the OCT image. The phase term can be extracted to yield the tissue displacement information using Doppler OCT methods, and will be discussed in section 2.4.

Since OCT focuses on using low coherence light sources, constructive interference between the sample and reference arms can be extracted only within a coherence length window, L, defined as:

$$L = \frac{2ln2}{\pi}\frac{\lambda^2}{n\Delta\lambda} = 0.44\frac{\lambda^2}{n\Delta\lambda}$$

(Eq. 2.7)

where Δλ is the bandwidth of the source and n is the refractive index of the tissue. The coherence length is also defined as the axial resolution of the OCT system.

Alternatively, the lateral resolution, Δx, of the system is dependent on the focusing lens at the sample arm. In equation 2.8, the F# or F number is a unique property of the lens and is defined to be the focal length, f, divided by the beam size, D.

$$\Delta x = 4\frac{\lambda F\#}{\pi} = 4\frac{\lambda f}{\pi D}$$

(Eq. 2.8)

There are always trade-offs between different optical properties, such as the lateral resolution and the focal length. Depending on the specific application, a most suitable OCT system can be designed. For ophthalmic imaging, we require low water absorption due to the high water content in the eye, so a lower wavelength is necessary. In addition, elastography utilizes Doppler OCT methods, which calls for high phase stability, so SD-OCT is the prime candidate with no moving parts.

2.2 SD-OCT alignment and calibration

Two major challenges of SD-OCT are the spectrometer alignment and k-space calibration. Since commercial SD-OCT systems often do not allow for customization for incorporating

ARF excitation, specifically the signal synchronization algorithm and the hardware compensation for imaging in fluid, it is necessary to build a custom SD-OCT system. The schematic is similar to the one shown in Figure 2.2, and a picture of the optical system is presented in Figure 2.3. This system is placed in a shock-proof metal box for portability and stability.

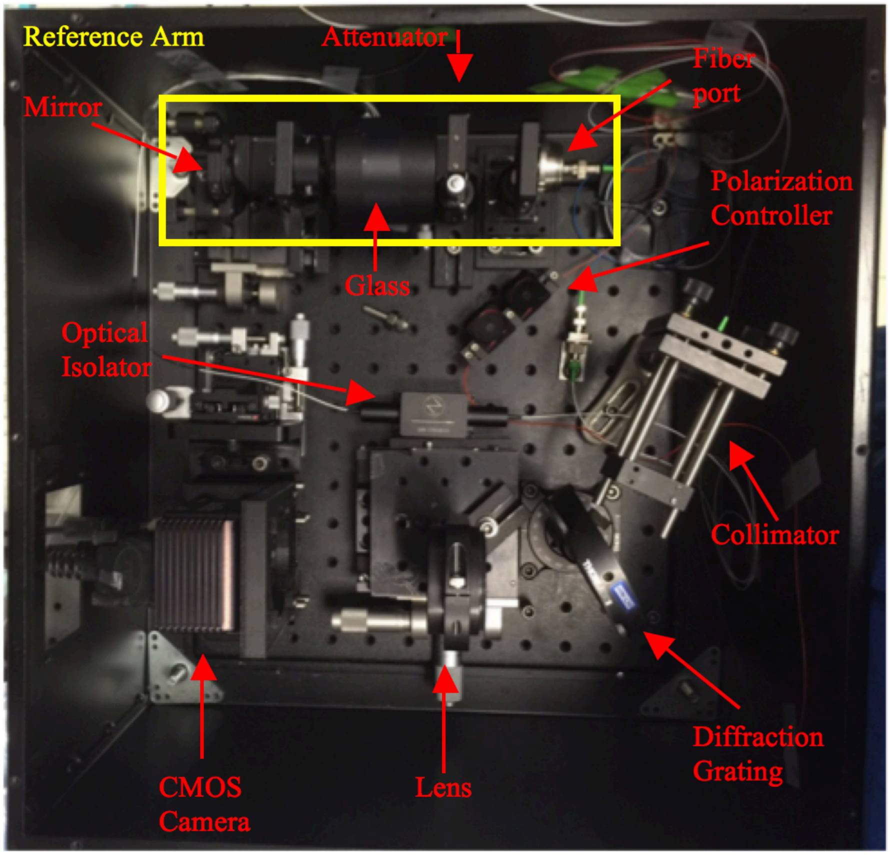

Figure 2.3 Picture of SD-OCT components in a box.

The alignment process is concentrated on the detector arm, where the light must be directed from the collimator to the camera detector. The wavelengths are separated with a 1200 slits/mm diffraction grating and focused onto the camera with a 100 mm or 150 mm lens. The primary challenge is getting the diffracted segment of light directly onto the 4096 line-scan camera pixels. For ocular OCT, where retinal layers are visualized, it is important to have high axial resolution in the system. According to equation 2.7, this means that we need a lower central wavelength and large bandwidth. The central wavelength is determined to be 890 nm due to its low water absorption in the eye and the bandwidth should be larger than 150 um to yield a resolution of ~3 um. The wide bandwidth requires more pixels on the line-scan camera, which results in more difficulty aligning the system.

For system alignment, the reference arm, which is boxed in yellow in Figure 2.3, is first aligned so that the light from the fiber connector is collimated and reflected back directly with a mirror. Once the reference and sample arms both have backscattered signal, the detector arm can be setup. The diffraction grating has entrance and exit angles both at 31 degrees, so the light that comes out of the collimator must be at 31 degrees with the grating, and same with the lens after the grating. The easiest way to do this is to keep the lens straight on the detector axis and angle the grating 62 degrees from there. Then place the collimator straight with respect to the angled grating, which would be 62 degrees from the central axis. Next tune the angle to 31 degrees, and the grating should be at 31 degrees from both the lens and the collimator on opposite sides. The camera will be placed at the focal plane of the lens, and the height of the collimator, lens, and camera should be matched as closely as possible. The grating must be aligned vertically so that the light diffracts on the same horizontal axis. Finally, the camera must be aligned with a 5 axis translational and angled stage so that the line of light is focused directly onto the pixels with minimal distortions.

To verify the system alignment, it is necessary to check the system spectrum using just the reference mirror as shown in Figure 2.4a. Once the spectrum closely resembles that of the laser source spectrum based on the optical spectrum analyzer, the system is aligned properly. The interference spectrum can be obtained by using a mirror on the sample arm and matching the lengths of the sample and reference arms. The interference spectrum for our custom SD-OCT is shown in figure 2.4b, where the high frequency interference can be visualized. At this point, OCT images can be obtained by doing FFT on the interference signal.

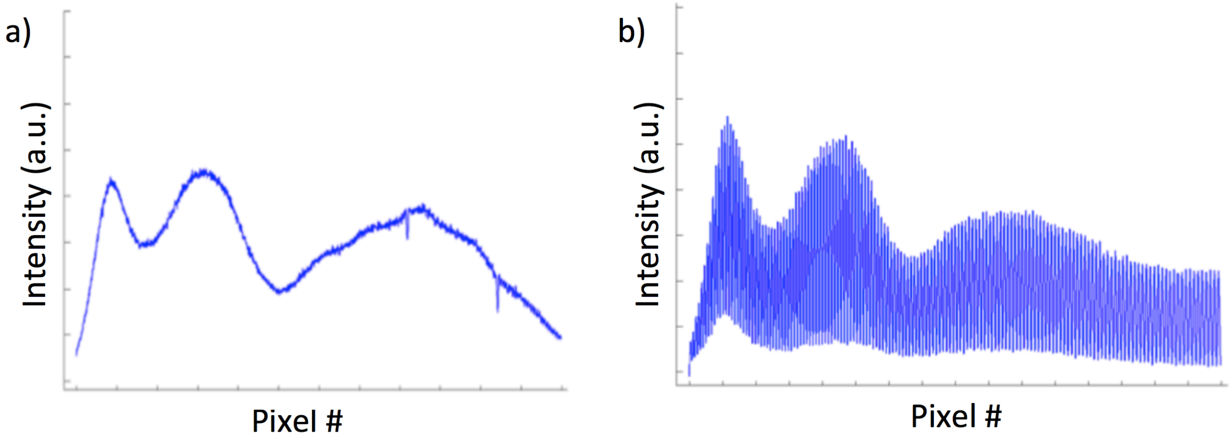

Figure 2.4 a) Raw system spectrum from reference mirror. b) Interference spectrum with sample and reference mirror interference.

Even with perfect detector arm alignment, chromatic aberration, dispersion, and calibration are major issues associated with SD-OCT. All three degrade the imaging quality by affecting primarily the axial resolution. Chromatic aberration is caused by minute differences in the focal distance associated with different wavelengths. While choosing the hardware components, it is important to use achromatic lens and collimators, which will solve the bulk of the issue.

Dispersion is another issue that is especially prominent in our application due to imaging in a fluid medium. Dispersion is a result of the light traveling in different mediums, such as air, glass, or water, in the sample and reference arms, where different wavelengths have inconsistent propagation paths. The result is a drift in the frequency of the interference fringe at every path length-matched location. Figure 2.4b demonstrates this effect with a higher frequency on the lower pixels and a lower frequency on the higher ones. A portion of the problem can be resolved by matching the light propagation distance in air for the sample and reference arms, and also using glass plates as shown in figure 2.3 or water cuvettes on the reference arm while the sample is submerged in fluid. However, it is often impossible to perfectly match the light propagation paths between the two arms using solely hardware, so software compensation is also necessary.

Using a broadband light source and a diffraction grating to separate the wavelengths, it is important to note that the signal of each pixel on the line-scan camera detector may not correspond linearly with the band of wavelengths that is used. Therefore, it is necessary to calibrate the wave numbers in k-space to correspond linearly with the pixel acquired. Software methods should be used to perform k-space calibration.

We will now discuss the calibration and dispersion compensation algorithms. The axial resolution of OCT is defined by the full width half max (FWHM) of its axial point spread function (PSF). According to the theory of OCT, the PSF of OCT can be given by the response of an infinitely thin sample, yielding a sinusoidal waveform in wavenumber space with a single frequency. However, the spectrometer of the SD-OCT system does not sample the OCT interference at equal interval of wavenumber, because the gratings disperse different wavelengths linearly onto the spectrum detector, but not the eavenumber. In addition, the medium mismatch between reference and sample arms may introduce dispersion across the bandwidth, and thereby degrade the PSF as well. Both of them can cause the distortion of the sine wave, which is the Fourier transform of the PSF, and also deteriorate the axial resolution of OCT. Therefore, it is necessary to linearize the wavenumber axis and compensate for the optical path medium mismatch, also known as k-space calibration and dispersion compenstation.

The main idea of k-space calibration is to find the function that maps the distorted wavenumber axis to its linear form, and thereby resample the interference at equal wavenumbers. A traditional way to correct the distortion is to use the interference signal of a mirror, assuming all the light is reflected only by its surface. Upon this assumption, the interference fringe is supposed to be a pure sine wave whose instantaneous phase is increasing linearly with the wavenumber. Taking advantage of this linear relationship, we are able to restore the linearity simply by resampling the interference waveform at equal phase intervals. To be specific, we perform a Hilbert transform on the mirror interference fringe and obtain the analytical form where instantaneous phase can be extracted. After that, the phase vector is resampled at equal intervals and its corresponding resampling coordinate is stored for further calibration. Especially for the phase resampling, a nonlinear regression model, using the power of the PSF as a merit function, can be used to precisely fit the phase vector as a function of wavenumber and eliminate random noise that may compromise the resample (73). Finally during OCT imaging, we re-register the interference signal by interpolating values at the resampling coordinate to ensure equal wavenumber intervals.

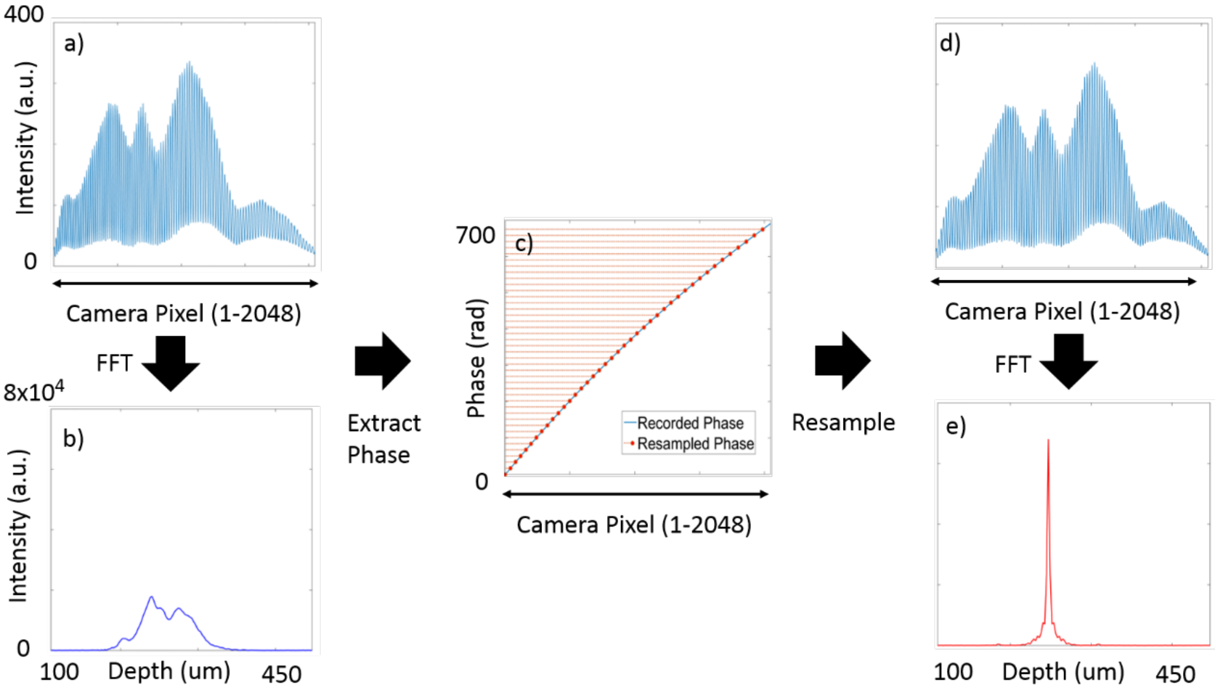

Figure 2.5 Flow chart of k-space calibration. a, d) Self interference signal of a cover glass before and after calibration. b, e) The FFT of self-interference signal before and after calibration. c) Instantaneous phase resampled at equal phase intervals.

Although this technique is able to calibrate for the nonlinear sampling issue of the wavenumber, it cannot account for the dispersion. More over, the wavenumber dependent phase delay caused by dispersion may deteriorate the linear relationship between the wavenumber and the phase of a mirror's interferogram, and hence compromises the effectiveness of the calibration. To solve this problem, we propose using the self-interference term of OCT for k-space calibration (73), inspired by the fact that it is free of dispersion. Specifically, a transparent cover glass, with approximately 200 um thickness, is first placed under the scan head of the sample arm while the reference arm is blocked. Then the two surfaces of the cover glass will reflect light back and interfere with each other to generate the self-interference signal with a pure sine wave fringe. Since the optical transmission mediums for the light from both surfaces are equivalent, there is minimal phase delay in their interference spectrums. By using this dispersion-free fringe, it can linearize the wavenumber axis with the k-space calibration algorithm. Figure 2.5 demonstrates the general process of this technique.

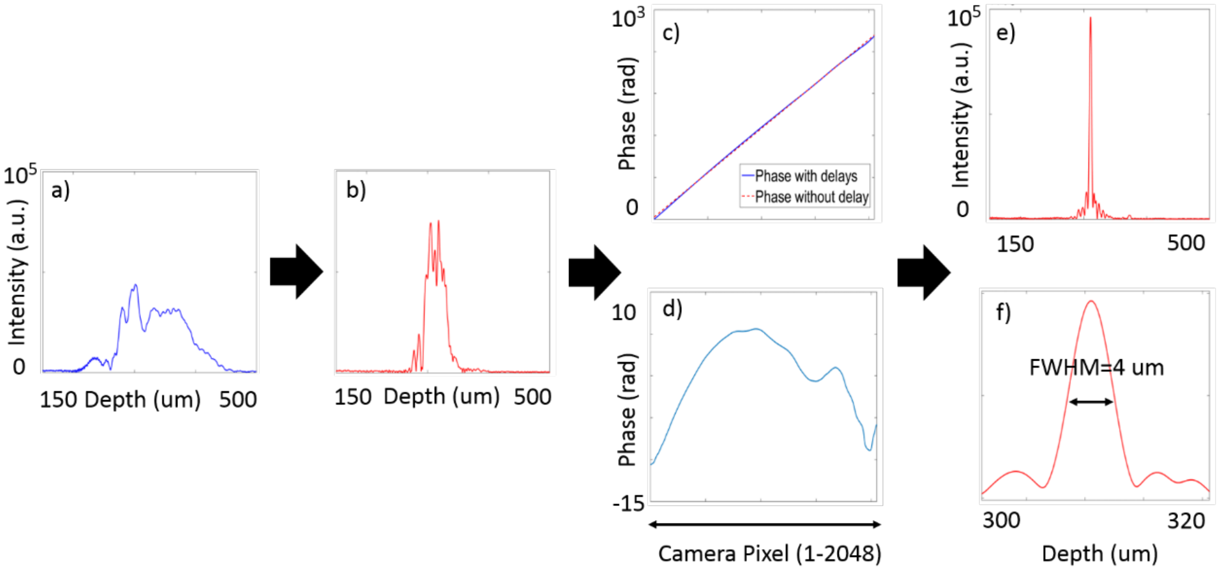

Figure 2.6 Flow chart of dispersion compensation. a) PSF of a mirror's interference signal digitized by line scan camera. b) PSF after k-space calibration. c) Blue line illustrates the phase of the calibrated signal, red dotted line is the first order component of its polynomial fit. d) Quantified wavenumber dependent phase delay, calculated by subtracting the first order component from the phase of the calibrated signal. e, f) PSF and its zoomed in view after dispersion compensation.

Although it is possible to bypass dispersion using the self-interference term, we cannot expect a highly sensitive self-interference signal during tissue imaging due to the lack of a highly scattering surface within the sample. To get rid of the dispersion in the OCT interference, we will need to quantify the phase delay across the bandwidth and correct them during real time imaging. Again, a mirror object is used to generate an interference fringe with linearly increasing phase over wavenumber. K-space calibration should be firstly performed to re-register the interference signal with a linear wavenumber. Then the phase of the calibrated fringe is fed to a polynomial model to fit for the first order component, which is given by the signal from the mirror surface. By eliminating the phase component induced by the mirror interference, the wavenumber dependent phase delays can be finally obtained and used for phase correction during real time imaging. The process of dispersion compensation can be briefly summarized by figure 2.6.

2.3 Principles of acoustic radiation force

ARF is non-invasive, non-contact, and fast, which makes for an ideal tool in *in vivo* applications. ARF, which is based on high-powered ultrasound, uses acoustic principles to exert a force on the sample. An acoustic wave is emitted from the ultrasonic transducer and is primarily absorbed by the tissue sample. The force exerted by the ARF on tissue is quantified with equation 2.9:

$$F = \frac{2\alpha I}{c} \qquad \text{(Eq. 2.9)}$$

where α is the absorption coefficient of the tissue, c is the speed of sound, and I is the temporal average intensity at the region of interest. Unfortunately, it is not feasible to quantify the force due to the difficulty in determining the ultrasound intensity at a particular location. The ultrasound intensity is extremely sensitive to location, and even at the focal region, the attenuation through tissue cannot be determined accurately enough to provide elastograms with high sensitivity.

The primary concern with using ARF is the safety, related in particular to the heat and mechanical pressure that are generated. The absorption of ARF induces heat, which can potentially cause damage on the tissue. The thermal index for our purposes has been determined to be 1.7 degrees per volumetric scan. The mechanical index is a measure of the ultrasound exposure, and the federal limit is set at 0.23 for ocular applications and 1.9 for all other applications. The ARF generated by our transducer has a mechanical index of approximately 1.6, which is acceptable for cardiovascular applications.

ARF causes particle displacement due to the transfer of momentum. Tissue displacement or vibrations caused by the ARF can be measured with OCT. Typically, we are aiming to measure micron and nanometer scale displacement using phase-resolved ARF-OCE, which has nanometer phase sensitivity.

2.4 Principles of phase-resolved ARF-OCE

ARF-OCE offers high-resolution elasticity mapping of tissues using dynamic ultrasonic excitation and optical phase detection (65, 66, 74). Several assumptions are made for elastography samples: 1) mechanically homogeneous over a single voxel. 2) isotropic. 3) volume is preserved. ARF is applied onto the sample for excitation while Doppler OCT is used for detection, which makes elastic quantification and mapping possible. The main ideas of ARF-OCE are summarized in Table 2.1. There are 2 main excitation mechanisms, including frequency sweeping and modulation. Frequency sweeps are used for bulk elasticity quantification based on the tissue resonance, which will be discussed in the next section. Modulation mimics an external transient square wave or sine wave force that gets applied to the entire focal region and induces relative vibrational displacement of the tissue. The displacement magnitude is detected by Doppler OCT based on the extracted phase information.

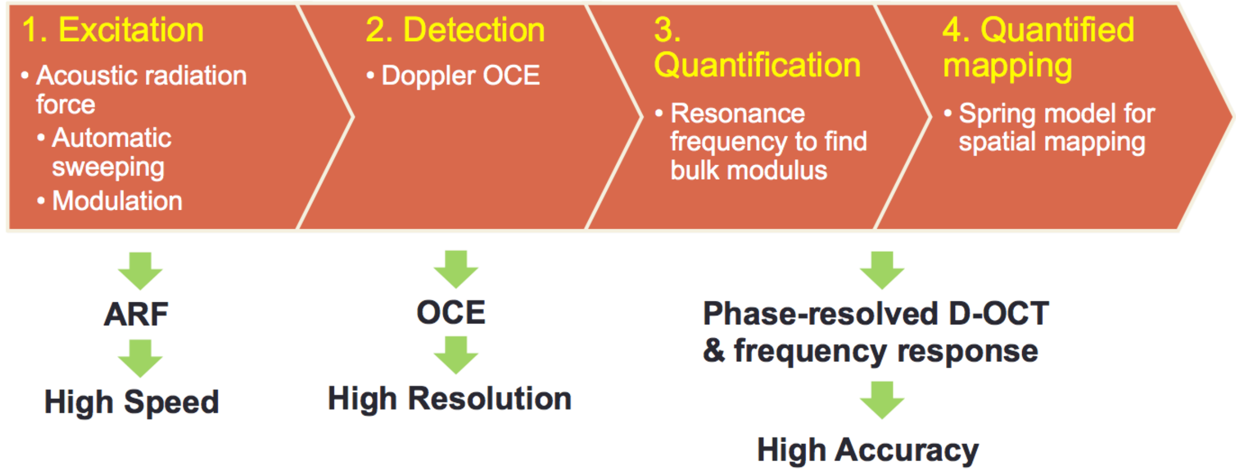

Table 2.1 Diagram of the principles of ARF-OCE.

With the extracted phase information shown previously in equation 2.3, the phase shift between 2 A-lines can be calculated. The Doppler frequency shift, f_D, is by definition directly proportional to the axial velocity denoted by $v_r \cos\theta$ and the measured phase shift, $\Delta\phi(z)$, as shown in equation 2.10:

$$f_D = \frac{2 v_r n \cos\theta}{\lambda_0} = \frac{\Delta\phi(x,z,t)}{2\pi\Delta t} \qquad \text{(Eq. 2.10)}$$

The variable n refers to the refractive index of the sample, λ_0 represents the central wavelength of the light source, and Δt is the period between the A-lines. By rearranging equation 2.6, the Doppler velocity can be defined as a function of the phase shift between A-lines. The displacement of the sample can be obtained by integrating the velocity over time as done in equation 2.11:

$$\Delta d = \int_{t_1}^{t_2} v_r dt = \int_{t_1}^{t_2} \frac{\Delta\phi(x,z,t)\lambda_0}{4\pi n \Delta t \cos\theta} dt \qquad \text{(Eq. 2.11)}$$

In order to calculate the mechanical elasticity, it is necessary to associate the displacement from the Doppler relationship to the elastic modulus. By definition, the strain, ε, is linearly proportional to the displacement, and inversely proportional to the change in sample thickness or the compression in the axial direction, denoted by Δz, as shown in equation 2.12:

$$\varepsilon = \frac{\Delta d}{\Delta z} \qquad \text{(Eq. 2.12)}$$

The Young's modulus, Y, is linearly proportional to the stress, σ, and inversely proportional to the strain. In equation 2.13 below, the stress can be written as the force per area, while the strain is defined as in equation 2.12.

$$Y = \frac{F/_{A}}{\Delta d/_{\Delta z}} = \frac{\sigma}{\varepsilon} \qquad \text{(Eq. 2.13)}$$

A summary of the excitation and detection steps is provided in Table 2.2. After the ARF is applied, OCT data is acquired, from which the phase information is extracted. The displacement is calculated using Doppler OCT and the relative elasticity can be obtained based on the strain value. The stress and the force cannot be measured since it is challenging to determine the ARF as discussed previously.

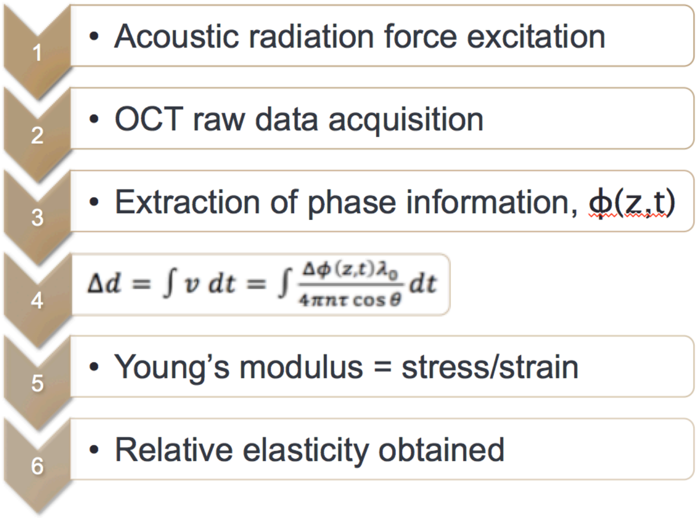

1. • Acoustic radiation force excitation
2. • OCT raw data acquisition
3. • Extraction of phase information, $\phi(z,t)$
4. $\Delta d = \int v\, dt = \int \frac{\Delta\phi(z,t)\lambda_0}{4\pi n\tau\cos\theta} dt$
5. • Young's modulus = stress/strain
6. • Relative elasticity obtained

Table 2.2 Summary of excitation and detection of ARF-OCE

In compressional OCE, an elastogram is generated based on the inverse relationship between the displacement and the Young's modulus. For commonly used excitation methods such as air puff, it is difficult to quantify the force applied per area. Although we can calculate ARF in a well-defined geometry, it is difficulty to get the precise value of ARF for in vivo applications when the distance between the transducer and tissue changes. In other words, the stress cannot be quantified, so a qualitative map is produced. For qualitative imaging purposes, the elasticity of healthy tissue and pathological ones can be differentiated by the differences in displacement values, with a higher displacement corresponding to softer tissue. Since the difference in elasticity are expected to differ by at least one order of magnitude for healthy and pathological ocular tissue and similarly for healthy intravascular tissue and plaque, qualitative information can be helpful in disease diagnosis.

The compressional OCE method allows users to approximate the ratio between sample compositions, but it is unable to directly offer quantitative elasticity. This is problematic when comparisons and diagnoses much be made between two different images, or between different time points. Due to changes in the experimental conditions and noise within the system, the displacement map cannot be effectively used to make conclusions between different samples and at difference acquisition times. Because the ARF on the sample cannot be accurately measured for in vivo applications, the absolute Young's modulus cannot be extracted. This leads to our methods of quantification, which will be discussed in the next section.

2.5 Quantification of elasticity

The relative elasticity measurements provided by the above method is helpful in distinguishing diseased lesions from healthy tissue within a single data set at one time. However, due to the different imaging conditions and external influences, it is difficult to make comparisons between different samples or at various time points. For example, the focal region of the transducer can shift at the sub-millimeter level, altering the ultrasonic force, thus affecting the phase response of the tissue, which can be incorrectly interpreted as a change in stiffness. Since the displacement sensitivity is in the nanometer scale, the measured tissue response can vary by magnitudes.

To determine the absolute stiffness of the tissues, we have developed a resonance ARF-OCE method. To start, the system can be represented by a simplified mechanical model consisting of a single spring and damper, also known as the Voigt Body Model, which is written as the following differential equation (53):

$$F(t) = m\ddot{x}(t) + \gamma \dot{x}(t) + kx(t) \qquad \text{(Eq. 2.14)}$$

The sinusoidal force applied to the sample is denoted by $F(t)$, while m is the mass of the object, $x(t)$ is the displacement, γ is the viscosity coefficient, and k is the spring constant. After solving for the displacement in the nonhomogeneous differential equation, and applying Hooke's law to the expression for Young's modulus, the elasticity can be represented by equation 2.15:

$$E = \frac{kL}{S} = \frac{(\mu^2+\lambda^2)mL}{S} \qquad \text{(Eq. 2.15)}$$

The thickness of the sample is denoted by L and the contact area is by S. The oscillation frequency and the damping coefficient are represented by $\mu = \frac{\sqrt{4mk-\gamma^2}}{2m}$ and $\lambda = \frac{-\gamma}{2m}$, respectively. Based on equation 2.15, the Young's modulus is proportional to the square of the oscillation frequency and the damping coefficient, while the mass, thickness, and area of the sample is known and remains relatively constant. The viscosity coefficient of a viscoelastic sample is often insignificant compared to the excitation force of ARF-OCE (53, 75). Therefore, the Young's modulus is primarily dependent on the oscillation frequency or the resonance frequency. Based on the principles of physics, the response of the sample will be highest when it is vibrating at its natural resonance frequency. This means that the tissue response will peak to signify the resonance frequency, and the absolute Young's modulus can be calculated.

The resonant frequency peak, μ, in equation 2.15 is determined by doing M-mode imaging while modulating at different frequencies, and measuring the displacement level. The frequency at which the highest displacement occurs is the resonant frequency. A frequency sweep from 1 Hz to 100 Hz has been determined to be within the range for tissue resonance. To demonstrate the dependency of the elasticity on the resonance frequency, it is necessary to sweep across the excitation frequencies to determine the resonance peak of a material with a known stiffness. This has been done in phantoms with relatively consistent mass and geometry but differing stiffness, and the squared relationship was verified (74). After the resonance frequency has been measured, calibration must be performed with samples with known elasticities to determine an accurate relationship between the resonance frequency and Young's modulus by fitting the data to equation 2.15.

The resonance frequency of tissue layers is difficult to isolate, so it is best to measure the bulk Young's modulus of the entire depth of the sample. Since the frequency sweep can only quantify the Young's modulus of the whole depth of the sample at the region of excitation, we need an additional model to calculate the individual layer elasticity.

In equation 2.15, we assume that the layers of the retina within the region of excitation can be modeled as a series of springs, each with their own spring constant, k_n, thickness, L_n, and surface area, S_n, with a fixed boundary at the bottom, similar to the simplified diagram shown below in Figure 2.7.

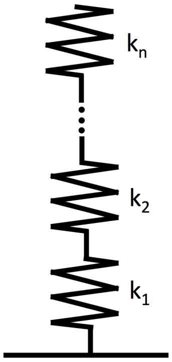

Figure 2.7 Simplified model of tissue layers based on springs in series.

From the model in equation 2.14 based on the stress over strain relationship, we know $E = \frac{kL}{S}$, where E is the Young's modulus, k is the spring constant, L is the thickness, and S is the surface area of the region of interest. Rewriting this equation, we get:

$$k = \frac{ES}{L} \tag{Eq. 2.16}$$

We also know that for springs in series, the bulk spring constant is related by:

$$\frac{1}{k} = \frac{1}{k_1} + \frac{1}{k_2} + \cdots + \frac{1}{k_n} \tag{Eq. 2.17}$$

Substituting in equation 2.16 into equation 2.17, we get:

$$\frac{L}{ES} = \frac{L_1}{E_1 S_1} + \frac{L_2}{E_2 S_2} + \cdots + \frac{L_n}{E_n S_n} \tag{Eq. 2.18}$$

The terms without subscripts on the left side of the equation are the bulk values of all n layers, while the others on the right side are the individual values for each of the layers. The surface area of each of the layers can be assumed to be the same, since the same excitation beam is used to excite the same lateral region of interest for each layer. This means that all the S terms cancel out and equation 2.18 can be rewritten as:

$$\frac{E}{L} = \frac{1}{{L_1}/{E_1} + {L_2}/{E_2} + \cdots + {L_n}/{E_n}} \text{ or } E = \frac{L}{\sum_{i=1}^{n} {L_i}/{E_i}} \qquad \text{(Eq. 2.19)}$$

In summary, the E is quantified based on the frequency sweep mechanism in equation 2.15. The relative ratio of the E_i for each individual layer can be determined using the modulated excitation approach. Finally, with the relative ratio between the layers and the quantified bulk Young's modulus, as well as the layered and bulk thicknesses, the absolute Young's modulus can be determined for each layer using equation 2.19. Last, the spatial distribution of the elastic moduli can be quantitatively mapped out using the relative vibrational displacement response that is measured using ARF-OCE with the mean value based on the individual layer elasticity. To verify the same principle for vascular and ocular tissues, these experiments have been performed on the retina and on human cadaver coronary arteries. The mechanical quantification can help determine pathological tissues and aid in the diagnosis of diseases.

2.6 Summary

In summary, we have discussed the basic principles of ARF-OCE and the elasticity imaging approach from optics to acoustics. First the basics of OCT are introduced, identifying both the TD-OCT and FD-OCT methods. Then we present the ideas of SD-OCT in detail and discuss the challenges in the alignment and calibration of the system. Next an overview of the ARF generation is given based on the principles of ultrasound, and the combined ARF-OCE system is presented. Finally, the method of elasticity quantification of the system is discussed, including the Voigt and spring models.

CHAPTER 3

Corneal Acoustic Radiation Force Optical Coherence Elastography

This chapter presents the preliminary ocular imaging results using ARF-OCE on *ex-vivo* rabbit corneas. An introduction to corneal diseases and current diagnosis methods will be summarized in section 3.1. Our ARF-OCE system setup will be introduced in section 3.2 while phantom validations to verify axial and lateral mechanical contrast are discussed in section 3.3. Healthy corneal imaging and the effects of the crosslinking experiments are presented in section 3.4, including instantaneous crosslinking and time delayed crosslinking. Finally, the results are summarized with a conclusion in section 3.5.

3.1 Introduction

The cornea is primarily composed of cross-linked collagen fibers, which provides it with high tensile strength and serves as a protective coat to the eye (76). It is an essential portion in the refraction of light entering the eye, and when there is a disruption in the collagen fiber network, such as in the case of keratoconus, corneal refractive function is compromised, affecting vision (77). Keratoconus is a disease characterized by changes in the cross-linking properties, high corneal curvature, reduced corneal thickness, and tissue topographic irregularity (78). In addition to natural diseases, refractive surgeries such as LASIK alter biomechanical properties of the cornea, resulting in conditions such as progressive post-LASIK keratectasia (PPLK) (79). PPLK is a progressive deformation of the cornea that occurs within two years of surgery, causing disruptions in the collagen cross-linking network (79, 80). In both PPLK and keratoconus, a common management solution is corneal collagen crosslinking treatment, which allows for biomechanical stability of the cornea by increasing the intra- and interfibrillar rigidity (80). With the increasing popularity of refractive surgeries, as well as the natural occurrences of corneal diseases, there is an increasing need for understanding the biomechanical properties of ocular tissue for diagnosis and progression tracking.

The ocular response analyzer (ORA) has been used to measure the mechanical properties of the cornea. It analyzes the response of ocular tissue to an air pressure, focusing on the hysteresis of the relaxation (81). However, factors such as the corneal thickness and curvature are not accounted for in ORA. The Corvis tonometer is another technology that visualizes and measures the deformation of the cornea in response to an air impulse (82). However, the response measurements are taken for the entire cornea as a whole, and cannot focus on a small region of interest. This is problematic in diagnosing ocular diseases in their early stages.

Recently, ultrafast OCE methods have been used to obtain both 2D and 3D volumetric data quickly, and are rapidly progressing toward translational research (83, 84). These methods use air puff or compression techniques for tissue excitation. In the case of the air puff technique in ocular OCE, full quantification of a depth resolved corneal image requires measurement and modeling of the shear wave across the entire cornea, which may have limitations when working with diseased corneas where lateral changes play an important role. Compression OCE is highly contact-based and not ideal for translation and *in vivo* studies. OCE has also been performed on corneal tissue by analyzing the propagation of shear waves (55, 85, 86). However, these corneal imaging methods do not currently offer real-time imaging of the elasticity map.

We propose using ARF-OCE with dynamic excitation to obtain high-speed, high-resolution elastogram mapping of corneal tissues. We apply a modulated square wave acoustic force to the sample and detect the phase shifts of the sample oscillation using phase-resolved OCT. In this chapter, we validate the ARF-

OCE system detection of axial and lateral changes in mechanical stiffness. We also use the imaging system for healthy corneal tissue as well as tissue with induced corneal sclerosis to compare the resulting Young's modulus.

3.2 System setup

The OCE system uses an ultrasonic transducer system for excitation of the sample, phase-resolved OCT system for detection of the vibrational response, and a computer for image processing. The schematic diagram is shown in Figure 3.1. The axial resolution of the system is 2.5 μm while the lateral resolution is 15 μm. A function generator feeds a square wave modulated signal into an amplifier, which generates an acoustic radiation force via a focused ring transducer of 4.5 MHz. The ultrasound transducer has a uniform stress field within approximately a 400 um by 400 um lateral region, with a larger axial field of 5 mm. The optical system is based on a superluminescent diode source with a central wavelength of 890 nm, and a bandwidth of 150 nm. The light traveling to the sample and reference arms splits in an 80/20 coupler. The light from the reference is delayed and reflected back with a mirror. The light in the sample

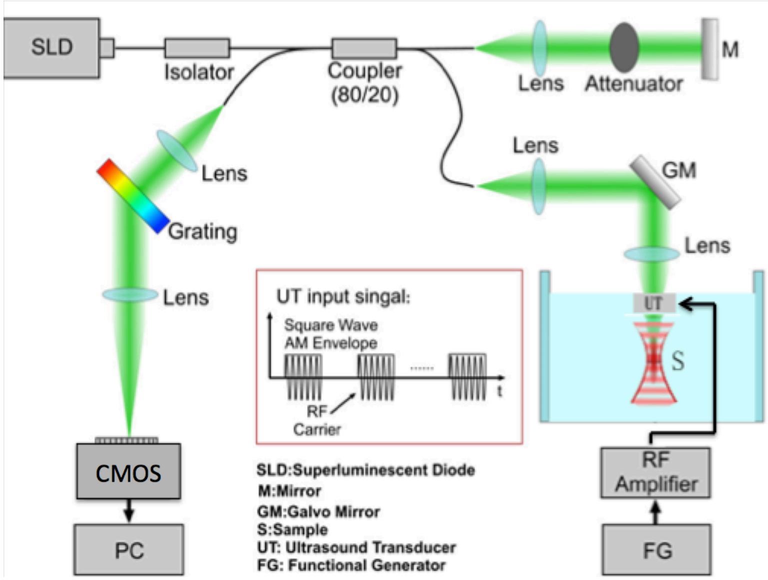

Figure 3.1 Schematic diagram of Corneal OCE system.

arm goes through the hollow ring in the middle of the transducer and interacts with the phantom or tissue in the focal zone, which overlaps with the acoustic zone of the transducer to generate a strong phase signal. The power from the sample arm is measured to be 0.89 mW, which is below the safe value determined by the American National Standards Institute.

The light then travels back into the camera arm, which houses a collimator, a diffraction grating, a focusing lens, and a CMOS camera for detection of the interference signal. A line scan CMOS detector, which can operate at up to 70k A-lines per second, is used in place of the CCD camera in the previous manuscripts for faster imaging. However, in these *ex-vivo* experiments, an A-line rate of 20kHz is used to capture OCT images and the OCE oscillations.

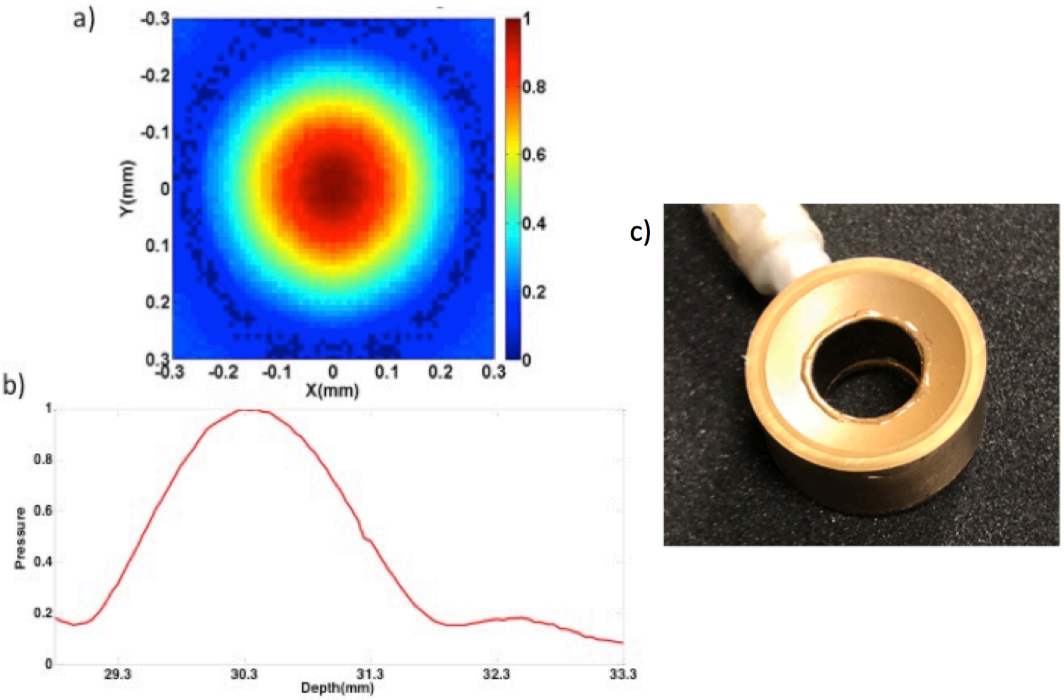

Figure 3.2 Ring Transducer Beam Profile. a. Normalized pressure profile at the axial focus. b. Normalized axial beam profile.

The acoustic profiles of the ultrasonic excitation transducer and OCT scanning beam were arranged in a confocal configuration on the same side of the imaging sample under the guidance of a hydrophone. The normalized pressure profile of the transducer is shown in Figure 3.2. The region of uniform pressure is small in the lateral direction at the axial focus as shown in Figure 3.2a and the axial beam profile is shown in 3.2b. During imaging, the ring transducer, shown in Figure 3.2c, was pulled away from the focal region in the axial direction in order to achieve a uniform stress region of approximately 600 um. Last, Doppler methods are used to determine the phase shifts between A-lines, where a larger phase change corresponds to high displacement and a softer sample. There is high phase stability of a few milliradians for a spectral domain OCT system (65).

3.3 Phantom validations

Our group had previously verified the lateral contrast of ARF-OCE imaging using a two-sided phantom (65, 66, 74), but it is still necessary to show feasibility for axial contrast. An agarose tissue-mimicking phantom with a stiffer inclusion was fabricated. The stiff inclusion has a diameter of about 1 mm, consisting of 0.8% agarose (by weight). It is buried within the larger phantom of 0.3% agarose. The completed sample, which is round with a diameter of 3.5 cm and a thickness of 1 cm, was placed on a holder for OCE imaging.

To determine the feasibility of this agarose phantom, we calculated the displacements of two uniform samples under different excitation voltages shown in Figure 3.3a. A linear dependency of the ultrasound-induced displacement on the excitation voltage was found, and a 500 mVpp excitation voltage was used for the rest of this study.

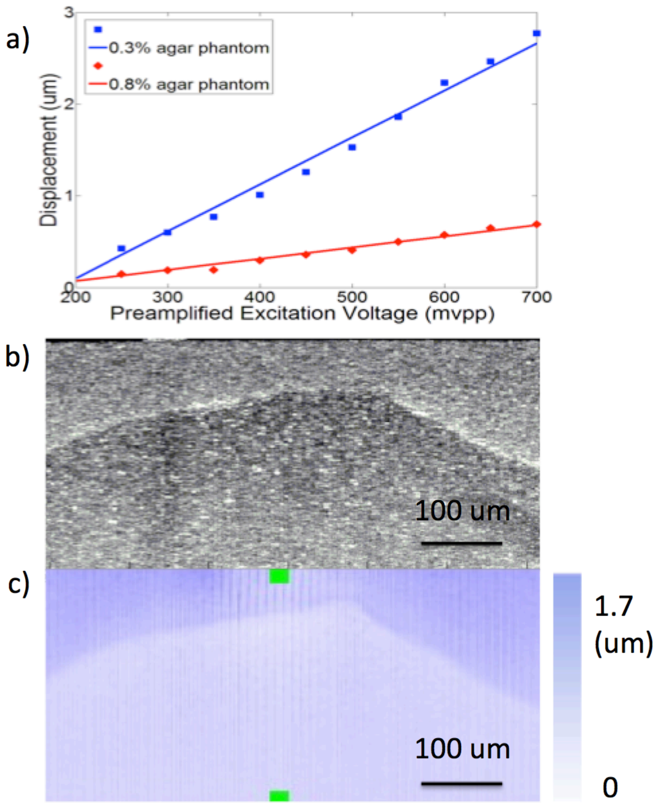

Figure 3.3 Phantom testing. a. Displacement under different excitation voltages for two phantoms of different stiffness. b. OCT image of inclusion phantom. c. OCE projection image of inclusion phantom.

The OCT and OCE displacement images of the inclusion phantom are shown in Figures 3.3b and 3.3c, respectively. The boundary between the two phantoms is evident in the OCT image likely because of water at the interface when the phantom was made, which contributes to a high scattering signal. In the OCE image, the boundary of the two phantoms is evident because of the differences in vibrational response. The shape of the two phantoms is clearly distinguishable from the OCE image in all directions, which proves that our system is able to detect differences in the mechanical properties of tissue both laterally and axially.

Using the phase change and the Doppler relationship, it is possible to extract the velocity of the phantom oscillation. The displacement can be calculated using the velocity measurements and integrating over time, depicted in equation 2.7. In this case, the central wavelength is 890 nm, the refractive index, of tissue is 1.3, the exposure time is 50 us, and the Doppler angle is 90 degrees. The mean displacement ratio of the softer phantom to the stiffer inclusion is approximately 3.49 : 1 according to the experimental results in figure 3. The Young's Modulus of a material is defined in equation 2.8. In this way, the stiffness of a sample varies inversely with its induced displacement values, and relative stiffness can be obtained if the displacement is calculated. The relative stiffness of the surrounding phantom to the rod inclusion of the agarose phantom is 1: 3.49.

Compression tests were performed using MTS Synergie 100 on both the 0.3% and a 0.8% agarose phantom, with resulting Young's Moduli of 3.68 kPa and 12.24 kPa, respectively. This corresponds to a stiffness ratio of 1: 3.33, which is in close agreement with our experimental result of 1: 3.49. A strain of up to 0.1 mm/mm with a strain rate of 50 mm/min was used for testing. The feasibility of the ARF-OCE system to detect relative axial and lateral contrast in mechanical properties is shown.

3.4 Corneal crosslinking imaging results

To test the feasibility of our imaging system on corneal tissues, we collected fresh rabbit eyeballs and obtained 3-D images of the rabbit cornea. All experiments were performed within 24 hours of eyeball extraction to ensure freshness. First, the healthy eyeball was placed inside a holder and covered with optically clear gel to hold the sample in place during excitation. A 3 mm by 3 mm area was scanned in the center of the cornea by using OCT, as shown in the 3-D reconstruction in Figure 3.4a. OCE imaging was performed within a smaller area with a 400 Hz ARF modulation frequency. The 3-D OCE images were reconstructed and shown in Figure 3.4b, with the color representing the phase shift of the tissue with respect to adjacent A-lines.

We also aimed to change the stiffness of the corneal tissue by inducing cross-linking using formalin solution. The entire eyeball was removed from the system and soaked with droplets of 10% formalin solution. After soaking for 12 hours, we placed the sample back into the system to observe the changes. We assume that after 12 hours, the formalin-induced crosslinking is uniform in the entire cornea, and 3D OCE was performed on a small region using the same ultrasonic excitation conditions. The results are shown in Figure 3.4c, where it was apparent that the phase shift has decreased drastically. The displacement amplitude ratio of the healthy cornea to the formalin soaked one was calculated to be 6.34 ± 0.22: 1.

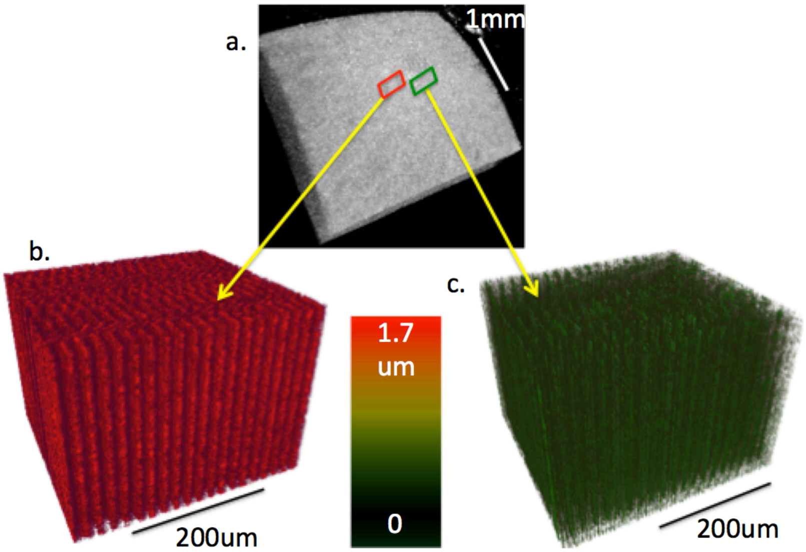

Figure 3.4 3-D images of rabbit cornea with and without formalin crosslinking. a. 3-D OCT reconstruction of 3 mm by 3 mm section of cornea. b. 3-D OCE section of healthy cornea. c. 3-D OCE section of cross-linked cornea.

Since the cornea was soaked for 12 hours, it was speculated that the mechanical changes could have been influenced by other factors, such as changes in the freshness of the cornea or instabilities of the system with change in time. In addition, the difference in stiffness changed over 6 fold in this case, which makes it easy to detect.

In order to induce a stiffness change within a single cornea to eliminate other factors affecting the system and simultaneously image tissue of different stiffness, we injected 0.01 ml of 10% formalin inside the healthy cornea via a 1-cc disposable syringe with a 30-gauge needle. The cornea was allowed to sit for merely ten minutes while we prepared for the imaging and zoomed into the area of injection. As shown in Figure 3.5a, the OCT image reveals that the left side, where the formalin solution was injected, is distinctly thicker than the right due to the formalin bubble. The tissue was excited with a 400 Hz modulation frequency and a 500 mVpp pre-amplified voltage given to the transducer. The OCE displacement magnitude image is shown in Figure 3.5b, with a red color representing high displacement. A much smaller displacement shift is shown on the left side, where the injection took place. Both OCT and OCE images were averaged over 50 B-scans for better representation. The displacement shifts of the raw OCE images before magnitude extraction are shown in Figure 3.5c, which corresponds to a smaller displacement on the left side that vibrates much less than the right. The displacement ratio of the healthy side on the right to the cross-linked portion on the left is approximately 1.82 ± 0.04: 1. There is a gradient in the middle portion of the image, similar to that of the phantom studies in Figure 3.3. Over time, the formalin solution would diffuse across the entire cornea and the OCE image would resemble that in Figure 3.4c. It was noticed that the displacement ratio of 1.82 ± 0.04 was much smaller. It is likely because we did not soak the cornea for nearly as long, so less cross-linking took place within the tissue. It is also important to note that the displacement values begin to decrease on the right side of the image, which is where the uniform acoustic focal zone ends at approximately 600 um.

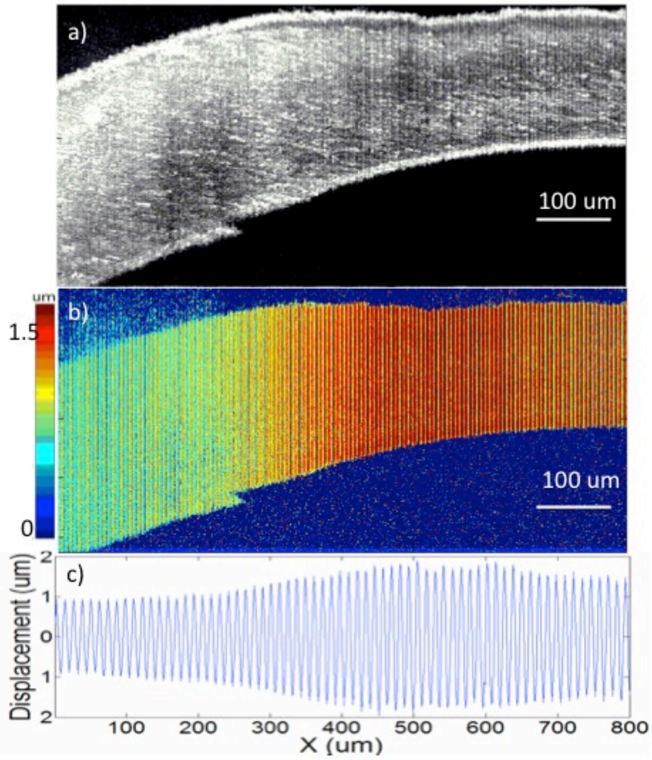

Figure 3.5 Imaging of rabbit cornea with injection of formalin solution. a. OCT image of cornea. b. OCE displacement magnitude image of cornea. c. Quantified displacement of cornea.

3.5 Summary

We have demonstrated the feasibility of using an ARF-OCE system for assessing the mechanical properties of corneal tissue. The feasibility of the imaging system to detect mechanical contrast both laterally and axially was tested on an inclusion dual-layered agarose phantom with a difference in stiffness in the two layers of 3.33 fold. The experimental Young's moduli ratios corresponded well with the mechanical compression test results under acoustic radiation forces. We have performed *in vitro* imaging of a healthy rabbit cornea as well as a cross-linked one. The OCT image changed little, but the OCE showed a 6-fold change. Last, we induced tissue cross-linking on a small area within the same cornea, and observed an approximately 2-fold difference in the stiffness. These results show that our ARF-OCE method has great potential in distinguishing diseased corneal tissue from normal ones and quantitatively characterizing the severity of the change in mechanical properties. These results validate the feasibility of using this system for relative mechanical elasticity testing and show its capabilities in demonstrating corneal cross-linking. This technique has great promise for the characterization and diagnosis of corneal diseases.

CHAPTER 4

Quantitative Ocular Imaging Using Resonance Response

In this chapter, we discuss the diseases of the anterior and the posterior eye and how to use the resonance frequency method to quantify the elasticity change based on shifts in the intraocular pressure. In section 4.1, I introduce the mechanical changes associated with ocular diseases and the current methods of diagnosis. The novel frequency sweep system is presented in section 4.2, and phantom calibration is explained in section 4.3. Next, the elasticity of an ex vivo pig eye and an in situ rabbit eye were quantified in sections 4.4 and 4.5, respectively. Last, I present the feasibility of using this technology to measure ocular elasticity based on different intraocular pressures in section 4.6 and a summary is presented in section 4.7.

4.1 Introduction

The eye can be separated into the anterior segment, which is responsible for focusing incoming light, and the posterior segment, which is responsible for detecting and transmitting the visual information to the brain. The two portions are both critical to the ocular health and must work together to create vision. Over the past 20 years, ocular diseases, including a combination of anterior and posterior diseases, have steadily increased with the aging and growing population. Keratoconus, as mentioned in the previous chapter, is characterized by the thinning and protrusion of the cornea and can lead to uncorrectable vision blurring and distortion (87, 88). It is the leading form of corneal dystrophy in the United States and affects 1 in 2000 people. Age related macular degeneration (AMD) is a disease of posterior eye that includes the formation of drusen and neovascularization of the retina, which leads to blurring and central vision impairment. AMD is the leading cause of blindness in Americans over 50 years of age (2, 89).

Keratoconus can be treated using tissue cross-linking methods, but still may progress to the point that corneal transplant surgery is required to salvage vision. There is currently no cure for AMD, but drug treatment is often used to slow down the disease progression. In both cases, early diagnosis is necessary in order to prescribe the correct form of treatment. AMD is currently diagnosed by imaging with angiography or optical coherence tomography to visualize the blood flow and the structural depth of the retina, respectively (90). Keratoconus is most often diagnosed with keratometry and corneal photography (91). In most cases, these diagnostic measures can only capture the disease in its advanced form.

AMD and keratoconus are different in nature and treatment, but they are similar in that they both affect the elasticity of tissues. In AMD, a stiffness change may take place at the early onset of drusen formation (92), before they can be visualized with structural imaging. In keratoconus, the corneal cross-linking is disrupted at the onset of disease (93), leading to changes in elasticity. It is essential to have a single technology to monitor the elasticity of the entire eye globe in order to diagnose these diseases in their early stages.

The mechanical properties of the cornea have been quantified using ocular methods (85, 86, 94), but the retina is hidden deep inside the globe, and is not as readily accessible. Some excitation methods, such as the air puff, will only detect surface response, so is not ideal for depth imaging. Ultrasound can penetrate through the entire eye, but using shear wave methods, it is difficult to detect small differences in velocity across thin tissues. Relative ARF-OCE has been used to quantify the cornea in the previous chapter, and can detect subtle changes in axial and lateral elasticity, but it is difficult to quantify and correlate to Young's moduli. It has been shown that the resonance frequencies of compressional waves are correlated to its elasticity, as demonstrated using magnetic resonance elastography and optical coherence elastography (52, 53, 74). In addition to tissue properties, it has been determined that the intraocular pressure of the eye has a profound impact on its measured elasticity, which is one of the factors limiting the accuracy of *ex-vivo* ocular elastography (95, 96).

We report on an automatic frequency sweeping mechanism to detect the resonance frequencies of the entire globe in order to quantify the elasticity of the tissues. A modulated acoustic radiation force, which sweeps across 250 frequencies for excitation, is synchronized with OCE, which is implemented for the detection of tissue response. First, phantom characterization was performed using 5 different elasticity silicone phantoms. The data were used for calibration of the relationship between the resonance frequency and the Young's modulus. Next, m-mode frequency response was detected for both the cornea and retina in an excised pig eye. Last, the frequency response of the in-situ eye was detected for a deceased rabbit within 30 minutes of euthanization. The effects of the intraocular pressure on the measured stiffness of the cornea were studied and a linear relationship was observed.

4.2 Frequency sweep system setup

In previous ARF-OCE experiments (67, 74), a focused ultrasound transducer was used for excitation, and a uniform signal region of 0.5 mm in diameter was generated. It was difficult to image the entire tissue region due to the large acquisition time and the difficulty of image reconstruction of each individual group of scans. The setup was not ideal for *in vivo* imaging, which is the goal. It was also challenging to obtain resonance frequency measurements since only a small portion of the tissue was excited and bulk response was not possible. In addition, transmission mode OCE, where the excitation and detection are on opposite sides of the sample, is not feasible for most tissue applications. In this manuscript, we utilized an unfocused 1 MHz ultrasound transducer with a diameter of 12 mm. The transducer can capture the depth of the entire eyeball and elicit a frequency response. Both excitation and detection occur on the outer surface of the eye. As shown in Figure 4.1a, the transducer was placed confocal to the Doppler OCT beam, at an angle. Doppler OCT detects the tissue response in the axial component.

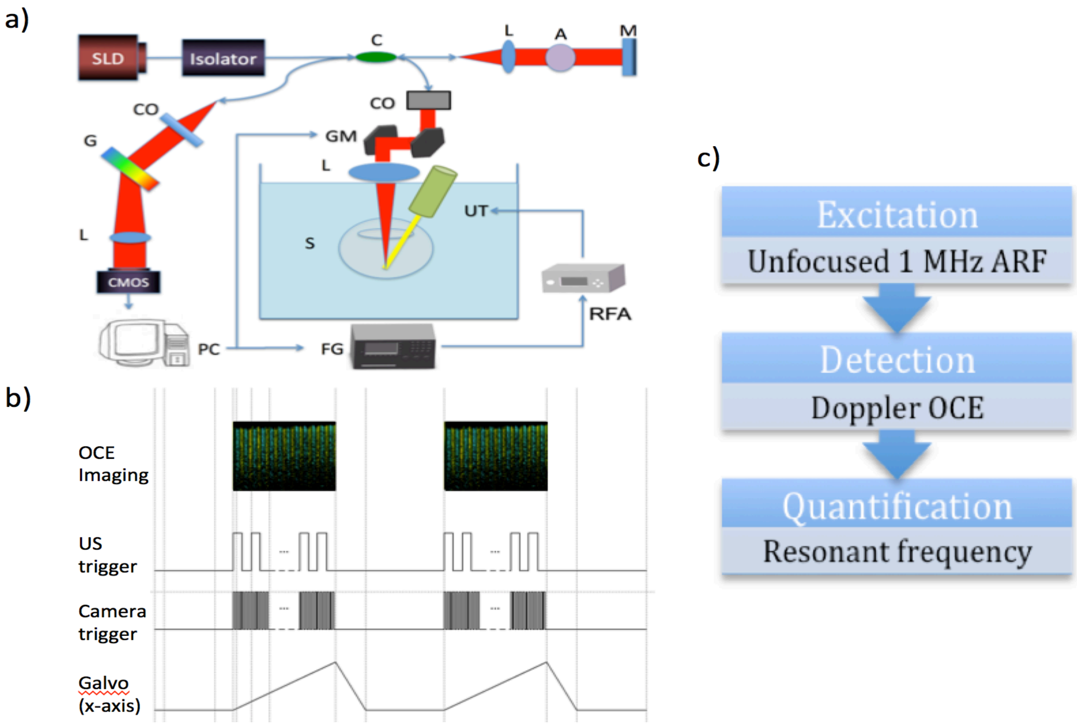

Figure 4.1. System schematic diagram. a) ARF-OCE system setup. L: lens, G: grating, CO: collimator, SLD: superluminescent diode, C: coupler, A: attenuator, M: mirror, GM: galvanometer mirrors, UT: ultrasound transducer, S: sample, RFA: radiofrequency amplifier, FG: function generator. b) Timing diagram of automatic synchronization. c) Flow chart of elastography.

Optical detection is performed using an 890 nm broadband superluminescent diode source with a bandwidth of 150 nm. An 80/20 coupler was used to split the light into the reference and sample arms, while the interference spectrum is separated with a diffraction grating and detected by the CMOS camera. For this study, the A-line rate was kept at 20 kHz, and m-mode images were obtained at each modulation frequency. The galvanometer mirrors were used for positioning of the light onto the region of interest. With a 0.9 mW output power on the sample, the system operates below the preset MPE limits.

In previous studies, including the one presented in chapter 3, only the relative elasticity values could be measured, so the alignment between the transducer, detector, and sample was highly sensitive in governing the relative amplitudes. In essence, all imaging conditions must be kept consistent in order to make accurate comparisons between different samples. External and environmental factors make this nearly impossible. In addition, since modulation frequencies far away from the resonance frequencies must be used, the excitation power needed to be high in order to observe a signal. In this study, a frequency sweep excitation is used, and the resonance frequency of each sample is determined. In this way, the imaging conditions, such as alignment, do not affect the frequency response, so human error is reduced. The excitation power can also be decreased since the response peaks at the resonance level.

The synchronization of the ultrasound excitation and optical detection is illustrated in Figure 4.1b. The sweeping mechanism has been automated, such that for every modulation frequency, 1000 m-mode A-lines are obtained at the region of interest. Two sets of data are taken at each frequency from 1 Hz to 250 Hz. Most human tissues have resonance frequencies of less than 100 Hz, so this range adequately captured the resonance peak.

4.3 Phantom calibration

Silicone phantoms were fabricated using titanium oxide as the optical scattering agent and for acoustic attenuation. A total of 0.258 g of TiO_2 was used per 300 g of mixture, which was kept consistent to preserve the same imaging contrast throughout all the phantoms. The amount of curing agent was varied to reflect the different elasticity of the phantoms, and measured at 1.7%, 2.3%, 3.3%, 8%, and 10%. First, the curing agent and TiO_2 were mixed in an ultrasonic vibrator for 90 minutes. Next, the mixture was added to silicone gel, with a total mass of 300 g. The solution was stirred by hand for 30 minutes until well mixed, and then placed in a vacuum for 30 minutes until all bubbles dispersed. The gel as then poured into 5 cm diameter dishes, with a depth of 1 cm. The phantoms were allowed to sit and dry overnight, and experiments were performed afterwards.

The raw phase frequency response data for 3 different phantoms are shown in Figure 4.2a. Data points after 100 Hz were omitted due to insignificant results. The small interval displacement response curves were then calculated, with the results averaged and normalized as shown in Figure 4.2b. The peaks for the five silicone phantoms can be clearly differentiated.

Mechanical compression tests were performed on the 5 uniform silicone phantoms using MTS Synergie 100. A strain of up to 0.1 mm/mm was used, with a strain rate of 50 mm/min. The thickness of the tissue was approximately 1 cm, and 50% compression was used. Mechanical testing was performed immediately after imaging to minimize the error. The resonance frequency peak and the Young’s modulus are related, and the relationship was given in equation 2.10 and 2.11.

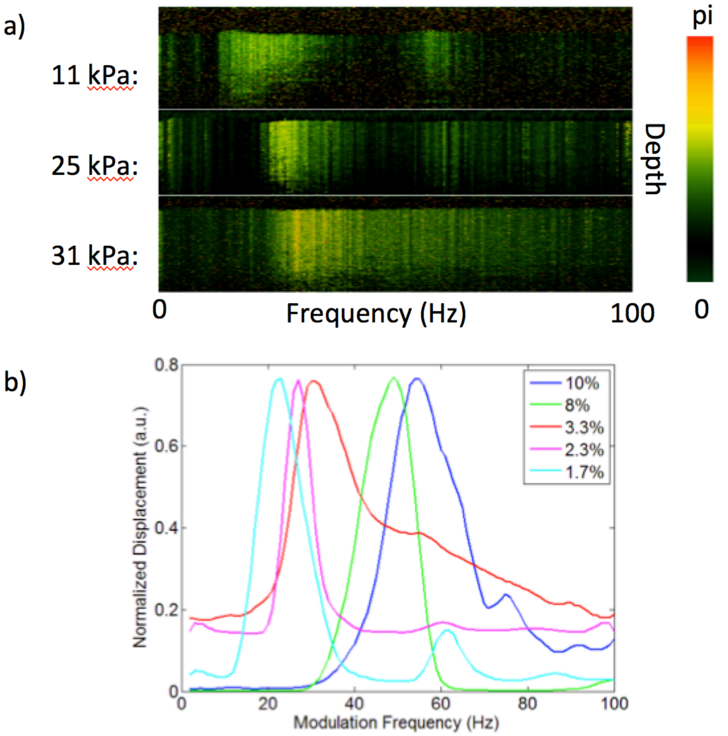

Figure 4.2 Phantom characterization. a) Raw phase frequency response. b) Quantified resonance frequency after normalization.

From equation 2.11, it can be concluded that the resonance frequency squared is proportional to the Young’s modulus. The elasticity of the silicone phantoms were plotted against the resonance frequency squared, as shown in Figure 4.3. A linear relationship was observed and the linear regression line has been fitted. There was a high correlation and a R^2 value of 0.998 between the modeled relationships. The two variables are related by the relationship $Y = 0.03\ f^2 + 0.3$.

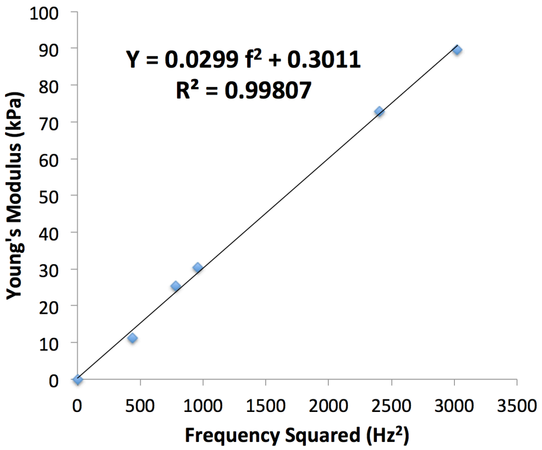

Figure 4.3 Linear relationship between the Young's modulus and the resonance frequency squared, with a best fit plot.

4.4 Porcine *ex vivo* whole eye imaging

In order to more closely simulate human tissue, pig ocular tissue was used. Pig eyes obtained within 2 hours of death were immersed in PBS solution for preservation. All experiments were performed within 24 hours of extraction. The entire eyeball was molded in an optically and acoustically clear agar phantom and fixed to the imaging stage. The top portion of the eye is not covered by the agar in order to minimize the attenuation of ultrasound signal by the phantom. The entire sample was submerged in PBS during imaging in order to keep the eye hydrated and also provide a medium for the ultrasound propagation. After cornea imaging was completed, the anterior portion of the eye was removed by carefully puncturing the iris and cutting away the cornea. The lens was taken out, but the vitreous was left in place to avoid damage to the retina.

M-mode frequency sweep imaging was performed on both the retina and the cornea. The central portion of the cornea was first swept from 1 to 250 Hz, with two frames per frequency and 1000 A-lines per frame. Next, the anterior portion of the eye, including the cornea and the lens, were carefully removed so that only the posterior portion remains. The retina was submerged in PBS as the coupling medium. The optical and acoustic signals were focused on the central portion of the retina, and the same set of frequency sweep was performed. The raw phase data over frequency is shown in Figures 4.4a and 4.4b, while the displacement response is plotted in Figure 4.4c. It is apparent that the resonance frequency peak for the cornea at 82 Hz is significantly higher than that for the retina at 21Hz. Assuming that the viscosity of ocular tissue is similar to that of the tissue-mimicking phantoms, and that the excitation depth and area is unchanged, the elasticity can be quantified based on the phantom calibration in Figure 4.3. The Young's modulus for the retina is approximately 13 kPa, and for the cornea is approximately 206 kPa. These estimations refer to the bulk modulus of the entire tissue, and the peaks signify the resonance frequency of the portion in focus.

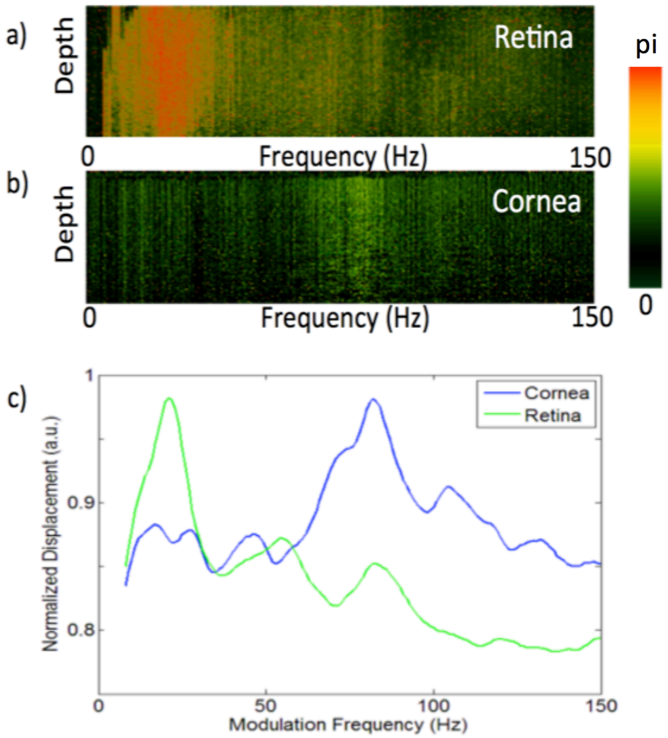

Figure 4.4 Pig eye results. a) Phase response of the pig retina over 150 Hz. b) Phase response of the pig cornea over 150 Hz. c) Normalized displacement response.

4.5 Rabbit *in situ* whole eye imaging

Although the elasticity of the rabbit retina and cornea have been quantified, the effect of the lens and cornea on the retina measurements is unknown. In order to perform *in vivo* quantification, it is necessary to determine the relationship between the bulk measurements and the individual tissue in focus. Therefore, measurements of an intact rabbit eyeball were taken. The rabbit was obtained within 20 minutes of euthanization from another experiment, with no prior ocular damage. All experiments were performed within 1 hour from death. The rabbit eye was proptosed using cotton swabs and kept moist with PBS. An aperture with a diameter of 5 mm was made in a sheet of latex, which was supported using a ring stand. The hole in the latex was placed directly on the proptosed rabbit eye and PBS was added to the set up to serve as the ultrasound medium as well as keep the tissues hydrated. Since the eye was fresh, frequency data was obtained for both the anterior and posterior eye with the tissue intact, representing the frequency response of the entire eyeball.

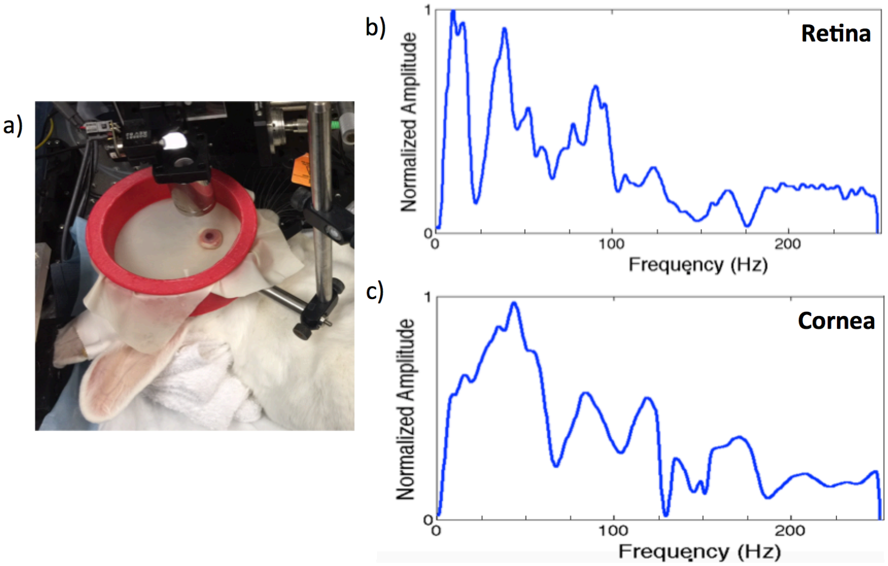

Figure 4.5 Rabbit eye results. a) Set up of deceased rabbit on imaging stage. b) Retina displacement response. c) Cornea displacement response.

The cornea and lens were fresh and optically transparent. Instead of removing the eye from the rabbit, the eye was proptosed in a PBS bath, through a small aperture in a rubber sheet, as shown in Figure 4.5a. The system was first aligned to focus on the central retina, and a set of frequency sweep measurements from 1 to 250 Hz were taken. Next, the focus was moved upwards to the central cornea, and the same measurements were obtained. By the time all data were taken, the eyeball was still optically transparent, which meant that minimal degradation was observed.

The displacement data were analyzed and plotted over different frequencies as shown in Figure 4.5b and 4.5c for the retina and cornea, respectively. The resonance frequency of the retina peaked at 10 Hz, which corresponded to a Young's modulus of 3.3 kPa according to the calibration data obtained previously. The response of the cornea peaked at 44 Hz, which equates to 58 kPa. The ratio of the rabbit retina to the cornea elasticity is 1:17.6, while the ratio of the swine results is similar at 1:15.8. It is also noted that while the single resonance peak is apparent in both the retina and the cornea data, many of the smaller peaks overlap. In the retina plot, there is another high peak at 16 Hz, which likely corresponds to the different stiffness between the retinal layers. In the cornea plot, there are small peaks at 10 Hz and 16 Hz, which are the effects from the retina resonance frequencies. Similarly, the retina plot also peaks highly at 44 Hz, which is the resonance frequency of the cornea. Even though the focus is on one portion of the eye, the entire eyeball vibrates with the modulated force, and all components of the eyeball are demonstrated in the frequency sweep results. The cornea has a high contribution to the retina plot due to its location and because the force must penetrate through the cornea. Many smaller peaks overlap in the retina and cornea plots in Figure 4.5, and probably signifies the other components of the eyeball. In particular, it is known that the lens strongly absorbs and refracts the ultrasound, so it must greatly contribute to the frequency response as well. Further experiments must be performed in order to determine the exact correlation.

4.6 Effects of intraocular pressure on ocular elasticity

Although the absolute elasticity can be determined from studying the frequency response, the elasticity of ocular tissue is highly dependent upon the intraocular pressure. Relatively stiff materials, such as the cornea, are largely affected by the pressure change. This phenomenon contributes to one of the major limitations of *ex-vivo* ocular studies, where the intraocular pressure is no longer preserved. The eye often collapses and is not an accurate representation of *in-vivo* tissue. In the last portion of our study, a pressure transducer was used to control the intraocular pressure of the eye, and the relationship between corneal stiffness and the pressure was observed.

The differential pressure transducer was connected to a large syringe, which regulates the intraocular pressure, as shown in Figure 4.6a. A 5 French catheter was inserted into the rabbit eye and connected to the syringe set up. Five different pressures were chosen to represent a range of intraocular pressures ranging from 0 mm Hg to 36 mm Hg. The filtered corneal frequency response is shown in Figure 4.6b. A different rabbit was used to do the experiments in Figures 4.5 and 4.6, and the difference in the frequency response is significant. This is likely due to the difference in the shape of the cornea, where the pressure-controlled sample was a round globe while the previous sample was collapsed.

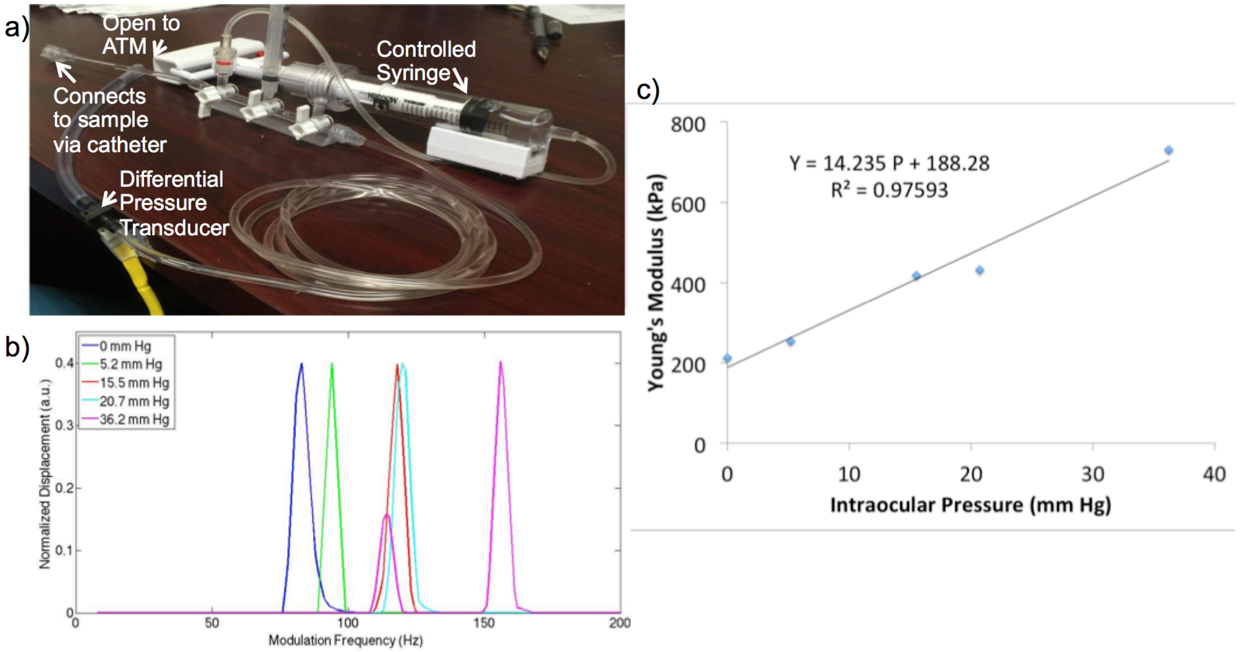

Figure 4.6 Intraocular pressure results. a) Set up for pressure modification system. b) Frequency response of cornea. c) Linear relationship between intraocular pressure and Young's modulus.

In order to quantify the elasticity of the cornea, phantom calibration results in Figure 4.3 were used to correlate the resonance frequency to the Young's modulus. The intraocular pressure and the elasticity are linearly proportional as shown in Figure 4.6c. The results verified the significant dependence of the corneal elasticity on the intraocular pressure.

4.7 Summary

In conclusion, we have reported on an ARF-OCE system using automatic frequency sweep. Phantom studies were performed for feasibility validations, and the results were compiled to calibrate the relationship between the resonance frequency and the elasticity, which corresponded with the Voigt model. In addition, cornea and retina studies were done using a pig eye by isolating the eyeball and the posterior sections. The elasticity was estimated to be 13 kPa and 206 kPa for the retina and the cornea, respectively. Last, cornea and retina frequency response measurements were taken on an intact rabbit eyeball, and the Young's moduli were 3.3 kPa and 58 kPa for the retina and cornea, respectively. Future studies will incorporate *in vivo* animal designs, as well as focused transducers to target tissue layers.

CHAPTER 5

Retinal Elasticity Mapping

In this chapter, we present a synchronized acoustic radiation force optical coherence elastography (ARF-OCE) system to measure and estimate the elasticity of cadaver porcine retina with high mechanical contrast between the layers. Section 5.1 presents an introduction to retinal elasticity and its significance. Section 5.2 introduces a novel synchronized ARF-OCE system and its synchronization scheme. Next, the central retina region near the optic nerve is imaged in section 5.3 and the data is analyzed and correlated to anatomical structures in section 5.4. Statistical analysis is performed on 64 different locations on the central retina in section 5.5, and a summary is offered in section 5.6.

5.1 Introduction:

The structure of the retina has been studied extensively. In particular, the retina consists of many sublayers that contribute to its function. For layered analysis of the retina, there have been many segmentation methods that have been used to separate the different layers within the retina (97-99). Many of these features are built into commercial imaging systems, and automatic detection is possible. The thickness of the layers and other anatomical structures can be analyzed *in-vivo* and correlated with pathology.

Elasticity changes in the retina and choroid can occur when the microvasculature changes or when drusen forms. In order to study the mechanical structure of the retina, several studies attempt to provide elastic properties by performing mechanical strain testing *in vitro* (10, 11). However, strain testing is not possible for tissues *in vivo.* In addition, the entire retina is extracted as a single unit, which means that individual layer information cannot be obtained. Although mathematical modeling of the retina to determine the Young's modulus has been reported (12), mechanical properties of the retina are still not well defined since the retina is inaccessible to many elastography methods or is limited by low resolution.

In this chapter, we use the ARF-OCE technique to map out the elasticity of the retina, with separation of 5 retinal layers. The previously used system has been synchronized in excitation, detection, and the incorporated mechanical stage scanning. In this way, the phase cycle of the tissue vibration is uniform in the direction parallel to the mechanical stage. First, structural OCT and functional OCE imaging were performed on a healthy pig retina near the optic disk and in the periphery of the retina after isolation of the posterior portion of the eye. Then the OCE phase information was analyzed along the axial direction. Then segmentation was performed on the retinal layers using OCT and the corresponding layer was matched on the OCE and histology. Nanometer displacement differences were observed between the layers. Finally, the relative stiffness was analyzed over 64 B-scan samples and statistical analysis was performed. The Young's moduli are estimated for each layer using the experimental stiffness ratios and average elasticity obtained from literature.

5.2 Synchronized system design

Similar to the previous chapter, an ultrasonic focused ring transducer was used for excitation while a SD-OCT system was used for detection of the tissue response. The acoustic and optical signals are all synchronized using the computer in order to obtain images with synchronized vibrational responses. A schematic diagram of the system set up is illustrated in Figure 5.1, where a mechanical stage has been added for large field scanning purposes.

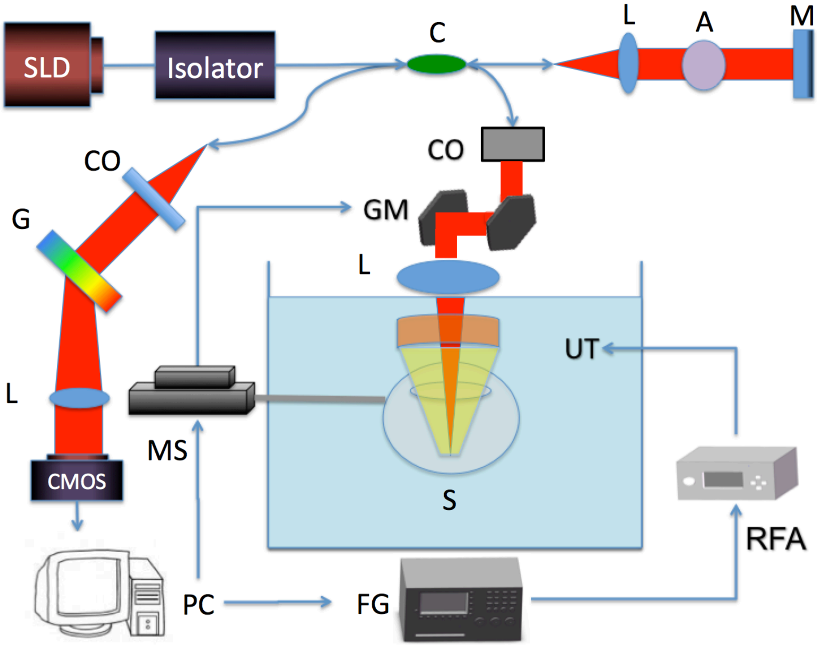

Figure 5.1 Schematic diagram of system setup. SLD: superluminescent diode, L: lens, G: diffraction grating, CMOS: camera, C: coupler, A: attenuator, M: mirror, MS: mechanical stage, GM: galvo mirror, UT: ultrasound transducer, S: sample, RFA: radio-frequency amplifier, FG: function generator, CO: collimator.

The function generator first outputs a modulated square wave signal of 833 Hz, which is amplified by approximately 170 times and fed to a 4.5 MHz ring US transducer with a focal distance of 3 cm. ARF using approximately 40V post-amplification is induced on the sample and vibrations are generated. A modulation frequency of 833 Hz, which is much higher than the resonance frequency of retinal tissue, was chosen so that the mechanical contrasts of the layers are not skewed by resonance vibrations. On the detection side, the optical set up highly resembles that of previous publications. The power from the sample arm is measured to be 0.89

mW, which is well below the safety limit determined by the American National Standards Institute. In order to optimize imaging conditions, especially to maximize imaging range, a mechanical stage has been incorporated into the system to move the sample. The sample is fastened to the mechanical stage via metal posts and the sample is mobilized in discrete steps during imaging. In this way, the limitation set forth by the 500 um uniform focal diameter of the transducer can be bypassed. One galvanometer mirror is used for scanning in one lateral dimension while the motorized stage provides scanning in the other lateral direction. This increases our imaging range from 500 um to over 3 mm and at the same time provides more uniform excitation across B-scans. A 20 kHz A-line rate is used and a volumetric scan in these experiments consists of 500 by 500 A-lines.

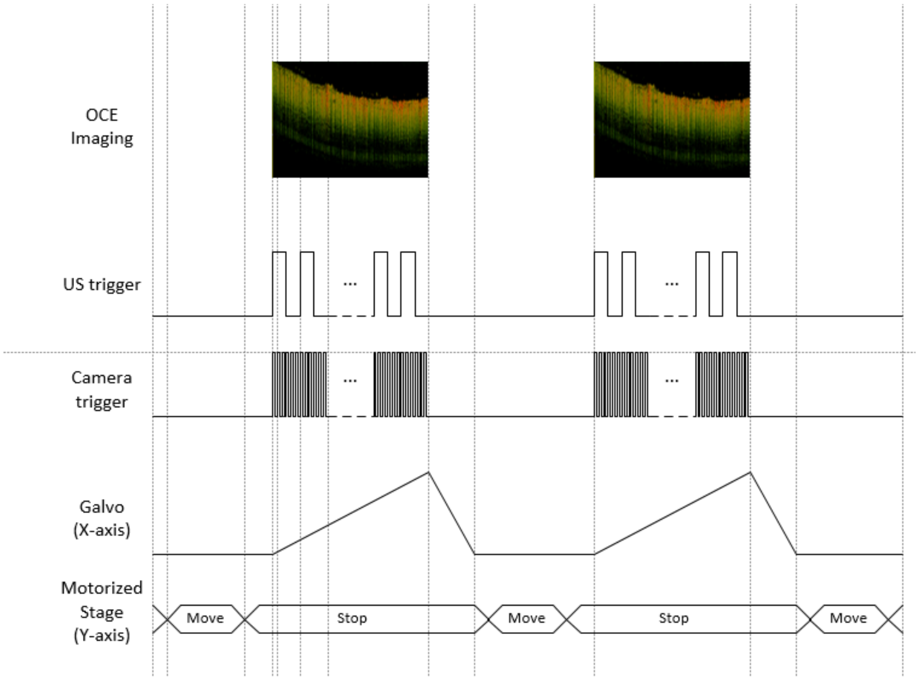

Figure 5.2 Timing diagram of system showing excitation and detection.

Synchronization between the acoustic excitation and optical detection was performed as shown in Figure 5.2. In this way, it is possible to control the phase of the modulation cycle at different spatial locations on the sample. A 0.1 ms pause was incorporated into the system to minimize noise caused by the movement of the motorized stage. The galvo sweeping, camera acquisition, and ultrasound modulation signals are triggered at the same time when the motorized stage is stationary to produce a single B-scan. Then the motorized stage shifts in a preset increment smaller than the lateral resolution of the system, and another B-scan is acquired. For the results shown here, a 6 um displacement is achieved for each step.

5.3 Retina and optic disk imaging

A porcine eyeball was isolated within 24 hours of death and the anterior of the eye was removed so that only the vitreous fluids and the retina/sclera remained. The eyeball was then fixed using agar gel and mounted to the imaging stage in the water bath. The optical disk was identified on the retina by its diameter of approximately 1.7 mm. Using the synchronized system, a region of 3 mm by 3 mm was scanned near the optical disk. Previously, only the middle 500 um by 500 um region can be assumed to have uniform excitation, but with the addition of the mechanical stage, a region of 500 um by 3 mm is able to achieve uniform force. This expands our imaging region by 6 fold in this figure.

The OCT cross-sectional image showing the optical disk region is displayed in Figure 5.3a, while the corresponding OCE phase map is displayed in Figure 5.3b. The B-scan shown is in the same direction as the movement of the mechanical stage. Within this B-scan, an accurate uniform acoustic field is guaranteed for elastography since synchronization allows for phase cycle uniformity in the direction perpendicular to the galvo scanning.

The OCT and OCE images of the peripheral retina is shown in Figure 5.3c and 5.3d, respectively. The same scanning mechanism was used over a 3 mm by 3 mm region after shifting the focus to the peripheral retina. It is clear that the optical disk region had a much smaller vibrational response, indicating a stiffer tissue, than the peripheral retina and the regions closer to the optical nerve head. The pocket structure in the middle of Figure 5.3b had a very high vibrational response, which indicates a softer tissue that is concluded to be a collapsed blood vessel. This figure portrays the relative elasticity of the optical nerve to the peripheral retina and demonstrates the feasibility of using ARF-OCE in the mapping of retinal elasticity. It was also noted that the relative stiffness of the retina changes in the axial direction, suggesting the separation of different layers, with the top layer indicating the softest structure.

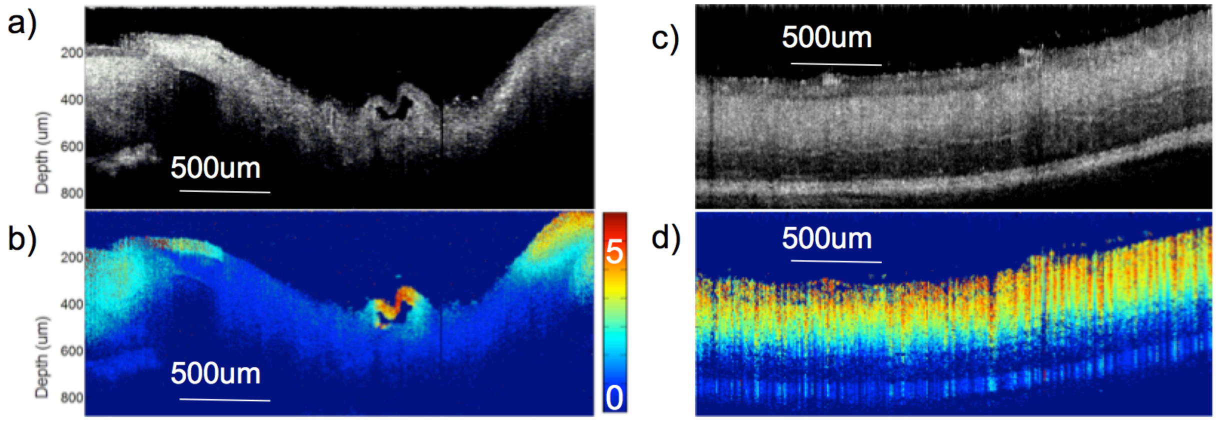

Figure 5.3 Optical disk and peripheral retina imaging. a) OCT cross-section of optical disk. b) OCE phase cross-section of optical disk. c) OCT cross-section of peripheral retina. d) OCE phase cross-section of peripheral retina.

5.4 Segmentation and histological correlation

Since different layers were observed both in the OCT intensity images and the OCE phase images, segmentation was performed on the OCT images using a graph-based method. A random walk algorithm was also used for refinement of the layers. From experimental results, 5 different axial layers could be isolated as shown in Figure 5.4a. The OCE small interval displacement image in Figure 5.4b was also segmented using the same boundaries. Segmentation was not performed on OCE directly since we have yet to validate the stiffness contrast corresponding to the boundaries between layers. Figure 5.4c shows the corresponding elastogram with Young's modulus values, which were derived from previous experiments that showed a bulk Young's modulus of 13 kPa of all the layers. According to porcine retinal anatomy, there are ideally 7 layers that can be separated, but were not visible in these results. Therefore, histology using H&E staining was performed shown in Figure 5.4d to match the imaging layers to anatomy. The top three layers, including the nerve fiber layer, ganglion cell layer, and inner plexiform layer, were compressed into a single detected layer. This is probably caused by the deterioration of the tissue after harvest, also as indicated by the collapsed blood vessel near the optic disk in Figure 5.3b. Experiments were performed approximately 40-48 hours after tissue harvest, and it is likely that degradation occurred during storage and transport.

The boundaries for the inner nuclear layer was highly distinguishable from the OCT images, and the mechanical elasticity also showed contrast between upper and lower layers. Within the inner nuclear layer, there seems to be a displacement gradient in the axial direction, with a redder color on the inside and a green color on the outside. This is due to the connective boundaries between the layers that vibrate together. In subsequent measurements, this gradient was taken into account and the entire axial displacement information was considered. The outer plexiform layer is relatively thin and displacement values continue to decrease. The outer nuclear layer is difficult to visualize on the OCT image, since its properties allow for low scattering of optical light. Therefore, it was omitted in the quantitative analysis. The outermost layer of the retina is the photoreceptor region, which had high scattering contrast, but low displacement values.

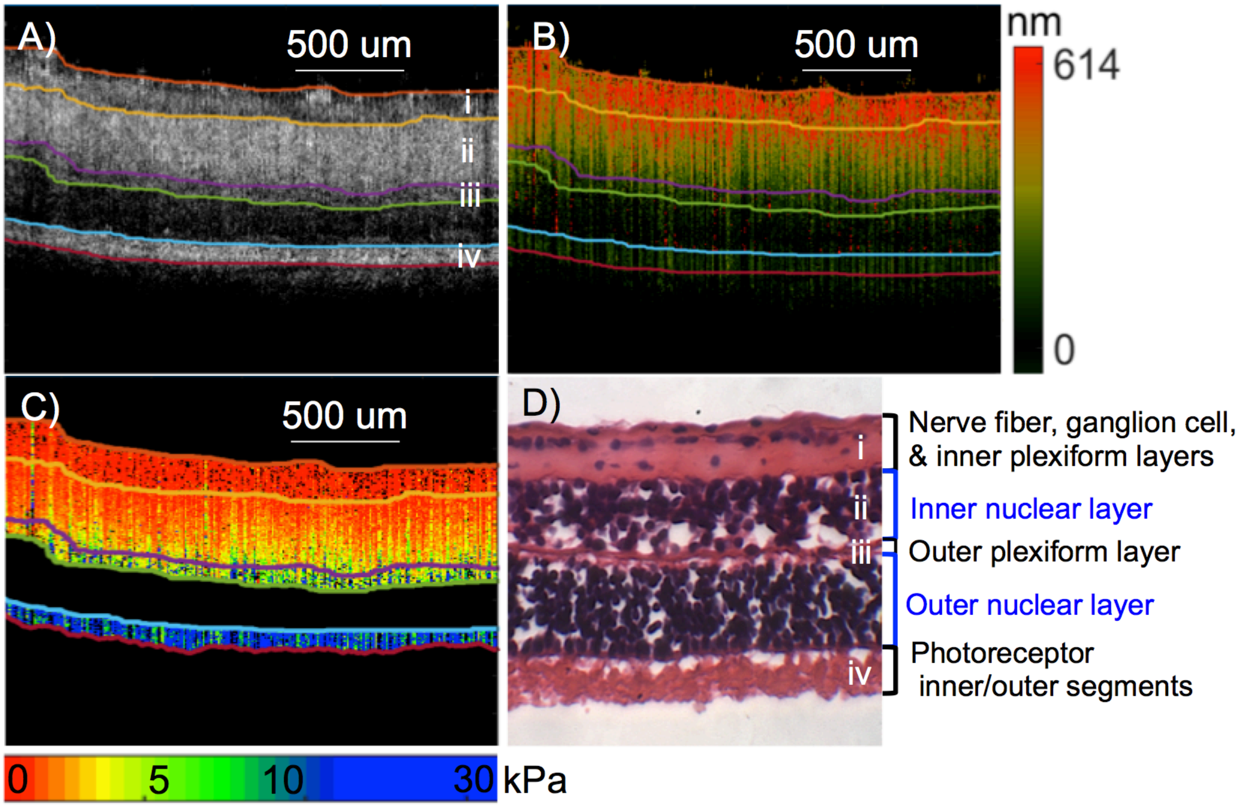

Figure 5.4 Retina segmentation and elastogram. a) OCT segmentation. b) Corresponding segments of OCE displacement mapping. c) Corresponding elastogram. d) H&E staining of porcine retina with the anatomical layers labeled.

From analysis of Figure 5.4, it can be concluded that the OCE displacement map is not affected by the difference in OCT intensity. As long as there is some scattering, the relative displacement can be measured. In this case, the depth penetration was enough to capture the retina. In the onset of AMD, drusen can form in the retinal pigment epithelium (RPE) layer, which is directly underneath the photoreceptor layer shown. A higher output power or a longer central wavelength can be used to increase imaging depth.

5.5 Statistical analysis

In order to verify the consistency of the relative layered stiffness over the entire retina, 64 cross-sectional OCT and OCE B-scans were obtained at different spatial locations on 2 retina samples. Segmentation was performed on OCT images and the respective OCE segments were analyzed. Five different retinal layers were isolated and the thickness of each layer was estimated by counting the axial pixels and averaging over the lateral direction. The results are summarized in Table 5.1. The entire thickness of the retina was approximately 400 um.

Since each of the 64 images varies in their phase cycle, it is necessary to normalize all the displacement values to a relative scale so direct comparisons can be made according to the ratios. In this case, the value of the highest displacement was set to be 1, and the other displacement values are portrayed as a fraction of the maximum. As shown from previous publications, the Young's modulus is inversely proportional to the displacement values, but only relative displacement ratios are available. Therefore, the elasticity estimations are based on modeling results from previous experiments, which estimated the overall Young's modulus of the entire retina to be 13 kPa. A weighted average approach was used where the weight contribution was dependent on the thickness of the respective layers, and the mean was set to 13 kPa. The results are shown in Table 5.1, where the Young's modulus was estimated anywhere from 1 to 26 kPa.

The outer nuclear layer was omitted from this estimation since scattering signal was too low for proper detection of OCE.

According to the results for 4 retinal layers, it seems that the inside layer on top of the retina is much softer than the bottom layers, which is getting closer to the sclera. This is expected since the sclera is much stiffer than the retina as determined from previous publications. A total of 64 B-scans were analyzed to correspond to 80% confidence level with 8% confidence interval. However, further analysis is necessary to accurately measure the retinal layers between several different samples.

Retinal Layer	Mean Thickness (um)	Normalized Displacement	Young's Modulus (kPa)
Nerve fiber layer Ganglion cell layer Inner plexiform layer	**67**	**0.99**	**1.33 ± 0.37**
Inner nuclear layer	**132**	**0.48**	**2.73 ± 0.82**
Outer plexiform layer	**37**	**0.17**	**7.7 ± 2.26**
Outer nuclear layer	**84**	**N/A**	**N/A**
Photoreceptor inner/outer segments	**72**	**0.06**	**25.9 ± 7.36**

Table 5.1 Total of 64 B-scans analyzed and the thickness and displacement values were estimated. Young's moduli were estimated using a weighted average approach. Outer nuclear layer omitted due to low scattering signal.

5.6 Summary

This study using ARF-OCE technology is the first to visualize the mechanical properties of individual retinal layers, where 4 distinct layers were quantified. An ARF-OCE system was set up with synchronized excitation, detection, and scanning for better control of the modulation phase cycle. By analyzing the cross-sectional images perpendicular to the galvanometer scanning direction, it can be guaranteed that the B-scan shows a synchronized vibration in a uniform phase cycle. Using this approach, elasticity maps were obtained for the peripheral retina and the optic disk regions. Segmentation was performed on the OCT images and the corresponding layers were separated in the OCE, and both were matched to histology results using H&E staining. Further analysis was performed on 64 B-scans to estimate the thickness of the 5 layers as well as the relative displacement values. Using a weighted average method, the Young's moduli for 4 different retinal layers were estimated. The ARF-OCE technology was used to quantify retinal layered elasticity and is adaptable to *in-vivo* applications. The translation of this technology provides a powerful tool for the clinical diagnostic management of AMD.

CHAPTER 6

In-vivo Real Time Retinal Elasticity Mapping

In this chapter, we used acoustic radiation force optical coherence elastography (ARF-OCE) to map out the elasticity of retinal layers in healthy and diseased in-vivo rabbit models for the first time. The significance of in vivo retinal elasticity imaging is discussed in section 6.1. The in vivo setup and experimental design is presented in section 6.2 while the mechanical quantification scheme is discussed in section 6.3. Section 6.3 examines the imaging results from a healthy in vivo rabbit model. In section 6.4, a pathological retinal model is custom designed and a difference in the mechanical contrast is observed between the healthy and diseased regions. The chapter ends with a summary in section 6.5.

6.1 Introduction:

While age is the greatest contributing factor for AMD, other risk factors include: being white or female, exposure to certain light wavelengths, history of cardiovascular disease, smoking, etc. (100). The most common form of AMD is known as dry/ non-exudative AMD, which presents with drusen, which are composed of oxidized nondegradeable material (mostly lipofuscin), that develop between Bruch's membrane and RPE layers of the retina. In the early stages of dry AMD, the patient may have metamorphopsia, reduced vision, or be completely asymptomatic; thus, the variable presentations highlight the need for the earliest detection methods (4, 5, 100).

Since no cure currently exists for AMD, several imaging modalities and techniques are used in AMD detection and monitoring including: fundus autofluorescence (FAF), fundus photography, OCT, fluorescein angiography, indocyanine green angiography, and Amsler grid, etc. (6, 100, 101). FAF relies on the fluorescence pattern of the oxidation compound lipofuscin contained in high amounts in the drusen (102). OCT can identify abnormal blood vessel formation in wet AMD through OCT angiography (90, 100). Although these imaging modalities and techniques provide crucial information for the diagnosis of AMD, they are often insufficient for early diagnosis, before structural changes occur.

The mechanical properties of distinct cellular layers in the retina are altered with the onset of AMD (9), but it is challenging to detect thin layers in the micron range without perturbing the natural retinal environment. Although mechanical quantification of the cornea has been previously performed with ARF-OCE (67, 103, 104), the location of the retina and its thin layers require high penetration, high resolution, and high sensitivity. These major complications have hindered previous elastography imaging techniques, and mechanical quantification of the *in-vivo* posterior eye is presented for the first time in this chapter. A technology that enables the *in-vivo* imaging of the posterior ocular globe is essential for gaining insight into the natural mechanical anatomy of the eye, as well as the changes that take place with ocular diseases.

In this study, ARF-OCE is used to provide phase-resolved displacement information on the central retina for both a healthy and abnormal *in-vivo* rabbit eye. Quantification of the layers uses a graph-based segmentation algorithm (97), and using a simple Voigt model. We demonstrated for the first time, to the best of our knowledge, *in-vivo* quantitative elasticity map of the retina. In addition, a general trend was observed between the healthy and the damaged rabbit retina.

6.2 In vivo system design

A schematic diagram of the *in-vivo* ARF-OCE system setup is shown in Figure 6.1a and a close up of the imaging setup is illustrated in Figure 6.1b. The optical components are similar to the system used in the previous chapter, and the primary difference is in the sample arm. A galvanometer scanner is used to sweep across the sample and a scan lens is used to focus the OCT light onto the retina. For the purpose of *in-vivo* imaging, a custom phosphate-buffered saline (PBS) bath is used, where a large red ring holds a sheet of flexible latex that is filled with PBS. A small aperture is made at the bottom of the latex sheet, where it goes directly over the proptosed rabbit eye. The ultrasound transducer is used for excitation of tissue displacement, and is placed directly inside the PBS bath, which acts as a propagation medium for the ultrasound. The ring acoustic transducer is aligned to be exactly confocal with the OCT beam using a hydrophone before the experiment to ensure that data acquisition is performed within the lateral focal region of the transducer and that maximum tissue response can be measured.

Detection of the tissue response is performed using a CMOS camera, where the interference signal is extracted through real-time processing and converted to both OCT intensity images and phase-resolved displacement maps. The axial resolution of the imaging system is approximately 3 µm with a lateral resolution of 27 µm in air. The phase sensitivity of the elastography system is in the nanometer scale, which allows for high displacement contrast.

The actual setup can be visualized in the photograph shown in Figure 6.1c. With such an *in-vivo* system, the rapid degradation of the retina occurring in post-mortem models is avoided. The rabbit is one of the few animals whose eye can be proptosed. The ring ultrasound transducer was taken out of Figure 6.1c so that the proptosed eye could be visible. As shown in the timing diagram in Figure 6.1d, the OCT detection uses C-mode to detect the mechanical response, with a line scan rate of 20 kHz, and B-frame rate of 20 frames per second. The acoustic pulse is continuously modulated during the OCT acquisition at a frequency of 833 Hz with a 50% duty cycle, which corresponds to a pulse width of 0.6 ms. The modulation pulse was again chosen so that it is relatively far away from the resonance frequency of tissue, which is typically below 100 Hz, and the value corresponds to a 1.2 msec period. Other frequencies much higher than 100 Hz would also be acceptable, as long as the vibrations are slow enough to be captured by the detector. The lateral focal region was limited at approximately 400 µm to guarantee high

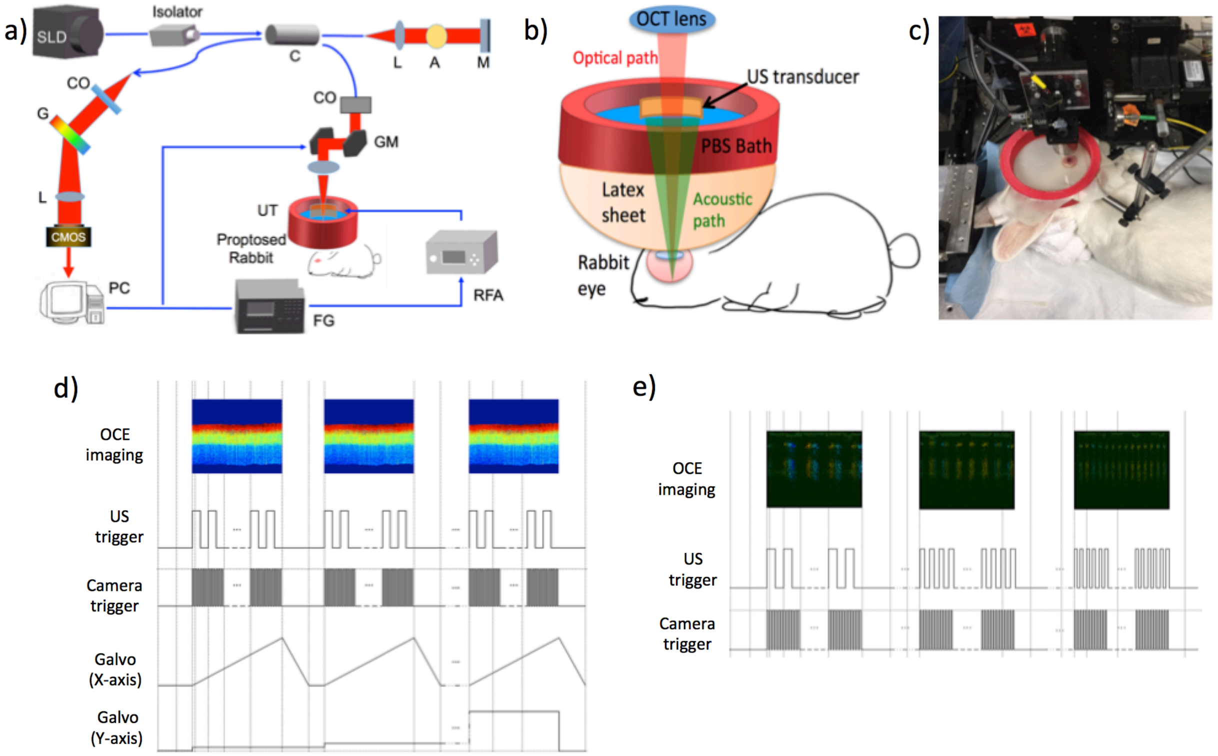

Figure 6.1 System setup for *in vivo* studies. a) Schematic diagram of system. b) Close up schematic of sample arm. c) Photo of the setup with the rabbit eye proptosed on the stage. d) Timing diagram of OCE modulation imaging. e) Timing diagram of OCE frequency sweep.

sensitivity imaging within a uniform pressure region, while the axial focal region was extended at more than 5 mm to guarantee that the pressure distribution differs by less than 0.1 dB over the imaging depth. The acoustic intensity within the 400 μm lateral region and the 1 mm axial region have been shown to be uniform in chapter 3, so any displacement differences in this region can be attributed to changes in mechanical properties. For all experiments presented here, the central retina region 2 mm from the optical disc on the temporal side of the retina was imaged, corresponding to the area of highest visual acuity. Both the OCT and phase-resolved displacement information was obtained and recorded. The displacement information is converted to the elastic modulus with a simple Voigt model and a spring model.

6.3 Quantification scheme

Quantification of the elasticity is summarized by equations 2.10 and 2.11, and performed by using the bulk frequency response of the entire depth of the posterior orbit with a simplified 5-spring model to isolate individual layers, which will represent the sclera, choroid and three retinal zones. First, the resonant frequency peak is determined by doing M-mode imaging while modulating at different frequencies, and measuring the displacement level. The frequency at which the highest displacement occurs is the resonant frequency peak. In this case, a sweeping mechanism from 1 Hz to 100 Hz has been implemented, with 0.1 Hz increments, shown in the timing diagram in Figure 6.1e. We used a silicone phantom with similar elasticity and thickness to the retina to calibrate the measurement of elastic modulus using equation 1. The resonance frequency was determined to be ~15 Hz. The resonance frequency and the Young's modulus is related by: $E = \mu^2 * 0.03$. The bulk Young's modulus of the entire depth of the sample can be calculated to be ~7 kPa.

The frequency sweep method can only quantify the bulk elastic modulus of the entire imaging depth of the sample at the region of excitation. The elasticity is quantified as stress over strain, where the strain values are inversely proportional to the displacement. Because the force of the ARF is difficult to quantify directly, the stress on the sample cannot be quantified. The OCE images measure the displacement of the sample at each location, assuming a uniform ultrasound stress field within the transducer focal region. This means that the relative elasticity of each layer can be measured spatially according to the OCE, but the absolute Young's modulus requires an additional model to calculate the individual layer elasticity.

It can be assumed that the layers of the retina, choroid, and sclera are a series of springs attached to each other with the bottommost layer fixed at a boundary. In this experiment, the bulk elasticity for the entire depth, including the retina, choroid, and sclera, is obtained based on the frequency sweep mechanism in Figure 6.1e. The total thickness and the thickness for individual layers were found using the segmentation algorithm on OCT B-scans. The relative ratio of the elasticity for each individual layer was determined based on the depth-dependent displacement map, as shown in Figure 6.1d, by using the modulated excitation approach. Finally, with the relative ratio between the layers and the quantified bulk Young's modulus, as well as the layered and bulk thicknesses, the absolute Young's modulus can be determined for each layer using equation 2.11. Last, the spatial distribution of the elastic moduli can be quantitatively mapped out using the relative vibrational displacement response that is measured using ARF-OCE with the mean value based on the individual layer elasticity.

6.4 In-vivo healthy rabbit study

The rabbit eye is the ideal model for this study due to the ability to proptose the eye conveniently, for bathing in ultrasonic conductive medium such as PBS, and without inflicting damage. For translation into clinical trials, ocular gel or a waterbath with a steridrape can be used to couple the ultrasonic radiation force into the retina. This is routinely used in clinical ophthalmic ultrasound, and would not be expected to be problematic for clinical translation.

The first New Zealand White rabbit was assumed to have a healthy ocular anatomy and imaged. The structural re-sliced OCT image was obtained as shown in Figure 6.2a, where individual posterior layers of the eye could be isolated using the graph-based segmentation algorithm (97). A re-sliced image in the Y plane is used since the ultrasound excitation is synchronized in that direction, while the B-scans in the X plane displays the modulated signal. It is apparent that not all layers of the retina could be differentiated and some distortions can be seen, most likely due to the bulk motion during *in-vivo* imaging caused by rabbit breathing or external noise as well as the limited imaging speed of 20 kHz. The ocular layers on the OCT were matched anatomical structures and verified by previous literature (105). The relative OCE displacement map is shown in Figure 6.2b, where higher displacement was seen on the ganglion side, and decreases toward the photoreceptor side, signifying the change in relative elasticity of the different layers. The frequency response of the tissue was obtained, and the resonance frequency peak was used to calculate the bulk Young's modulus of the tissue, which was determined to be approximately 7 kPa. Using the spring model and a weighted average, the corresponding elastogram was generated in Figure 6.2c.

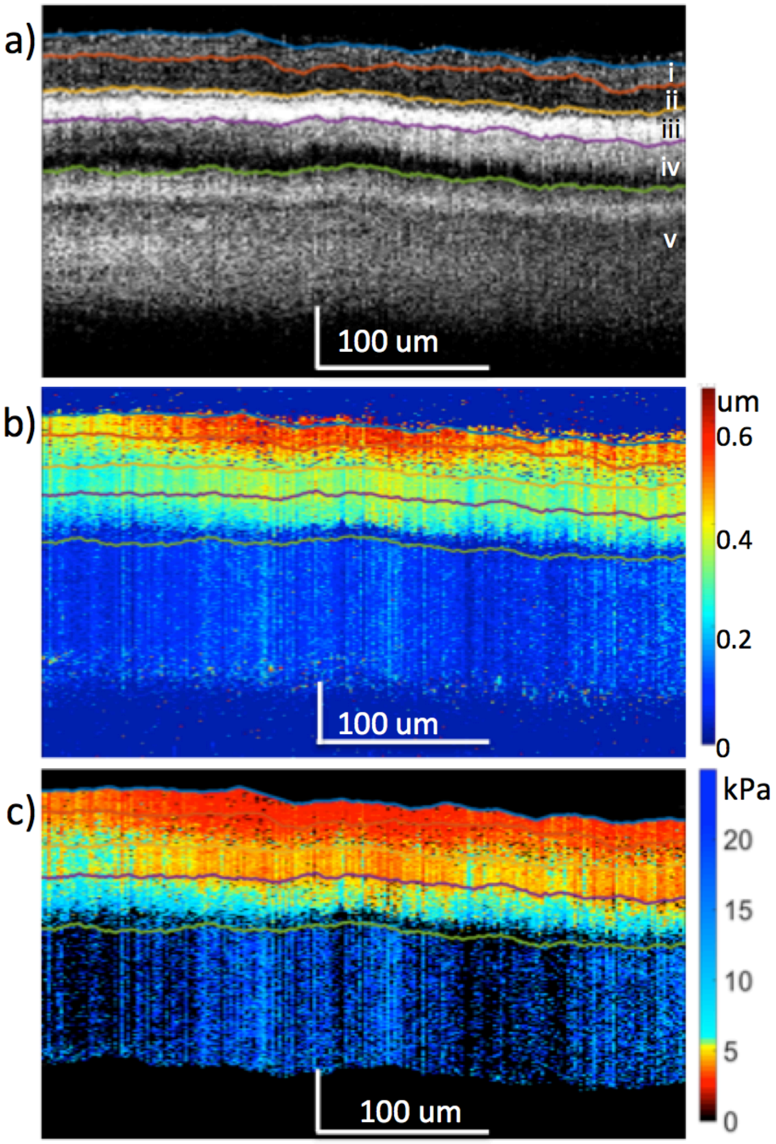

Figure 6.2 The *in-vivo* rabbit posterior eye results. a) OCT. b) OCE displacement map. c) Elastogram. Layer i: optic nerve fibers, ganglion cell layer, and the inner plexiform layer, layer ii: inner nuclear layer, outer plexiform layer, and the outer nuclear layer, layer iii: RPE, layer iv: choroid, layer v: sclera.

According to the OCT and elastogram results, the retinal, choroidal, and scleral layers appear to be relatively uniform in the lateral direction, which is expected of healthy retinal tissues. Images of the OCT and OCE at different locations on the central retina within the region of ultrasound excitation are presented in Figure 6.3a and 6.3b, respectively, where similar patterns and trends can be observed across different layers. After averaging across 64 locations on the temporal retina, the mean stiffness of each layer is summarized in Figure 6.3c with the mean and standard deviation estimated for each layer. According to the thickness of the OCT layers and their correlation to the histological image, the layers were matched to their respective Young's modulus. Due to the smaller thickness of the New Zealand White rabbit's posterior orbit, it was possible to obtain a signal from the choroid and sclera layers below the retina. It is important to note that there was tissue edema observed in the sclera, which was possibly due to the eye proptosis as well as the constriction caused by the elastic sheet setup.

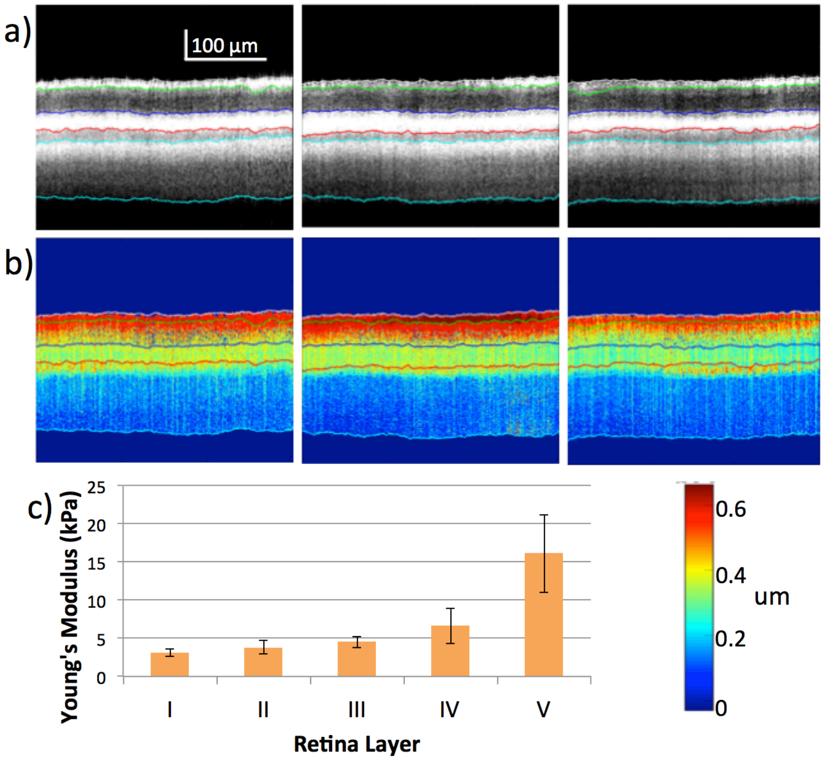

Figure 6.3 Posterior eye results from New Zealand White rabbit at different location in central retina. a) OCT images of the central retina at increments of 75 um within 400 um focal region. b) OCE images of corresponding region. c) Summary of elasticity from layers I to V.

6.5 In-vivo rabbit damaged retinal study

In order to test the feasibility of the ARF-OCE imaging system on detecting diseased states, we induced retinal damage on a second New Zealand White rabbit, primarily using blue light exposure. All rabbit experiments are performed with adherence to the guidelines set forth by the UCI Institutional Animal Care and Use Committee. In order to induce damage on the rabbit retina, the rabbit was treated with a high fat diet, blue light exposure, and nicotine for 8 weeks total, as outlined in Table 6.1. Similar animal models using rodents and rabbits have been previously published (106, 107). The rabbit was exposed to blue light for 2 hours a day, 5 times a week for 8 weeks, by lining the cage with blue light LED strips as shown in Figure 6.4. The rabbit was imaged every 2 weeks, from week 0 to week 9, according to the protocol, and

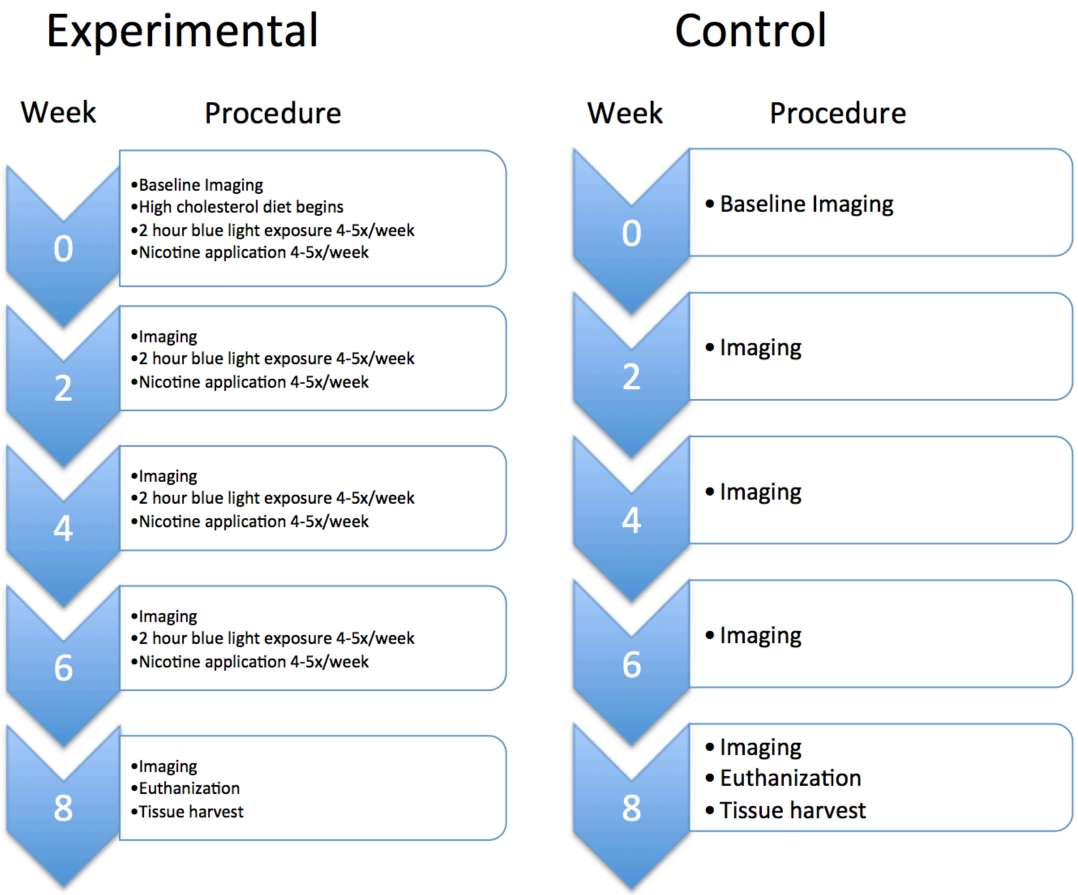

Experimental

Week	Procedure
0	•Baseline Imaging •High cholesterol diet begins •2 hour blue light exposure 4-5x/week •Nicotine application 4-5x/week
2	•Imaging •2 hour blue light exposure 4-5x/week •Nicotine application 4-5x/week
4	•Imaging •2 hour blue light exposure 4-5x/week •Nicotine application 4-5x/week
6	•Imaging •2 hour blue light exposure 4-5x/week •Nicotine application 4-5x/week
8	•Imaging •Euthanization •Tissue harvest

Control

Week	Procedure
0	• Baseline Imaging
2	• Imaging
4	• Imaging
6	• Imaging
8	• Imaging • Euthanization • Tissue harvest

Table 6.1 Diseased rabbit model description.

sacrificed. During imaging, the rabbit was first injected with 35 mg/kg of ketamine and 5 mg/kg of xylazine subcutaneously. For topical anesthesia, 2 drops of proparacaine HCl was applied. Topical atropine solution was also added for dilation of the eye. Once the rabbit becomes unconscious, he is placed on the imaging stage and the eye is proptosed. During imaging, the heart rate and oxygen saturation levels are consistently monitored and additional anesthesia via subcutaneous injection of ketamine is added with 17.5 mg/kg. After imaging, the rabbit is given buprenorphine for pain management as necessary, and is monitored closely until it becomes fully conscious. In the final terminal imaging, the rabbit is catheterized via the ear and injected with euthasol. OCE imaging from weeks 4 and 8 were compared. At the end of 8 weeks, the rabbit was imaged and sacrificed.

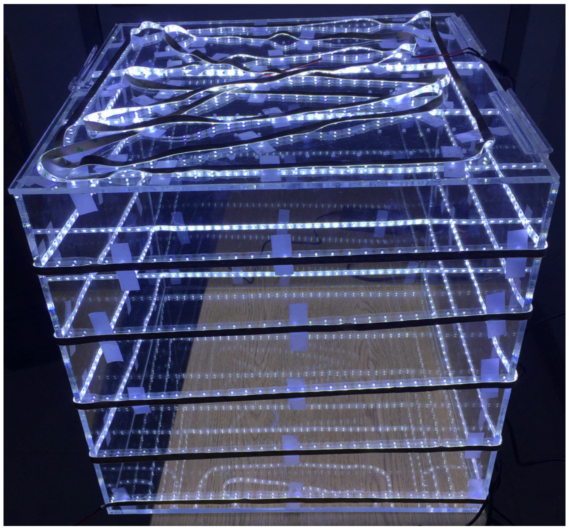

Figure 6.4 Rabbit blue light exposure chamber.

The rabbit was placed in a transparent chamber with 225 W of cool white LED's lining 5 faces of the chamber. Since cool white LED's are expected to have a high concentration of blue light in the 470's range while not causing pain to the rabbit, they are the ideal candidates (108, 109). Blue light has been shown to cause AMD in moderate amounts, and are one of the major risk factors in retinal diseases (110, 111). The 3D central retina region 2 mm away from the optic disc on the temporal side was imaged. During the first 4 weeks of treatment, no retinal damage was observed, as shown in Figure 6.5a and 6.5b. The OCT image showed a smooth transition throughout the layers, while the OCE and elastogram maps were very similar to the healthy eye from the first rabbit not damaged with light.

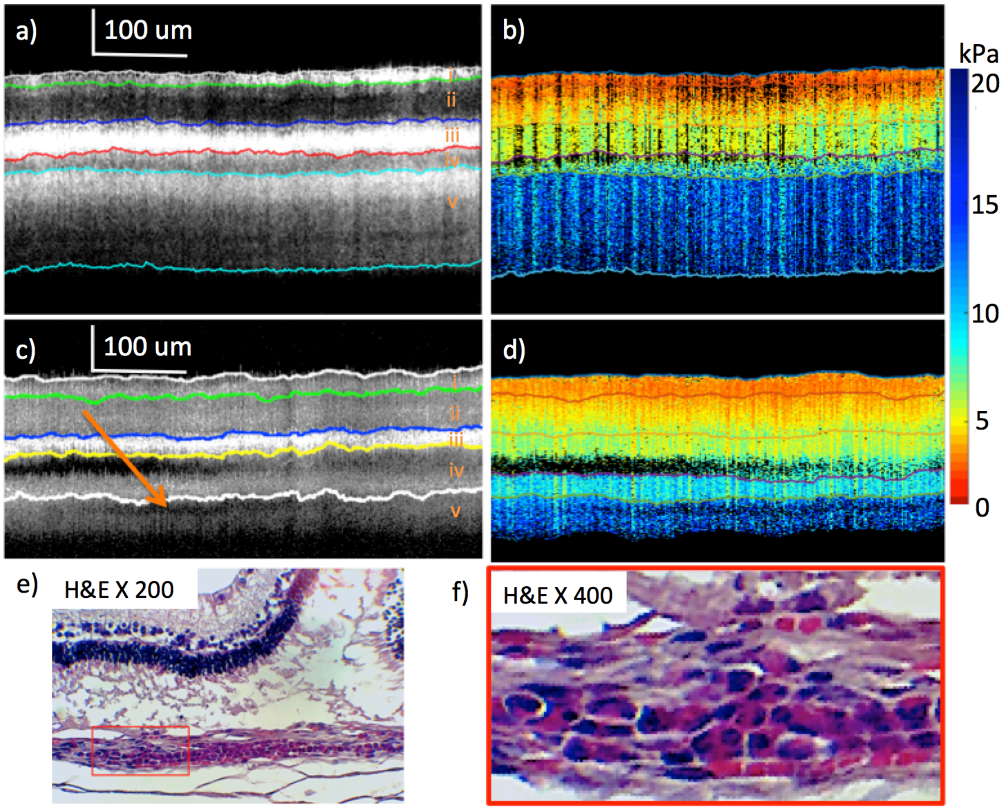

Figure 6.5 Healthy vs. abnormal rabbit from weeks 4 and 8 imaging after light treatment. a) OCT of healthy retina at week 4. b) Elastogram of healthy retina at week 4. c) OCT of abnormal portion of retina at week 8. d) Elastogram of abnormal portion of retina at week 8. e) H&E staining after euthanization at week 8. f) Higher magnification H&E histology. Red box includes photoreceptor/RPE debris with round cell accumulation in underlying choroid and presumed lymphocyte filtration. Orange arrow (c) points to presumed lymphocytic infiltrate in choroid, resulting in low OCT signal.

After 8 weeks of treatment, imaging was performed and shown in Figures 6.5c and 6.5d. The OCT image showed a dark region between the bright RPE layer and the choroid, which corresponds with the detachment. There is also an irregular pocket of low scattering OCE signal in the choroid layer. In addition, it seems that the light penetration of the damaged retina is shallower than that of the relatively healthy one, as shown by the thinner section of sclera that can be observed in layer v. Histological analysis was performed and is shown in Figures 6.5e and 6.5f. After analysis by a pathologist, it was determined that there was inflammation, causing a presumed lymphocytic infiltrate due to the prolonged blue light exposure. During histopathological examination we found mononuclear round cells in a small focal accumulation in the diseased rabbit choroid. We speculate these were lymphocytes responding to the retinal injury. From the literature, lymphocytes typically appear with a low OCT scattering signal, and inflammation can lead to reduced stiffness in the membrane (112-114). This observation means that the low signal region on the choroid corresponds to the region of inflammation. The fold in the retina on H&E is most likely caused by formalin fixation shrinkage artifact, as determined by the pathologist. Once again, swelling was observed in the sclera layer, which is likely caused by proptosis conditions.

Although some abnormalities were seen in the OCT, the elastogram looks very similar between the imaging performed at weeks 4 and 8. In order to identify differences, the Young’s moduli values for each layer has been summarized in Figure 6.6, where the relatively healthy data at 4 weeks of treatment and the abnormal regions at week 8 are shown. An overall trend was observed where the top 4 layers are generally softer for the healthy tissue. The bottom layer is the only layer where the healthy site is stiffer than the abnormal site. According to literature, the stiffness of lymphocytes is approximately 1 kPa or even lower (113, 114). Therefore, it is likely that the lower stiffness in layer v of the abnormal rabbit is caused by the infiltration of lymphocytes in the region of inflammation. One rabbit eye was analyzed using the diseased model, averaging across 500 A-lines, and while a trend was observed, the results were not statistically significant. Further *in-vivo* studies are necessary to verify the trend across different eyes.

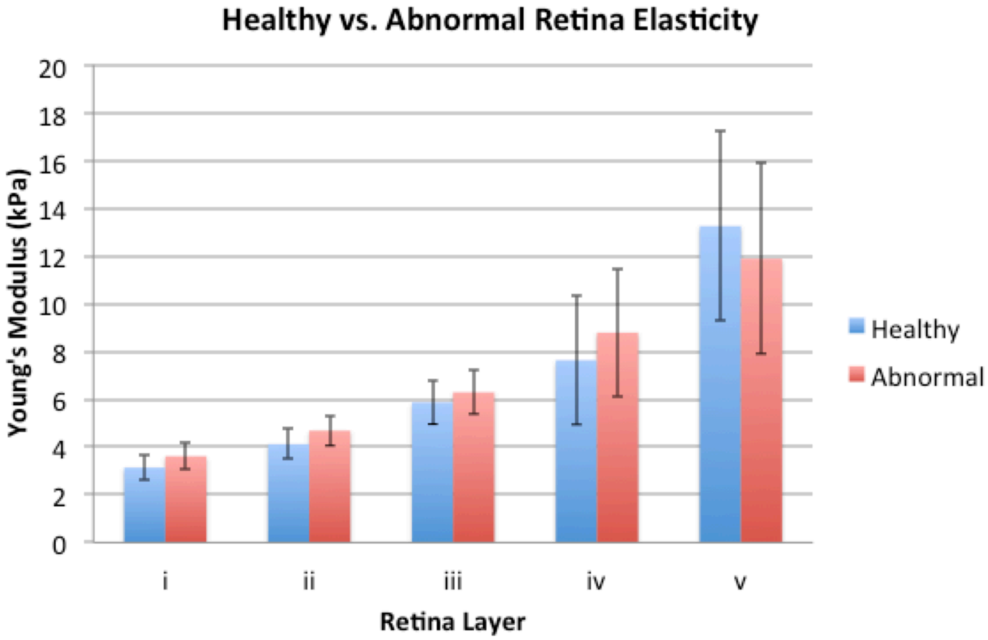

Figure 6.6 Histogram of relatively healthy and damaged rabbit posterior eye elasticity.

6.6 Limitations for clinical translation

Although we demonstrated the imaging and quantification of mechanical properties of the retina *in-vivo,* there are a number of challenges that must be overcome to translate the technology for clinical applications. First, the current acoustic intensity using to induce tissue motion exceeds the FDA 510k guidelines for diagnostic ultrasonography of the eye. The FDA ophthalmic standard for mechanical index (MI) is 0.23 while our MI is close to 2. However, the current ARF induced displacement is hundreds of nanometers, while the phase sensitivity of our imaging system is less than 1 nanometer (115). Therefore, decreasing the excitation voltage by 10 fold will be feasible, and keep the system within the safety limits. Further tests must be performed to determine the minimal excitation that is necessary to maintain adequate mechanical sensitivity. Second, the current imaging field of view is limited to below 1 mm, with the transducer excitation area as the primary limiting factor. In addition, the lateral focal region is only 400 um, it is difficult to image the entire central retina region. Adaptation of an array transducer that enables excitation at multiple locations on the retina will be necessary to image biomechanical properties of the full central retina.

In addition, during each imaging session, co-location is assured by first finding the location of the optic disk, and then moving 2 mm on the temporal side. With this method, exact alignment between each time point and correlating to histology is difficult. However, as demonstrated in figure 3a and 3b, the retinal layer elasticity trend is quite uniform across the central retina, so the comparison between healthy and diseased models remains valid. With respect to histology, there are features that can be seen within 200 um of the presumed region, where the histology matches with the OCT image, which is extremely helpful in co-alignment.

The condition of proptosis definitely affects the properties of the retinal layers. The scleral edema that has been observed is most likely due to scleral injection or vessel dilation resulting from proptosis. In addition, the behavior of the choroidal response pattern in proptosed vs non-proptosed eyes is drastically different (116). Proptosis increases the intraocular pressure of the eye, which led to choroidal edema that is likely caused by choroidal injection. Proptosis may well have an effect on layer response due to vascular congestion (116). However, studies presented here emphasize relative changes over time or compared to normals in the proptosed state, so the results still provide valid information on relative changes. In future studies, methods for performing the procedure without proptosis are being considered, including the clinical steridrape setup as well as using ultrasonic gel for index matching.

6.7 Summary

Quantified elasticity maps of the *in-vivo* posterior eye are presented for the first time, using a proptosed rabbit eye model. This minimally invasive technology offers high resolution and high sensitivity for penetration directly into the individual posterior eye layers. The ARF-OCE system enables *in-vivo* imaging of the retina, which is essential for studying the retinal anatomy, as well as to detect and manage retinal diseases. In addition to studying the pure mechanical structure of the healthy and abnormal eyes, there are a number of other applications that can benefit from this technology. For example, in the application of the prosthetic retina using electrode stimulation, it is important to track the elasticity changes before and after stimulation, which can be done using the ARF-OCE technology. In this initial paper, we have demonstrated the elasticity mapping of different layers in the posterior full thickness of the eye of *in-vivo* rabbit models. The stiffness of the layers increases gradually from the ganglion side to the photoreceptor sides of the retina. In addition, we have also created a customized rabbit model primarily using blue light exposure to induce damage on the retina. Inflammation in the central retina was observed and changes in the elastic trend were speculated to be caused by the pathology. This study verifies the feasibility of using ARF-OCE to provide quantified elasticity maps of the retina, and is a critical stepping stone to the clinical translation of such a technology.

CHAPTER 7

Intravascular Elastography Using ARFI-OCE

In this chapter, we report the development of an intravascular ARFI-OCE system that uses an integrated miniature ultrasound and OCT probe to map the relative elasticity of vascular tissues. We demonstrate the capability of the miniature probe to map the biomechanical properties in phantom and human cadaver carotid arteries. The significance of intravascular OCE is introduced in section 7.1. In section 7.2, we discuss the design of the imaging system including the probe fabrication process. In sections 7.3 and 7.4, the data acquisition and processing method is presented and is validated with phantom studies, respectively. A human cadaver carotid artery is imaged and analyzed in detail in section 7.3, and we end with a summary in section 7.4.

7.1 Introduction

Atherosclerosis is a major cardiovascular disease in which plaque that is composed of fat, cholesterol, calcium, and other substances, build up in the artery walls. The lumen of the artery narrows and can lead to major diseases and complications, such as strokes and heart attacks. Identifying vulnerable plaques early is essential for the management and prevention of fatal outcomes (117). Atherosclerotic plaques can occur anywhere in the major arterial vasculature, including smaller arteries such as the coronary artery that are not easily accessible (118). Due to the lack of accessibility and the small size of the sample, intravascular diagnosis methods have become a powerful tool in interventional cardiology for diagnosis and management of cardiovascular diseases.

Atherosclerosis affects the mechanical properties of vessel walls due to the changes in the wall composition and the local geometry (119). Since the biomechanical properties of fibrous and lipid plaques are different, there is a close correlation between the tissue elasticity and pathology. Most intravascular OCE methods focus on *ex vivo* image acquisition due to the limited size of the artery and system stability. Taking the tissue out of its natural environment will affect its mechanical properties and have limited clinical value. In order to obtain accurate characterization of elastic properties, it is necessary to perform imaging *in vivo*, which requires incorporating the technique into a single miniature probe. Development of ARF-OCE with a miniature probe poses some challenges due to the need for high sensitivity and a large excitation force.

In this chapter, we introduce a novel miniature probe-based system using a single ARF as the excitation mechanism and phase-resolved OCE for detection in order to map the elasticity of tissues. We use a miniature focused ring transducer for maximum excitation and utilize OCE for its nanometer sensitivity (115, 120-122). Calibration data was obtained using two uniform phantoms while the feasibility of distinguishing mechanical contrast and tissue imaging was demonstrated using a side-by-side phantom and cadaver tissues, respectively. The relative Young’s moduli ratio of the cadaver tissue components were approximated and compared to literature values (123). The results demonstrate the feasibility of a miniature probe for the quantification of tissue mechanical properties, and represent a significant first step toward developing an endoscopic intravascular probe for ARF-OCE.

7.2 Intravascular probe-based system design

The overall design of the ARFI-OCE system is shown in Figure 7.1a. Similar to the setup in previous chapters, an 890 nm SLD source with a bandwidth of 150 nm is used in the SD-OCT system. With a 0.9 mW output power on the sample, the system operates below the preset MPE limits. On the detection arm, a 1200 slits/mm diffraction grating is used along with a CMOS camera for detection of 20 k A-lines per second. The ultrasonic excitation was synchronized with the OCE acquisition via a function generator for efficient detection. A single amplified ARFI was given for the specified pulse duration and 500 A-lines of Doppler OCT were used to detect the phantom or tissue response.

The front-facing miniature probe design is shown in Figure 7.1b. A 3.5 mm 8.8 MHz ring ultrasound transducer with a middle aperture of approximately 1 mm with a focal depth of 5.53 mm was used. The optical components include HP-780 optical fiber and 0.7 mm in diameter GRIN lens. First, the single mode optical fiber is cleaved at 8 degrees using an angled fiber cleaver. Next, the GRIN lens is fixed to the fiber with UV glue. The focal distance of the fiber is kept at 5-6 mm by controlling for the distance between the lens and fiber end. A 0.8 mm in diameter polyimide tube is fastened over the lens-fiber complex for protection, and the entire unit is put through the aperture of the transducer. The surface of the transducer and lens are aligned flush so that excitation and detection are exactly confocal, yielding in maximum tissue response signal. The optical fiber is well protected inside a stainless steel torque coil housing and connects the imaging probe to the system via a FC/APC optical connector. One end of the fiber is connected to the GRIN lens for imaging, while the other end is connected to an FC/APC connector and attached to the system for light transmission.

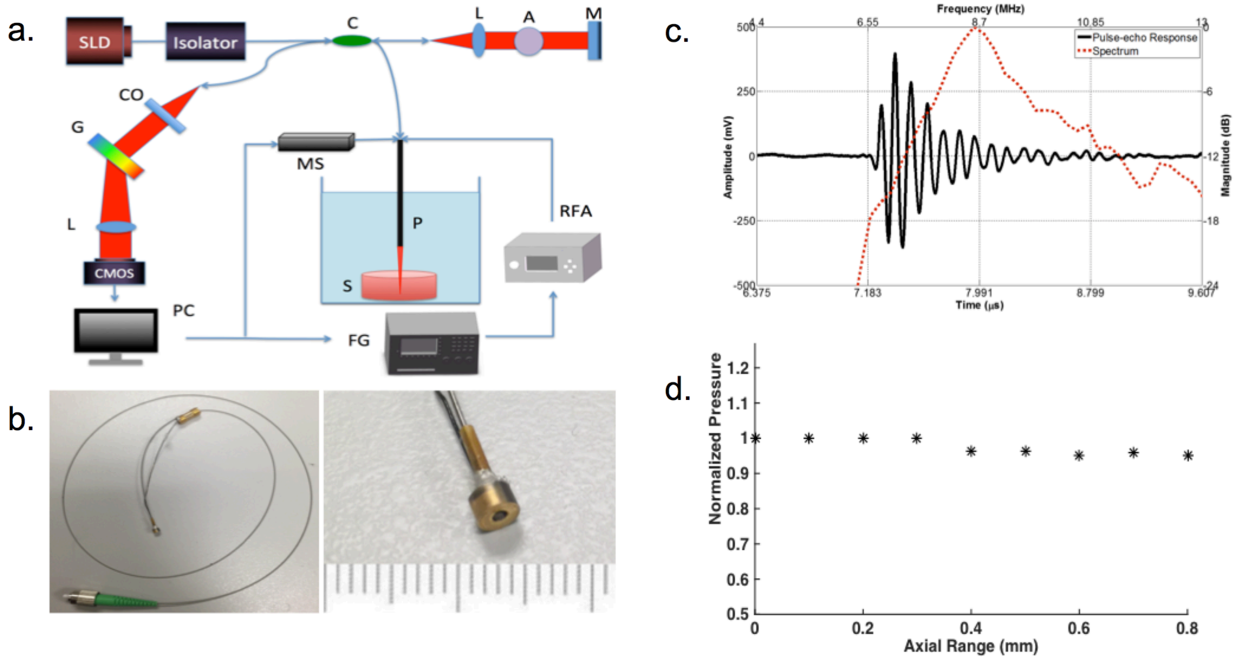

Figure 7.1 a) Overview of ARFI OCE system set up. C: collimator, L: lens, A: attenuator, M: mirror, G: grating, MS: mechanical stage, RFA: radio frequency amplifier, P: probe, S: sample, FG: function generator. b) Probe design (left). probe head including a ring transducer and optical elements inside (right). c) Transducer frequency and echo characterization. (d.) Transducer axial force field characterization.

The transducer characterization data including the pulse-echo response and the spectrum is shown in Figure 7.1c. The electrical wire of the transducer connects to the FG and RFA for synchronization and driving ARF transducer. The tip of the probe was fixed to be stiff with glue and it was then fastened to a metal rod on the mechanical stage for stability and translational movement. The tip of the probe was submerged in a water bath to provide a medium for ultrasound during imaging. The mechanical stage movement was also synchronized with the ARFI excitation and Doppler OCT detection for scanning a B-scan. For calibration studies, only

M-mode was used to capture the displacement response and the mechanical stage was not used for lateral scanning. The axial pressure field of the transducer is characterized in Figure 7.1d. For this study, the sample placement was kept within 0.8 mm of the axial focal depth, where the excitation pressure is approximately uniform within a -0.415 dB range. Therefore, the displacement amplitude can be directly compared.

7.3 Data acquisition and processing

Sample OCE raw images obtained from uniform gelatin phantoms are shown below. The left image in Figure 7.2a, which shows the phase bands with a strong initial compression response and weaker relaxation response, was obtained using 70 V ARF excitation for the duration of 1 ms on a 12.7 kPa gelatin phantom. The middle image utilizes the same duration, but with a higher voltage of 80 V, and it is apparent that there is a difference in the phase bands, with the color changing from green to teal. In the right image, the pulse duration of the ARF is increased to 2.5 ms, and the phase bands for both the compression and relaxation become wider by approximately 2.5 fold.

In order to process and quantify the phase and displacement information, the phase Doppler equation 2.10 is used. The change in displacement is calculated from the integral of the velocity. Using the concepts of the Doppler effect, the velocity can be obtained by calculating the change in phase information. Because the probe is very small and imaging takes place in a water bath, there is a need to eliminate the bulk motion in displacement caused by water movement and large-scale vibrations. Since the frequency of the noise is relatively low compared to that of the tissue response to the ARF, it is possible to use a polynomial regression fit to filter out the low frequency motions ([124]). A 10^{th} order polynomial fit was used, based on least-squares regression analysis. This low frequency noise component was subtracted from the full signal so that only useful signal remained. The filter was applied on all displacement data to eliminate bulk motion.

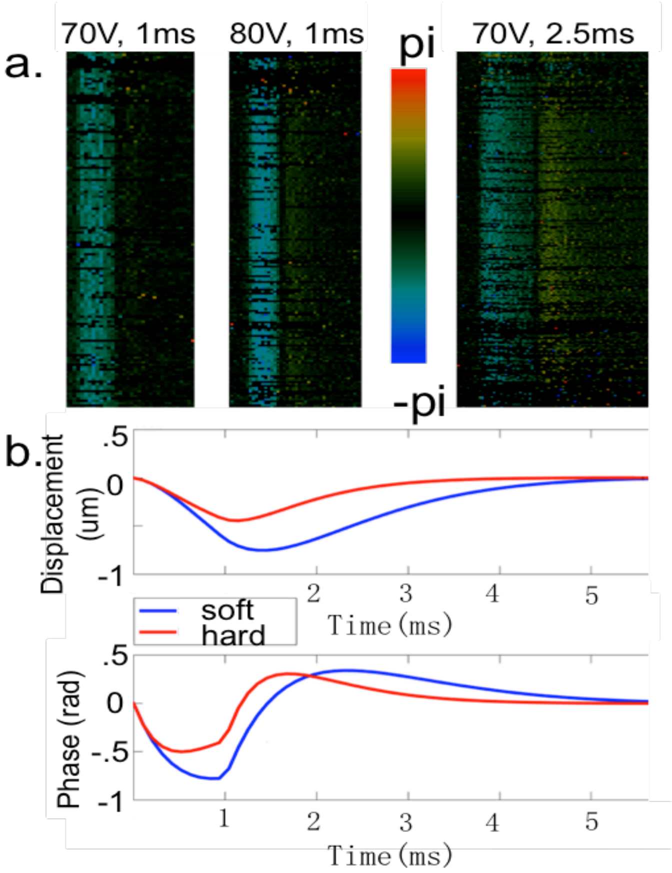

Figure 7.2 Displacement data. a) Raw phase Doppler data of phantom response. b) Displacement and phase analysis of response of 70V, 1ms excitation.

In Figure 7.2b, the response of a relatively soft and a relatively stiff gelatin phantom were obtained using a 70 V and 1 ms excitation ARF and both the phase and integrated displacement data are plotted. From the displacement image, it is apparent that the softer phantom displaced more than the stiffer phantom in general. For this particular data point, the maximum displacement of the soft phantom was 0.75 um while that of the stiff phantom was 0.45 um. The relaxation time for the soft phantom was also much longer than that of the stiff one, as expected. The phase plot shows the velocity of the soft phantom to be higher than that of the stiff one during the entire period.

7.4 Phantom validations

Two gelatin phantoms with different stiffness were fabricated. The relatively soft phantom was composed for 2.45% (by weight) gelatin, 0.4% (by volume) intralipid, and 1.8% (by weight) silicon dioxide. The stiffer phantom composed of 6% (by weight) gelatin. Intralipid was added for optical contrast while silicon dioxide was for acoustic attenuation. The uniform phantoms are circular with a diameter of 5 cm and thickness of 5 mm. A side-by-side phantom was also fabricated by cutting out a portion of the stiff phantom and adding the gelatin mixture of the soft phantom to the opening. The thickness of the side-by-side phantom was approximately 8 mm. There was some diffusion that occurred between the barriers of the two phantoms, which contributed to a gradient in elasticity.

Imaging was performed using the 2 uniform gelatin phantoms. In Figure 7.3a, various after-amplification voltages ranging from 50 V to 90 V were used on both phantoms and the displacement values were measured and averaged across 50 points. Bulk motion was once again removed. The relationship between the voltage and displacement is known to be quadratic, which is reflected in the regression fit in Figure 7.3a. The soft phantom exhibited approximately 2 times the displacement value of the stiff one at each excitation voltage. Mechanical compression tests were performed on the 2 uniform gelatin phantoms using a MTS Synergie 100. A strain of up to 0.1 mm/mm was used, with a strain rate of 50 mm/min. The thickness of the tissue was approximately 1 cm, and 50% compression was used. In most cases, deterioration was seen at around 50%. The Young’s modulus of the soft phantom was 11.7 kPa while the Young’s modulus of the stiff phantom was 23.1 kPa. These results are in general agreement with the experimental data shown in Figure 7.3a.

Data was also obtained for different excitation pulse widths. The soft gelatin phantom was used with pulse widths ranging from 0.4 to 2.5 ms. There is again an approximately linear relationship between the pulse duration and the observed displacement as expected in Figure 7.3b.

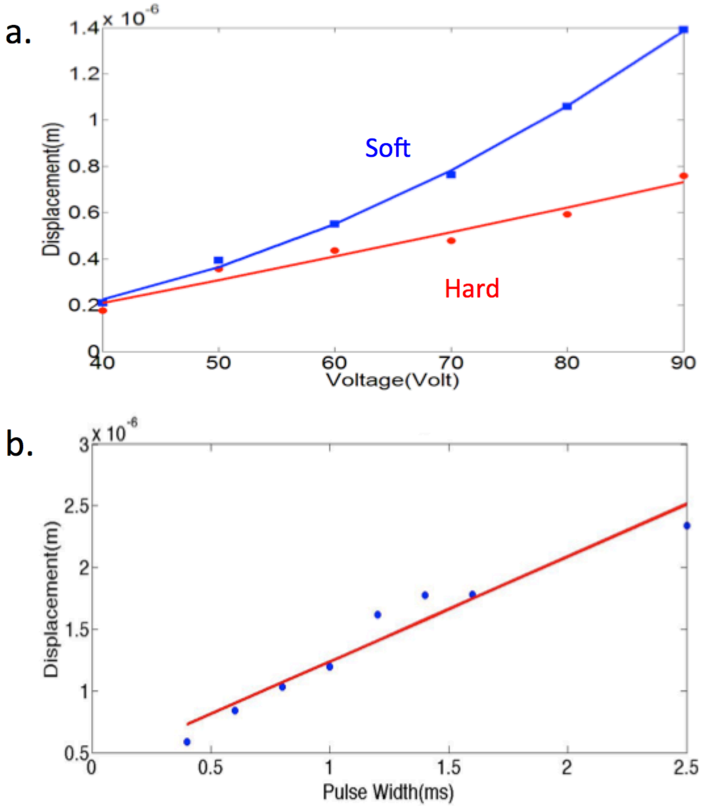

Figure 7.3 Phantom data. a) Voltage versus displacement for relatively soft and stiff uniform gelatin phantoms. b) Pulse width versus displacement for soft gelatin phantom.

For the lateral scanning experiments, an excitation voltage of 70 V and a pulse width of 1 ms was used. Since the Young's modulus for the soft and stiff phantoms were determined to be 11.7 kPa and 23.1 kPa respectively, corresponding to a soft to stiff elastic ratio to approximately 1:1.97. Since displacement and Young's modulus is inversely proportional according to equation 2.11, this displacement of the soft to stiff phantom is expected to be 1.97:1, which is approximately the ratio denoted in Figure 7.3a.

Next, in order to validate the feasibility of lateral scanning using a mechanical stage without excess noise, a side-by-side gelatin phantom was used in a 5 cm diameter petri dish with a height of 1 cm, and placed upright at the bottom of the water bath for imaging. The mechanical stage was synchronized with a step size of 20 μm, traveling one step every second. At each step, a 70 V and 1 ms excitation pulse was given, and 500 A-lines were recorded to capture the sample response. The structural OCT image is shown in Figure 7.4a. The 2-sided phantom appears uneven within the ultrasound focal region, with the right surface at a lower position than the left side due to a few different factors, including initial fabrication artifact, diffusion, and evaporation of the phantom between its construction and the time of imaging. This effect has been noted and so mechanical testing was performed immediately after imaging to minimize any changes in the elasticity over time. The OCT image shows a relatively uniform structure throughout. In Figure 7.4b, the elastogram of the same phantom is shown, and it is apparent that the right hand side shows higher displacement than the left side. Figure 7.4c draws out the average displacement curve by using segmentation to isolate the entire signal region in Figure 7.4b and taking the mean along the entire depth. The left side has mean value of 0.75 μm while the right side has a mean of 1.13 μm. The displacement values are larger than that of the homogeneous phantoms since the thickness of the side-by-side phantom was larger, at 8 mm. There is a gradual gradient change in the middle region where the two phantom likely diffused and mixed with each other.

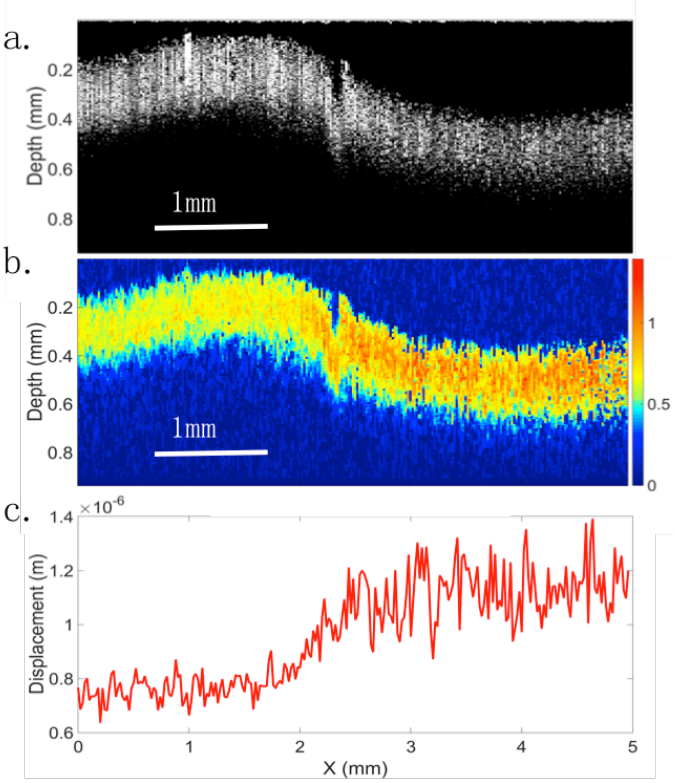

Figure 7.4 Side by side phantom. 1) OCT structural image. b) OCE elastogram. c) Average displacement map

7.5 Elasticity mapping of human cadaver carotid artery

Fresh human carotid artery samples were obtained from volunteer subjects and frozen in a -19 degree freezer. After the imaging system was set up, the tissue was thawed and a 1 cm section of the tissue was isolated and cut open longitudinally. The tissue was pinned down to a holder and submerged in phosphate buffered saline for imaging to minimize swelling. After imaging was completed, the region of interest was marked with pins and the tissue was fixed in formalin for

24 hours. Then it was processed and embedded in wax. Sectioning was performed using a Microtome to obtain 6um thick slices on a region of interest of 1mm. Finally, H&E staining was performed and images were taken with a microscope with 4x magnification to find a match with the experimental region of interest.

The carotid artery of the human cadaver was used to test the system response in tissue, specifically in plaque regions. The images were taken with similar parameters as that of the side-by-side phantom, at 20 Hz A-line rate in M-mode, with 1 s per movement step on the mechanical stage. A post-amplified voltage of 70 V and pulse duration of 1ms was used. The OCT image is shown in Figure 7.5a, where it is difficult to distinguish the plaque tissue from just the structural data. There seems to be a structural change on the left hand side of the image that may correspond to a plaque. However, the right hand side looks to be relatively uniform and smooth.

From the OCE elastogram shown in Figure 7.5b, it is apparent that the displacement on the left hand side is much smaller than the right hand side, suggesting plaque formation there. More interestingly, within the middle bulging section, there are distinct layers on the tissue. The dark blue region is much stiffer, suggesting that there may be a fibrous plaque layer there. The right hand side of the image shows higher displacement and signals toward relatively healthy tissue.

In order to validate the feasibility of our system in discerning abnormalities in tissue, histology was performed on the matching tissue using H&E staining shown in Figure 7.5c. A research pathologist was consulted in reading the histological slide. There is relative preservation of the smooth muscle layers in the media of the artery on the right hand portion, shown by the black arrow. However, there is obvious intimal thickening and atheroma on the lumen side, indicated by the blue arrow, which correspond to the low displacement region in the middle of Figure 7.5b. Within the 300 um tissue penetration that was imaged, the intimal thickening was fully captured, shown by the yellow layer. On the left hand side, there is a thicker atherosclerotic plaque, for which the vacuoles can be visualized, and this can be correlated to the lower displacement on the left side than the right side. Based on the morphology, these indications are consistent with atherosclerotic plaques. This demonstrates that the mechanical elasticity seen in our elastogram matches well with tissue pathology. It is also important to note that the system has the capabilities to differentiate both lateral and axial contrast within arterial tissue. A gradient can be seen from the left side where it is stiffer to the right side where the healthier tissue is soft. This can potentially allow us to diagnose the severity of stiffening and disease progression.

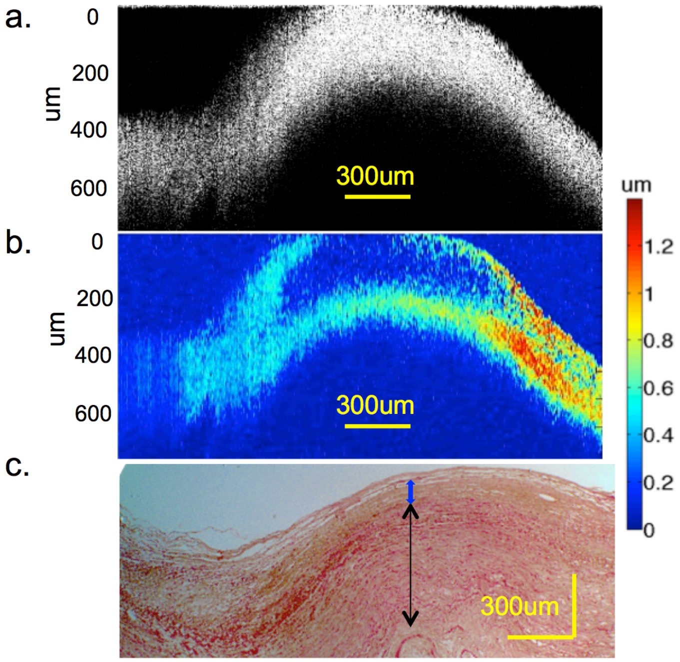

Figure 7.5 Cadaver tissue & histology data. a) OCT image of human cadaver coronary artery cross-section. b) OCE elastogram of corresponding region. c) H&E staining of the region under 4x magnification. Red box corresponds to region of stiff inclusion.

Using the calibration data for the ARF stress value, we can approximate the relative Young's moduli of the healthy versus diseased region. In Figure 7.5 above, the far right side consists of mostly healthy tissue and early atheroma, and the average displacement is estimated to be 0.97±0.2 um. The left side, consisting of abnormal tissue, has a displacement of 0.19±0.04 um. This corresponds to a stiffness ratio of 1:5.1 for the right to left sides. According to this value and comparison to literature (123), the diseased region is most likely composed of fibrous plaque, which has been verified with histology as well.

All methods were carried out in accordance with the University of California, Irvine Institutional Review Board (IRB) and the Institutional Biosafety Committee. IRB granted an exemption to the protocol requirement since the activities do not constitute Human Subject Research. Informed consent was deemed unnecessary because confidentiality of the deceased cadaver tissues is protected and coded. All experimental protocols were approved by the UCI IBC under protocol #2016-1570.

7.6 Summary

In conclusion, we have introduced an ARFI-OCE technique that uses a front-facing miniature probe with a ring transducer to generate elastograms of tissue with high mechanical sensitivity. Phantom data was collected using two uniform phantoms with different stiffness. Lateral scanning was performed using a side-by-side gelatin phantom and observed the appropriate mechanical contrast. Finally, imaging was performed on a human cadaver carotid artery sample and tissue abnormality was detected and matched to histology results. The relative Young's moduli of the tissue were approximated based on the relative displacement information. These results represent a prototype device that can identify plaque regions effectively and serves as an important step to the miniaturization and translation of this technology for *in vivo* imaging.

CHAPTER 8

Summary and Future Directions

8.1 Summary

This Ph.D. dissertation has presented a method of quantified elasticity mapping for the *in vivo* diagnosis of ocular diseases and cardiovascular applications using ARF-OCE. We also discuss the translation of such technology to clinical imaging. The experimental research and the theoretical approach have been discussed in detail.

A phase-resolved ARF-OCE method using confocal excitation and detection was optimized for measuring tissue elasticity and rendering elasticity maps. The system has been optimized in resolution, synchronization, imaging range, and the implementation of a new setup to accommodate *in vivo* imaging. In this system, an ultrasound transducer emits ARF to induce tissue vibrations and the resulting displacement is measured using Doppler OCT. The advantages are high resolution due to optical detection, high sensitivity due to the phase stability of Doppler OCT, and fast imaging speed. In previous experiments, only qualitative elasticity measurements were possible due to the difficulty in quantifying the stress induced by ARF on tissue. A method of quantification was created based on the resonance frequency theory and the Voigt mechanical model to calculate the elasticity of individual tissue structures. After phantom validations and calibrations, this technique was applied to ocular and cardiovascular applications in the early stage diagnosis of diseases. From a clinical standpoint, this technology uses non-invasive, non-ionizing light interactions, and is translatable to become a powerful tool in clinical diagnosis and therapeutic monitoring.

In ocular diseases such as keratoconus and AMD, the elasticity of the tissue begins to change before structural changes are visible with current imaging modalities. With ARF-OCE, the degree of corneal crosslinking can be measured and the relative elasticity map has been generated to show spatial changes. The layered elasticity change of the retina has also been mapped in both *ex vivo* and *in vivo* settings to visualize the differences in elasticity between retinal layers and the changes in mechanical properties associated with pathological changes such as inflammation. The resonance frequency sweep was also applied on both the anterior and posterior eye, where the frequency response directly related to the stiffness of the material. The feasibility for the translation to *in vivo* elasticity mapping has been proven, which is a stepping stone to clinical diagnosis.

In cardiovascular applications, a novel miniature ARF-OCE probe has been fabricated for intravscaular imaging. The spatial elasticity mapping has been obtained for validation phantoms and the carotid artery, and the mechanical changes for pathological plaques could be identified. In addition, the plaque components could also be distinguished based on the elasticity analysis. Since intravascular US and OCT are both commercialized and widely used in the clinics today, the translation of the ARF-OCE technology is imminent. It will offer physicians an additional property to aid in the diagnosis and monitoring of vulnerable plaques.

8.2 Future directions: Retinal electrode stimulation

In addition to measuring the retinal layered elasticity change during disease onset, ARF-OCE can also be applied to elasticity tracking before and after ocular procedures to assess the retinal damage. One application is determining the change in retinal stiffness before and after the application of a retinal prosthesis. Current retinal prosthesis method involves the placement of electrodes on the retina to stimulate the nerve fibers. When metal electrodes are introduced onto a soft tissue surface, it may inadvertently change the tissue properties and induce damage onto the tissue. It is important to study the changes and harmful effects that take place with the electrode placement to better understand the effectiveness of such a procedure.

We have also conducted a few preliminary experiments by placing electrodes onto an ex-vivo porcine retina. Vitrectomy was performed to cleanly remove the vitreous, and a small surgical tack was used to hold the electrode in place. Due to the *ex-vivo* nature of the tissue and the lack of blood perfusion, retinal detachment was observed at some portions in Figure 8.1a. We have verified that the OCT light cannot penetrate through the metal electrode, but can go through the polyimide portions adjacent to it. Figure 8.1b shows the *en face* view of the retina, where the metal electrode portions show up with no optical signal, and the polyimide portions can be visualized underneath. The region directly underneath the polyimide can be quantified by directly measuring the tissue response using ARF-OCE.

To verify the feasibility of elasticity mapping underneath the polyimide material, Figures 8.1c and 8.1d zoom into a smaller region within the ultrasonic lateral focus. The OCT image is shown along with the displacement map, where the ganglion side of the retina seems to vibrate less, or is stiffer, than the deeper portions. This is likely due to the stiff electrode/polyimide unit that is directly on top of the retina. In addition, the resonance frequency method was used to measure the bulk modulus of the retina plus electrode unit, which was approximately 180 kPa.

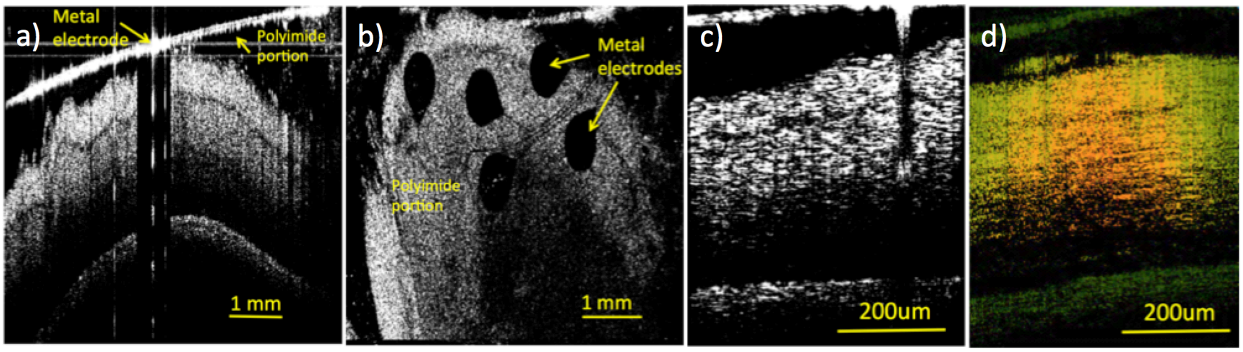

Figure 8.1. Preliminary results with electrode placement on retina. a) OCT B-scan of region under electrode and polyimide unit. b) En-face OCT of retina through the electrode/polyimide unit. c) OCT zoomed in portion of region under polyimide. d) OCE of region under polyimide.

The primary challenge is that the ARF currently exceeds the federal safety limit for ocular ultrasound exposure by approximately 10 fold. However, the theoretical phase sensitivity of the ARF-OCE system is on the nanometer scale, while we are currently inducing micrometer displacement. Therefore, further experiments need to be performed to determine the optimal ARF level where the trade-off between sensitivity and power is balanced.

These results demonstrate that it is feasible to use compressional elastography to determine the stiffness of the retina before and after electrode placement. The plan for the next step is to add electrode stimulation in both *ex-vivo* and *in-vivo* animal models, and measure the changes in retinal elasticity to better understand the impact of retinal prosthesis. The experiments conducted thus far serve as stepping stones to clinical imaging of the retina both with and without prosthesis.

8.3 Future directions: In vivo intravascular ARF-OCE

ARF-OCE provides physicians with a tool to measure the mechanical elasticity of vascular tissues and differentiate plaque components. However, structural information is still necessary to visualize the plaque contour, especially to aid in the identification of the fibrous cap and lipid pool with high resolution. OCT and US have proven to be perfectly complimentary in vascular imaging of vulnerable plaques, where OCT provides the high resolution to visualize thin fibrous caps and US offers a deep penetration into the large lipid pools (125-127). Therefore, the next step is to combine the probe-based ARF-OCE technology with OCT and US to yield in a tri-modality system that can offer both mechanical properties as well as structural information.

Having validated the ARF-OCE system with phantom testing and tissue, we have started to modify the setup to incorporate ultrasound, as well as make it compatible with miniature rotating catheter probes. The schematic diagram of the tri-modality system is shown in Figure 8.2. This system combines the OCT, US, and OCE components in a single probe. The probe connects directly to a rotary joint with a motor for fast rotational scanning. An ultrasound pulser/receiver is used to detect acoustic signal for image formation. The ultrasound excitation and acquisition, OCT acquisition, as well as probe rotation are all synchronized and controlled via C++ software on the computer. The SD-OCT system and ARF generation is similar to the one presented in the previous chapter. For OCT/US, we will use a similar algorithm to the previous system (125-127).

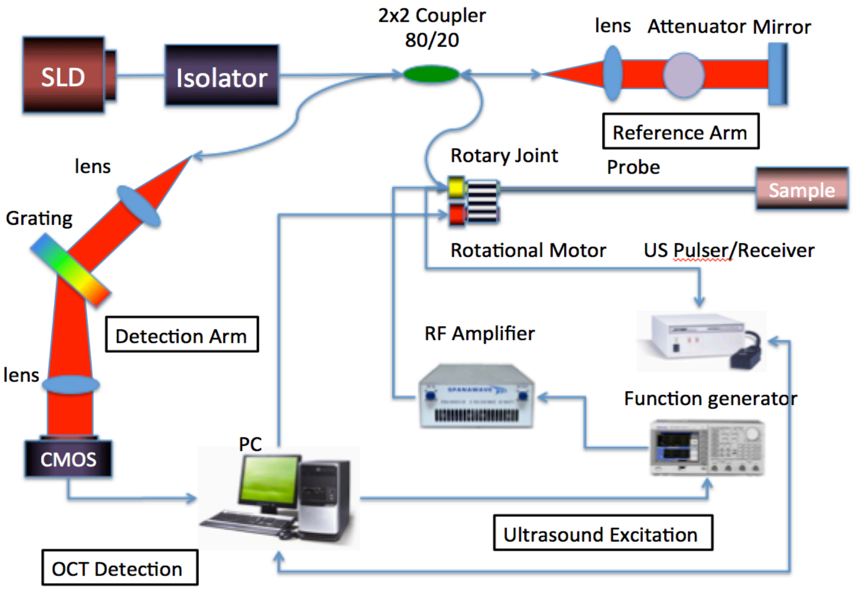

Figure 8.2 Integrated tri-modality system with ARF-OCE, OCT, and US.

The probe design will be similar to the probe presented in chapter 7, since the ultrasound transducer can both serve as the ARF excitation for OCE and the pulser/receiver for ultrasound imaging. We have been able to cut down the size of the ring ultrasound transducer from 3.5 mm to 2.5 mm, and the inner ring diameter is kept at 0.6 mm. The optical and acoustic beams will be confocal on the sample of interest. The two signals will be synchronized so that OCT, OCE, and US imaging can be performed simultaneously. The probe will be attached to a rotary joint device, which will allow for rotational scanning inside the artery. The probe design must be robust to fast rotations inside a catheter sheath. The proposed rotation mechanism uses a rotary joint with a rotating motor. This type of rotational mechanism has been previously used in US/OCT as well as OCT probes, and has proven to work well even under high scanning speeds up to 72 Hz (126).

One of the major obstacles to overcome in miniature OCE probe design is the strength of the ARF emitted by the ultrasonic transducer. Because these transducers have been scaled down from diameters of 3 cm to less than 2.5 mm, the induced ARF signal is intuitively much weaker than before. Therefore, it is necessary to test whether the transducer is able to provide a strong enough force to create displacement in the sample. Even if there is displacement signal, if a high voltage is applied from the function generator, the probability of burning and damaging the transducer is very large. Therefore, it is also necessary to test for the maximum voltage that the transducer can withstand. In addition, the impulse ARF-OCE imaging technique described in the previous chapter requires step by step A-line acquisition, which is inefficient. It would be ideal to offer continuous excitation as the probe scans across the tissue of interest, which will increase the imaging speed from 10 minutes to less than 0.3 s per frame. Again, the limitation is the amount of ARF the miniature transducer can withstand at one time.

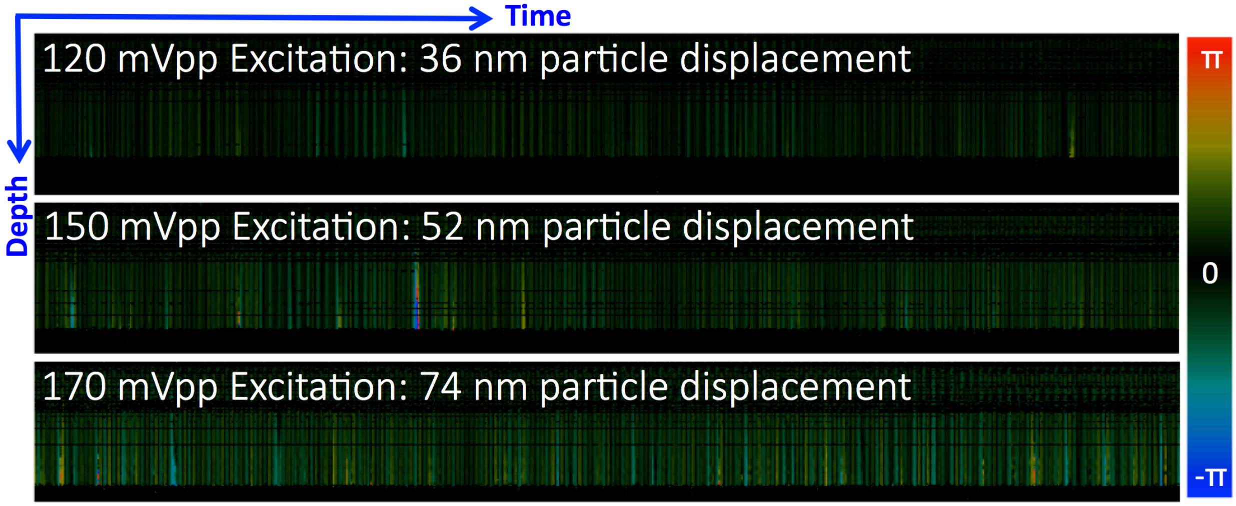

Figure 8.3. Continuous pulse ARF-OCE imaging of phantom at different excitation voltage.

Therefore, we tested the feasibility of using continuous pulse excitation using the front-facing catheter on a phantom as shown in Figure 8.3. We demonstrate that even with a 2.5 mm probe, we can generate sufficient force to induce sample vibrations and acquire the phase and displacement data. This allows for faster real-time imaging with continuous probe rotation and pull-back.

With the intravascular ARF-OCE technology, it has been able to successfully distinguish diseased from healthy tissues, especially when the OCT image alone does not show this accurately. The current goal is to implement probe rotation during acquisition, as well as to miniaturize the design further by gradually cutting down on the transducer size without sacrificing the ARF power excessively. The current catheter can be used for diagnosis in larger vessels, but the diameter is ideally less than 1 mm for imaging in the coronary arteries. While the ocular applications exceed the ultrasound exposure limit, this is not an issue with cardiovascular imaging, where the exposure limit is well above the current ARF level.

In the next step, *in vivo* experiments will be performed in the rabbit aorta and in the porcine coronary artery to evaluate the performance of the addition of ARF-OCE. Our ultimate goal is to translate the imaging system from laboratory use to clinical diagnosis. The results obtained from the animal studies will provide solid data necessary for IRB approval of future clinical testing. This project is the stepping stone to using an integrated intravascular imaging technology in clinics for early diagnosis and progress tracking of vulnerable plaques for atherosclerosis.

OCE is a valuable tool that has gained momentum in recent years for the characterization and quantification of mechanical properties of tissues. Various methods of excitation and detection have been used, including air puff and ARF for excitation, and shear wave and compressional wave for detection. All of these methods aim to quantify the elasticity of tissues with the Young's modulus as standard. It has been demonstrated that ARF-OCE has great potential to characterize the mechanical elasticity of vascular lesions in the early diagnosis of atherosclerosis. The surveillance of vulnerable plaques will provide a critically important tool for monitoring the disease progression and provide timely intervention in high-risk patients.

References

1. Bressler NM, Bressler SB, Fine SL. Age-related macular degeneration. Survey of Ophthalmology. 1988;32(6):375-413. doi: https://doi.org/10.1016/0039-6257(88)90052-5.
2. Jager RD, Mieler WF, Miller JW. Age-related macular degeneration. New England Journal of Medicine. 2008;358(24):2606-17.
3. Alamouti B, Funk J. Retinal thickness decreases with age: an OCT study. British journal of ophthalmology. 2003;87(7):899-901.
4. Ayoub T, Patel N. Age-related macular degeneration. Journal of the Royal Society of Medicine. 2009;102(2):56-61.
5. Wong T, Chakravarthy U, Klein R, Mitchell P, Zlateva G, Buggage R, Fahrbach K, Probst C, Sledge I. The natural history and prognosis of neovascular age-related macular degeneration: a systematic review of the literature and meta-analysis. Ophthalmology. 2008;115(1):116-26. e1.
6. Group A-REDSR. The Age-Related Eye Disease Study system for classifying age-related macular degeneration from stereoscopic color fundus photographs: the Age-Related Eye Disease Study Report Number 6. American journal of ophthalmology. 2001;132(5):668-81.
7. Kaiser PK, Blodi BA, Shapiro H, Acharya NR. Angiographic and optical coherence tomographic results of the MARINA study of ranibizumab in neovascular age-related macular degeneration. Ophthalmology. 2007;114(10):1868-75. e4.
8. Huang D, Swanson EA, Lin CP, Schuman JS, Stinson WG, Chang W, Hee MR, Flotte T, Gregory K, Puliafito CA. Optical coherence tomography. science. 1991;254(5035):1178-81.
9. Krishnan L, Hoying JB, Nguyen H, Song H, Weiss JA. Interaction of angiogenic microvessels with the extracellular matrix. American Journal of Physiology-Heart and Circulatory Physiology. 2007;293(6):H3650-H8.
10. Chen K, Rowley AP, Weiland JD. Elastic properties of porcine ocular posterior soft tissues. Journal of Biomedical Materials Research Part A. 2010;93(2):634-45.
11. Friberg TR, Lace JW. A comparison of the elastic properties of human choroid and sclera. Experimental eye research. 1988;47(3):429-36.
12. Jones I, Warner M, Stevens J. Mathematical modelling of the elastic properties of retina: a determination of Young's modulus. Eye. 1992;6(6):556.
13. Mozaffarian D, Benjamin EJ, Go AS, Arnett DK, Blaha MJ, Cushman M, Das SR, de Ferranti S, Després J-P, Fullerton HJ. Heart disease and stroke statistics—2016 update: a report from the American Heart Association. Circulation. 2016;133(4):e38-e360.
14. Mozaffarian D, Benjamin EJ, Go AS, Arnett DK, Blaha MJ, Cushman M, Das SR, De Ferranti S, Després J-P, Fullerton HJ. Executive summary: heart disease and stroke statistics—2016 update: a report from the American Heart Association. Circulation. 2016;133(4):447-54.
15. Ross R. Atherosclerosis—an inflammatory disease. New England journal of medicine. 1999;340(2):115-26.
16. Hansson GK. Inflammation, atherosclerosis, and coronary artery disease. New England Journal of Medicine. 2005;352(16):1685-95.

17. Virmani R, Burke AP, Kolodgie FD, Farb A. Pathology of the Thin-Cap Fibroatheroma. Journal of interventional cardiology. 2003;16(3):267-72.
18. Cheruvu PK, Finn AV, Gardner C, Caplan J, Goldstein J, Stone GW, Virmani R, Muller JE. Frequency and distribution of thin-cap fibroatheroma and ruptured plaques in human coronary arteries: a pathologic study. Journal of the American College of Cardiology. 2007;50(10):940-9.
19. Amirbekian V, Lipinski MJ, Briley-Saebo KC, Amirbekian S, Aguinaldo JGS, Weinreb DB, Vucic E, Frias JC, Hyafil F, Mani V. Detecting and assessing macrophages in vivo to evaluate atherosclerosis noninvasively using molecular MRI. Proceedings of the National Academy of Sciences. 2007;104(3):961-6.
20. Waxman S, Ishibashi F, Muller JE. Detection and treatment of vulnerable plaques and vulnerable patients: novel approaches to prevention of coronary events. Circulation. 2006;114(22):2390-411.
21. Little WC, Constantinescu M, Applegate RJ, Kutcher MA, Burrows MT, Kahl FR, Santamore WP. Can coronary angiography predict the site of a subsequent myocardial infarction in patients with mild-to-moderate coronary artery disease? Circulation. 1988;78(5):1157-66.
22. Sherman CT, Litvack F, Grundfest W, Lee M, Hickey A, Chaux A, Kass R, Blanche C, Matloff J, Morgenstern L. Coronary angioscopy in patients with unstable angina pectoris. New England Journal of Medicine. 1986;315(15):913-9.
23. Takano M, Mizuno K, Okamatsu K, Yokoyama S, Ohba T, Sakai S. Mechanical and structural characteristics of vulnerable plaques: analysis by coronary angioscopy and intravascular ultrasound. Journal of the American College of Cardiology. 2001;38(1):99-104.
24. LaMuraglia GM, Southern JF, Fuster V, Kantor HL. Magnetic resonance images lipid, fibrous, calcified, hemorrhagic, and thrombotic components of human atherosclerosis in vivo. Circulation. 1996;94(5):932-8.
25. Ebenstein DM, Coughlin D, Chapman J, Li C, Pruitt LA. Nanomechanical properties of calcification, fibrous tissue, and hematoma from atherosclerotic plaques. Journal of biomedical materials research Part A. 2009;91(4):1028-37.
26. Inagaki J, Hasegawa H, Kanai H, Ichiki M, Tezuka F. Tissue classification of arterial wall based on elasticity image. Japanese journal of applied physics. 2006;45(5S):4732.
27. Baldewsing RA, Mastik F, Schaar JA, Serruys PW, van Der Steen AF. Robustness of reconstructing the Young's modulus distribution of vulnerable atherosclerotic plaques using a parametric plaque model. Ultrasound in Medicine and Biology. 2005;31(12):1631-45.
28. Loree HM, Tobias BJ, Gibson LJ, Kamm RD, Small DM, Lee RT. Mechanical properties of model atherosclerotic lesion lipid pools. Arteriosclerosis, Thrombosis, and Vascular Biology. 1994;14(2):230-4.
29. Chai C-K, Speelman L, Oomens CW, Baaijens FP. Compressive mechanical properties of atherosclerotic plaques—Indentation test to characterise the local anisotropic behaviour. Journal of biomechanics. 2014;47(4):784-92.
30. Walsh M, Cunnane E, Mulvihill J, Akyildiz A, Gijsen F, Holzapfel GA. Uniaxial tensile testing approaches for characterisation of atherosclerotic plaques. Journal of biomechanics. 2014;47(4):793-804.

31. Baldewsing RA, Schaar JA, Mastik F, van der Steen AF. Local elasticity imaging of vulnerable atherosclerotic coronary plaques. Atherosclerosis, Large Arteries and Cardiovascular Risk: Karger Publishers; 2007. p. 35-61.
32. Schaar JA, De Korte CL, Mastik F, Strijder C, Pasterkamp G, Boersma E, Serruys PW, Van Der Steen AF. Characterizing vulnerable plaque features with intravascular elastography. Circulation. 2003;108(21):2636-41.
33. Ophir J, Cespedes I, Ponnekanti H, Yazdi Y, Li X. Elastography: a quantitative method for imaging the elasticity of biological tissues. Ultrasonic imaging. 1991;13(2):111-34.
34. Sun C, Standish BA, Yang VX. Optical coherence elastography: current status and future applications. Journal of biomedical optics. 2011;16(4):043001.
35. Manduca A, Oliphant TE, Dresner M, Mahowald J, Kruse SA, Amromin E, Felmlee JP, Greenleaf JF, Ehman RL. Magnetic resonance elastography: non-invasive mapping of tissue elasticity. Medical image analysis. 2001;5(4):237-54.
36. Greenleaf JF, Fatemi M, Insana M. Selected methods for imaging elastic properties of biological tissues. Annual review of biomedical engineering. 2003;5(1):57-78.
37. Khalil AS, Chan RC, Chau AH, Bouma BE, Mofrad MRK. Tissue elasticity estimation with optical coherence elastography: toward mechanical characterization of in vivo soft tissue. Annals of biomedical engineering. 2005;33(11):1631-9.
38. Wang RK, Kirkpatrick S, Hinds M. Phase-sensitive optical coherence elastography for mapping tissue microstrains in real time. Applied Physics Letters. 2007;90(16):164105.
39. Wang RK, Ma Z, Kirkpatrick SJ. Tissue Doppler optical coherence elastography for real time strain rate and strain mapping of soft tissue. Applied Physics Letters. 2006;89(14):144103.
40. Kennedy BF, Kennedy KM, Oldenburg AL, Adie SG, Boppart SA, Sampson DD. Optical coherence elastography. Optical Coherence Tomography: Technology and Applications. 2015:1007-54.
41. Liang X, Adie SG, John R, Boppart SA. Dynamic spectral-domain optical coherence elastography for tissue characterization. Optics express. 2010;18(13):14183-90.
42. Manapuram RK, Aglyamov SR, Monediado FM, Mashiatulla M, Li J, Emelianov SY, Larin KV. In vivo estimation of elastic wave parameters using phase-stabilized swept source optical coherence elastography. Journal of biomedical optics. 2012;17(10):100501.
43. Rogowska J, Patel N, Fujimoto J, Brezinski M. Optical coherence tomographic elastography technique for measuring deformation and strain of atherosclerotic tissues. Heart. 2004;90(5):556-62.
44. van Soest G, Mastik F, de Jong N, van der Steen AF. Robust intravascular optical coherence elastography by line correlations. Physics in Medicine & Biology. 2007;52(9):2445.
45. Wang S, Larin KV. Optical coherence elastography for tissue characterization: a review. Journal of biophotonics. 2015;8(4):279-302.
46. Sinkus R, Tanter M, Catheline S, Lorenzen J, Kuhl C, Sondermann E, Fink M. Imaging anisotropic and viscous properties of breast tissue by magnetic resonance-elastography. Magnetic resonance in medicine. 2005;53(2):372-87.
47. Sinkus R, Tanter M, Xydeas T, Catheline S, Bercoff J, Fink M. Viscoelastic shear properties of in vivo breast lesions measured by MR elastography. Magnetic resonance imaging. 2005;23(2):159-65.

48. Catheline S, Gennisson J-L, Delon G, Fink M, Sinkus R, Abouelkaram S, Culioli J. Measurement of viscoelastic properties of homogeneous soft solid using transient elastography: An inverse problem approach. The Journal of the Acoustical Society of America. 2004;116(6):3734-41.
49. Nightingale K, McAleavey S, Trahey G. Shear-wave generation using acoustic radiation force: in vivo and ex vivo results. Ultrasound in Medicine and Biology. 2003;29(12):1715-23.
50. Evans A, Whelehan P, Thomson K, McLean D, Brauer K, Purdie C, Jordan L, Baker L, Thompson A. Quantitative shear wave ultrasound elastography: initial experience in solid breast masses. Breast cancer research. 2010;12(6):R104.
51. O'Donnell M, Skovoroda AR, Shapo BM, Emelianov SY. Internal displacement and strain imaging using ultrasonic speckle tracking. IEEE transactions on ultrasonics, ferroelectrics, and frequency control. 1994;41(3):314-25.
52. Ahmad A, Huang P-C, Sobh NA, Pande P, Kim J, Boppart SA. Mechanical contrast in spectroscopic magnetomotive optical coherence elastography. Physics in Medicine & Biology. 2015;60(17):6655.
53. Liang X, Oldenburg AL, Crecea V, Chaney EJ, Boppart SA. Optical micro-scale mapping of dynamic biomechanical tissue properties. Optics express. 2008;16(15):11052-65.
54. Wang S, Larin KV. Noncontact depth-resolved micro-scale optical coherence elastography of the cornea. Biomedical Optics Express. 2014;5(11):3807-21.
55. Nguyen T-M, Arnal B, Song S, Huang Z, Wang RK, O'Donnell M. Shear wave elastography using amplitude-modulated acoustic radiation force and phase-sensitive optical coherence tomography. Journal of biomedical optics. 2015;20(1):016001.
56. Liang X, Crecea V, Boppart SA. Dynamic optical coherence elastography: a review. Journal of innovative optical health sciences. 2010;3(04):221-33.
57. De Korte CL, Van Der Steen AF, Céspedes EI, Pasterkamp G. Intravascular ultrasound elastography in human arteries: initial experience in vitro. Ultrasound in Medicine and biology. 1998;24(3):401-8.
58. de Korte CL, van der Steen AF, Céspedes EI, Pasterkamp G, Carlier SG, Mastik F, Schoneveld AH, Serruys PW, Bom N. Characterization of plaque components and vulnerability with intravascular ultrasound elastography. Physics in Medicine & Biology. 2000;45(6):1465.
59. Baldewsing RA, Schaar JA, Mastik F, Serruys P. Intravascular Ultrasound Elastography: A Clinician's Tool for Assessing Vulnerability and Material Composition of Plaques. Studies in health technology and informatics. 2005;113:75-96.
60. de Korte CL, Sierevogel MJ, Mastik F, Strijder C, Schaar JA, Velema E, Pasterkamp G, Serruys P, van der Steen AF. Identification of atherosclerotic plaque components with intravascular ultrasound elastography in vivo: a Yucatan pig study. Circulation. 2002;105(14):1627-30.
61. Baldewsing RA, de Korte CL, Schaar JA, Mastik F, van der Steen AF. Finite element modeling and intravascular ultrasound elastography of vulnerable plaques: parameter variation. Ultrasonics. 2004;42(1-9):723-9.
62. Baldewsing RA, de Korte CL, Schaar JA, Mastik F, van Der Steen AF. A finite element model for performing intravascular ultrasound elastography of human atherosclerotic coronary arteries. Ultrasound in Medicine and Biology. 2004;30(6):803-13.

63. Prati F, Arbustini E, Labellarte A, Dal Bello B, Sommariva L, Mallus M, Pagano A, Boccanelli A. Correlation between high frequency intravascular ultrasound and histomorphology in human coronary arteries. Heart. 2001;85(5):567-70.
64. Fujimoto JG. Optical coherence tomography. Comptes Rendus de l'Académie des Sciences-Series IV-Physics. 2001;2(8):1099-111.
65. Qi W, Chen R, Chou L, Liu G, Zhang J, Zhou Q, Chen Z. Phase-resolved acoustic radiation force optical coherence elastography. Journal of biomedical optics. 2012;17(11):110505.
66. Qi W, Li R, Ma T, Kirk Shung K, Zhou Q, Chen Z. Confocal acoustic radiation force optical coherence elastography using a ring ultrasonic transducer. Applied physics letters. 2014;104(12):123702.
67. Qu Y, Ma T, He Y, Zhu J, Dai C, Yu M, Huang S, Lu F, Shung KK, Zhou Q. Acoustic radiation force optical coherence elastography of corneal tissue. IEEE Journal of Selected Topics in Quantum Electronics. 2016;22(3):288-94.
68. Catheline S, Thomas J-L, Wu F, Fink MA. Diffraction field of a low frequency vibrator in soft tissues using transient elastography. IEEE transactions on ultrasonics, ferroelectrics, and frequency control. 1999;46(4):1013-9.
69. Gennisson JL, Cornu C, Catheline S, Fink M, Portero P. Human muscle hardness assessment during incremental isometric contraction using transient elastography. Journal of biomechanics. 2005;38(7):1543-50.
70. Schmitt JM. Optical coherence tomography (OCT): a review. IEEE Journal of Selected Topics in Quantum Electronics. 1999;5(4):1205-15.
71. Fercher AF. Optical coherence tomography. J of Biomedical Opt. 1996;1:157-73.
72. Stanga P, Bird A. Optical Coherence Tomography (OCT) principles of operations, tenchnology, indication in Vitroretinal imaging intepretation of results. Int Ophthalmol. 2001;23:9-15.
73. Moon S, Qu Y, Chen Z. Characterization of spectral-domain OCT with autocorrelation interference response for axial resolution performance. Optics Express. 2018;26(6):7253-69.
74. Qi W, Li R, Ma T, Li J, Kirk Shung K, Zhou Q, Chen Z. Resonant acoustic radiation force optical coherence elastography. Applied Physics Letters. 2013;103(10):103704.
75. Han Z, Aglyamov SR, Li J, Singh M, Wang S, Vantipalli S, Wu C, Liu C-h, Twa MD, Larin KV. Quantitative assessment of corneal viscoelasticity using optical coherence elastography and a modified Rayleigh–Lamb equation. Journal of biomedical optics. 2015;20(2):020501.
76. Kotecha A. What biomechanical properties of the cornea are relevant for the clinician? Survey of ophthalmology. 2007;52(6):S109-S14.
77. Ruberti JW, Sinha Roy A, Roberts CJ. Corneal biomechanics and biomaterials. Annual review of biomedical engineering. 2011;13:269-95.
78. Roy AS, Shetty R, Kummelil MK. Keratoconus: a biomechanical perspective on loss of corneal stiffness. Indian journal of ophthalmology. 2013;61(8):392.
79. Comaish IF, Lawless MA. Progressive post-LASIK keratectasia: biomechanical instability or chronic disease process? Journal of Cataract & Refractive Surgery. 2002;28(12):2206-13.

80. Salgado JP, Khoramnia R, Lohmann CP, von Mohrenfels CW. Corneal collagen crosslinking in post-LASIK keratectasia. British Journal of Ophthalmology. 2011;95(4):493-7.
81. Luce DA. Determining in vivo biomechanical properties of the cornea with an ocular response analyzer. Journal of Cataract & Refractive Surgery. 2005;31(1):156-62.
82. Hon Y, Lam AK. Corneal deformation measurement using Scheimpflug noncontact tonometry. Optometry and Vision Science. 2013;90(1):e1-e8.
83. Singh M, Wu C, Liu C-H, Li J, Schill A, Nair A, Larin KV. Phase-sensitive optical coherence elastography at 1.5 million A-Lines per second. Optics letters. 2015;40(11):2588-91.
84. Kennedy BF, Malheiro FG, Chin L, Sampson DD. Three-dimensional optical coherence elastography by phase-sensitive comparison of C-scans. Journal of biomedical optics. 2014;19(7):076006.
85. Wang S, Larin KV. Shear wave imaging optical coherence tomography (SWI-OCT) for ocular tissue biomechanics. Optics letters. 2014;39(1):41-4.
86. Zhu J, Qu Y, Ma T, Li R, Du Y, Huang S, Shung KK, Zhou Q, Chen Z. Imaging and characterizing shear wave and shear modulus under orthogonal acoustic radiation force excitation using OCT Doppler variance method. Optics letters. 2015;40(9):2099-102.
87. Rabinowitz YS. Keratoconus. Survey of ophthalmology. 1998;42(4):297-319.
88. Krachmer JH, Feder RS, Belin MW. Keratoconus and related noninflammatory corneal thinning disorders. Survey of ophthalmology. 1984;28(4):293-322.
89. Lim LS, Mitchell P, Seddon JM, Holz FG, Wong TY. Age-related macular degeneration. The Lancet. 2012;379(9827):1728-38.
90. Hee MR, Baumal CR, Puliafito CA, Duker JS, Reichel E, Wilkins JR, Coker JG, Schuman JS, Swanson EA, Fujimoto JG. Optical coherence tomography of age-related macular degeneration and choroidal neovascularization. Ophthalmology. 1996;103(8):1260-70.
91. Wagner H, Barr J, Zadnik K. Collaborative Longitudinal Evaluation of Keratoconus (CLEK) Study: methods and findings to date. Contact Lens and Anterior Eye. 2007;30(4):223-32.
92. Young RW. Pathophysiology of age-related macular degeneration. Survey of ophthalmology. 1987;31(5):291-306.
93. Edmund C. Corneal elasticity and ocular rigidity in normal and keratoconic eyes. Acta Ophthalmologica. 1988;66(2):134-40.
94. Nguyen T-M, Song S, Arnal B, Huang Z, O'Donnell M, Wang RK. Visualizing ultrasonically induced shear wave propagation using phase-sensitive optical coherence tomography for dynamic elastography. Optics letters. 2014;39(4):838-41.
95. Litwiller DV, Lee SJ, Kolipaka A, Mariappan YK, Glaser KJ, Pulido JS, Ehman RL. MR elastography of the ex vivo bovine globe. Journal of Magnetic Resonance Imaging. 2010;32(1):44-51.
96. Liu J, Roberts CJ. Influence of corneal biomechanical properties on intraocular pressure measurement: quantitative analysis. Journal of Cataract & Refractive Surgery. 2005;31(1):146-55.

97. Huang S, Piao Z, Zhu J, Lu F, Chen Z. In vivo microvascular network imaging of the human retina combined with an automatic three-dimensional segmentation method. Journal of biomedical optics. 2015;20(7):076003.
98. Garvin MK, Abràmoff MD, Kardon R, Russell SR, Wu X, Sonka M. Intraretinal layer segmentation of macular optical coherence tomography images using optimal 3-D graph search. IEEE transactions on medical imaging. 2008;27(10):1495-505.
99. Ishikawa H, Stein DM, Wollstein G, Beaton S, Fujimoto JG, Schuman JS. Macular segmentation with optical coherence tomography. Investigative ophthalmology & visual science. 2005;46(6):2012-7.
100. Friedman NJ, Kaiser PK, Pineda II R. The Massachusetts Eye and Ear Infirmary Illustrated Manual of Ophthalmology E-Book: Elsevier Health Sciences; 2014.
101. Fine SL, Berger JW, Maguire MG, Ho AC. Age-related macular degeneration. New England Journal of Medicine. 2000;342(7):483-92.
102. Spaide RF. Fundus autofluorescence and age-related macular degeneration. Ophthalmology. 2003;110(2):392-9.
103. Ford MR, Dupps WJ, Rollins AM, Roy AS, Hu Z. Method for optical coherence elastography of the cornea. Journal of biomedical optics. 2011;16(1):016005.
104. Larin KV, Sampson DD. Optical coherence elastography–OCT at work in tissue biomechanics. Biomedical optics express. 2017;8(2):1172-202.
105. Cohen E, Agrawal A, Connors M, Hansen B, Charkhkar H, Pfefer J. Optical coherence tomography imaging of retinal damage in real time under a stimulus electrode. Journal of neural engineering. 2011;8(5):056017.
106. Dasari B, Prasanthi JR, Marwarha G, Singh BB, Ghribi O. Cholesterol-enriched diet causes age-related macular degeneration-like pathology in rabbit retina. BMC ophthalmology. 2011;11(1):22.
107. Pennesi ME, Neuringer M, Courtney RJ. Animal models of age related macular degeneration. Molecular aspects of medicine. 2012;33(4):487-509.
108. Kimura N, Sakuma K, Hirafune S, Asano K, Hirosaki N, Xie R-J. Extrahigh color rendering white light-emitting diode lamps using oxynitride and nitride phosphors excited by blue light-emitting diode. Applied physics letters. 2007;90(5):051109.
109. Bando K, Sakano K, Noguchi Y, Shimizu Y. Development of high-bright and pure-white LED lamps. Journal of Light & Visual Environment. 1998;22(1):1_2-1_5.
110. Taylor HR, Munoz B, West S, Bressler NM, Bressler SB, Rosenthal FS. Visible light and risk of age-related macular degeneration. Transactions of the American Ophthalmological Society. 1990;88:163.
111. Algvere PV, Marshall J, Seregard S. Age-related maculopathy and the impact of blue light hazard. Acta Ophthalmologica. 2006;84(1):4-15.
112. Liu L, Gardecki JA, Nadkarni SK, Toussaint JD, Yagi Y, Bouma BE, Tearney GJ. Imaging the subcellular structure of human coronary atherosclerosis using micro–optical coherence tomography. Nature medicine. 2011;17(8):1010.
113. Bufi N, Saitakis M, Dogniaux S, Buschinger O, Bohineust A, Richert A, Maurin M, Hivroz C, Asnacios A. Human primary immune cells exhibit distinct mechanical properties that are modified by inflammation. Biophysical journal. 2015;108(9):2181-90.
114. Cai X, Xing X, Cai J, Chen Q, Wu S, Huang F. Connection between biomechanics and cytoskeleton structure of lymphocyte and Jurkat cells: An AFM study. Micron. 2010;41(3):257-62.

115. Zhang J, Rao B, Yu L, Chen Z. High-dynamic-range quantitative phase imaging with spectral domain phase microscopy. Optics letters. 2009;34(21):3442-4.
116. Silverman RH, Urs R, Lloyd HO. Effect of ultrasound radiation force on the choroid. Investigative ophthalmology & visual science. 2013;54(1):103-9.
117. Puri R, Worthley MI, Nicholls SJ. Intravascular imaging of vulnerable coronary plaque: current and future concepts. Nature Reviews Cardiology. 2011;8(3):131.
118. VanderLaan PA, Reardon CA, Getz GS. Site specificity of atherosclerosis: site-selective responses to atherosclerotic modulators. Arteriosclerosis, thrombosis, and vascular biology. 2004;24(1):12-22.
119. Richardson PD. Mechanical properties of atherosclerotic tissues. Mechanics of Biological Tissue: Springer; 2006. p. 207-23.
120. Zhao Y, Chen Z, Saxer C, Xiang S, de Boer JF, Nelson JS. Phase-resolved optical coherence tomography and optical Doppler tomography for imaging blood flow in human skin with fast scanning speed and high velocity sensitivity. Optics letters. 2000;25(2):114-6.
121. Joo C, Akkin T, Cense B, Park BH, De Boer JF. Spectral-domain optical coherence phase microscopy for quantitative phase-contrast imaging. Optics letters. 2005;30(16):2131-3.
122. Choma MA, Ellerbee AK, Yang C, Creazzo TL, Izatt JA. Spectral-domain phase microscopy. Optics letters. 2005;30(10):1162-4.
123. Tracqui P, Broisat A, Toczek J, Mesnier N, Ohayon J, Riou L. Mapping elasticity moduli of atherosclerotic plaque in situ via atomic force microscopy. Journal of structural biology. 2011;174(1):115-23.
124. Kadi AP, Loupas T. On the performance of regression and step-initialized IIR clutter filters for color Doppler systems in diagnostic medical ultrasound. IEEE transactions on ultrasonics, ferroelectrics, and frequency control. 1995;42(5):927-37.
125. Li J, Ma T, Jing J, Zhang J, Patel PM, Kirk Shung K, Zhou Q, Chen Z. Miniature optical coherence tomography-ultrasound probe for automatically coregistered three-dimensional intracoronary imaging with real-time display. J Biomed Opt. 2013;18(10):100502. Epub 2013/10/23. doi: 10.1117/1.JBO.18.10.100502. PubMed PMID: 24145701; PMCID: 3801153.
126. Li J, Ma T, Mohar D, Steward E, Yu M, Piao Z, He Y, Shung KK, Zhou Q, Patel PM, Chen Z. Ultrafast optical-ultrasonic system and miniaturized catheter for imaging and characterizing atherosclerotic plaques in vivo. Sci Rep. 2015;5:18406. doi: 10.1038/srep18406. PubMed PMID: 26678300; PMCID: 4683418.
127. Liang S, Saidi A, Jing J, Liu G, Li J, Zhang J, Sun C, Narula J, Chen Z. Intravascular atherosclerotic imaging with combined fluorescence and optical coherence tomography probe based on a double-clad fiber combiner. J Biomed Opt. 2012;17(7):070501. doi: 10.1117/1.JBO.17.7.070501. PubMed PMID: 22894457.